

**A study on reactively evaporated chalcogenide thin films for
optoelectronic and thermoelectric energy conversion**

*Thesis Submitted to
Cochin University of Science and Technology
in partial fulfillment of the requirements
for the award of the degree of
Doctor of Philosophy
in
Physics*

by

Namitha Asokan T.



**Department of Physics
Cochin University of Science and Technology
Cochin- 682 022, Kerala, India
April 2017**

A study on reactively evaporated chalcogenide thin films for optoelectronic and thermoelectric energy conversion

Ph.D. Thesis:

Author

Namitha Asokan T.
(Assistant Professor, Department of Physics
Sree Narayana College, Nattika)
Teacher Fellow, Solid State Physics Laboratory
Department of Physics
Cochin University of Science and Technology.
Cochin-22, Kerala, India
email – namithaasokan@gmail.com

Guide

Dr. B. Pradeep
Professor
Department of Physics
Cochin University of Science and Technology
Cochin-22, Kerala, India

Department of Physics
Cochin University of Science and Technology
Cochin-22, Kerala, India

April 2017



Department of Physics
Cochin University of Science and Technology
Kochi- 682022, Kerala, India

Dr. B. Pradeep
Professor

Certificate

Certified that the work presented in the thesis entitled “A study on reactively evaporated chalcogenide thin films for optoelectronic and thermoelectric energy conversion” is a bonafide record of research done by Mrs. Namitha Asokan T., under my guidance and supervision at Department of Physics, Cochin University of Science and Technology, Kochi, Kerala, India. The work presented in this thesis has not been included in any other dissertation submitted previously for the award of any other degree, diploma, associateship or any other title or recognition from any University/Institution. All the relevant corrections and modifications suggested by the audience during the pre-synopsis seminar and recommended by the doctoral committee of the candidate has been incorporated in the thesis.

Kochi - 682022
Date: 27.04.2017

Prof. B. Pradeep
(Research Supervisor)

Phone: +91 0484 2577404 **Fax:** +91 0484 2862459 **Email:** bp@cusat.ac.in

DECLARATION

I hereby declare that the work presented in the thesis entitled “A study on reactively evaporated chalcogenide thin films for optoelectronic and thermoelectric energy conversion” is based on the original research work done by me under the guidance and supervision of Dr. B. Pradeep, Professor, Department of Physics, Cochin University of Science and Technology, Kochi, Kerala, India. The work presented in this thesis has not been included in any other dissertation submitted previously for the award of any other degree, diploma, associateship or any other title or recognition from any University/Institution.

Kochi - 682022

Namitha Asokan T.

Date: 27.04.2017

Acknowledgements

This dissertation arose in part out of years of research that has been done since I came to Solid State Physics Laboratory. By that time, I have worked with a great number of people whose contribution in various ways to the research and the making of the thesis deserve special mention. It is a pleasure to convey my gratitude to them all in my humble acknowledgment.

In the first place I would like to express my gratitude to Prof. B. Pradeep for his supervision, advice, and guidance from the very early stage of this research as well as throughout the work. Above all and the most needed, he provided me unflinching encouragement and support in various ways. I am indebted to him more than he knows.

I am thankful to Prof. M. Junaid Bushiri, Head of Department of Physics for all the facilities extended to me in the Department. I would like to express my sincere appreciation to former Heads and all the faculties of Department of Physics, CUSAT for their help and facilities for the various characterization studies. I am thankful to all the office and library staff of Department of Physics, CUSAT. I am extremely thankful to Prof. M. K. Jayaraj, Department of Physics, CUSAT for the help and support extended throughout the course, as Doctoral Committee member. I am extremely thankful to the Management, Principal, teachers and administrative staff of

Sree Narayana College, Nattika for their constant support and encouragement throughout the period of my Ph.D. programme.

I am grateful to Dr. V. Ganesan and Dr. G.S. Okram, UGC-DAE for AFM and TEP measurement. I am also grateful to T. Shripathi, UGC-DAE for his valuable help in the XPS measurement. My heartfelt thanks to Raichel Reena Philip, R. Geethu, Dhanya S. and Rajani Jacob, Department of Physics, Union Christian College, Aluva for the help in photoconductivity study. I acknowledge STICK, CUSAT and Department of Physics, Sree Narayana College, Nattika for taking SEM- EDAX and Hall measurements of my samples.

I greatly acknowledge University Grants Commission for providing me the fellowship through RFSMS scheme and facility of Faculty development programme for the remaining years during the course of my work.

I express my heartfelt thanks to my dearest friends K. S. Urmila, Anuroop R., Sreejith P., Abhilash A., Hiba Rehman E. and Reena Rajan for their sincere friendship and support right from the beginning of my work.

I express my gratitude to M.Phil. students and M.Sc. project students. I express my sincere thanks to all my friends in the Physics Department, other Departments in CUSAT for their loving support throughout my life at CUSAT.

I thank all the teachers of my school days, graduation and post-graduation for inspiring and encouraging me in all endeavours.

It is an honour to thank my parents for their unflagging love and support throughout my life. My parents especially my mother never complained in spite of all the hardships in their life. I also remember my brother Mr. Anuraj and his wife Reshmi with affection.

My deepest gratitude goes to my understanding, loving, patient husband Prijith P. Asok. This dissertation would have been simply impossible without him. It is just because of the support extended by him and his parents, that I am submitting this thesis. Special thanks to my beloved children, Parvana and Sreeraman whose love and patience helped me quite a lot to complete this work. Thank God Almighty for the blessings and wisdom to finish this thesis and indeed, throughout my whole life.

Namitha Asokan T.

Preface

Chalcogenide materials have had a prominent position in the field of photovoltaic (PV) and thermoelectricity because of their versatility in combination with other elements and the small variation in electronegativity between sulfur, selenium, and tellurium, it is possible to obtain semiconductors with energy gaps appropriate for TE and PV applications over a wide range of temperature. Thin films based on sulfides, selenides and tellurides, have recently attracted much interest as materials for optoelectronics and thermoelectric (TE) technology. Now a day there has been exponentially increasing interest in developing chalcogenide thin film for solar cell and TE application because of the raw material can be obtained easily, cheaper and abundant.

Today we predominantly depend on fossil fuels (i.e. coal, oil and gas) and with the addition of electricity from nuclear power to meet our energy demands. The present global primary energy consumption (GPEC) is ~ 15 TW. World energy demand increased more than tenfold over the 20th century and in the 21st century, further increases in world energy consumption can be expected. PV power generation technology is one of the most renewable energy technologies which employs solar panels composed of a number of solar cells containing a photovoltaic material. Approximately 90 per cent of the world's power is generated by heat engines that use fossil fuel combustion as a heat source and typically operate at 30–40 % efficiency, such that a large amount of heat is lost to the environment. The development of new materials

with high efficiency is one of the key factors for expanding the range of PV and TE applications to the medium/large scale. Present work focuses on preparation and characterization of chalcogenide thin films for TE and PV applications using cost-effective technique in order to fulfill the world's future energy needs. The thesis divided into eight chapters.

Chapter 1: This chapter deals with recent developments of chalcogenide thin films in PV and TE technology. Material properties and evolution of thin semiconducting films in PV technologies are also included. TE phenomena enable the solid-state inter conversion of thermal and electrical energy. This conversion occurs through two primary phenomena: the Seebeck and the Peltier effect. This chapter includes the basic theories of thermoelectrics and the most significant material properties that are important for the preparation of high efficiency photovoltaic solar cells.

Chapter 2: This chapter deals with the basics of semiconductors. The chapter also includes some analytical expressions that are in good agreement with the most interesting experimental data of the semiconductors, and which can be used for numerical calculations in the prepared semiconducting thin films.

Chapter 3: This chapter deals with the theory of evaporation and the surface mechanism during film growth. The discussions of the theory of the reactive evaporation technique, its advantages, disadvantages etc are also included. Furthermore, the chapter contains a brief discussion of the

experimental techniques used for the determination of the transport quantities, structural parameters and optical quantities. The techniques involve x-ray diffraction, atomic force microscopy, energy dispersive X-ray spectroscopy, X-ray photo electron spectroscopy, scanning electron microscopy, Fizeau technique, thickness profiler, absorption and transmission, hall measurement, electrical conductivity and thermoelectric power.

Chapter 4: This chapter deals with preparation and characterization of lead selenide thin films (PbSe). PbSe compounds attract considerable scientific attraction due to the technological importance of these materials, in crystalline and polycrystalline forms as IR detectors, solar cell, solar control coatings, photographic plates, laser selective and photoconductive absorber and analyzers. The various optical and transport properties of the PbSe thin films prepared using the reactive evaporation technique are also included.

Chapter 5: This chapter deals with preparation and characterization lead antimony selenide thin films ($\text{Pb}_{3.58}\text{Sb}_{4.42}\text{Se}_{10}$). nano-structured. P-type $\text{Pb}_{3.58}\text{Sb}_{4.42}\text{Se}_{10}$ are reactively evaporated and their structural, optical and transient photoconductivity properties are evaluated. Interest in extending the temperature range of operation above that of the commercially used TE materials, the Seebeck coefficient of $\text{Pb}_{3.58}\text{Sb}_{4.42}\text{Se}_{10}$ thin films are studied over low temperature.

Chapter 6: Silver selenide is a I-VI narrow band gap semiconductor and is found in nature as a component of minerals, the so called

Naumannite. Studies on thin films of Ag_2Se are attracting wide attention for various non-linear optical devices, rechargeable secondary devices, multipurpose ion-selective electrodes, infra-red sensors, photolithographic layers, electrochemical potential memory devices, semiconducting optical devices for visible region, Schottky barrier, resistive random-access memory device and super ionic conductor. This chapter deals with preparation and characterization silver selenide (Ag_2Se) thin films. Polycrystalline thin films of silver selenide are prepared by reactive evaporation technique to investigate the optoelectronic and thermoelectric properties.

Chapter 7: This chapter deals with AgSbSe_2 thin films prepared using reactive evaporation technique. To evaluate the potentiality of this material for optoelectronic and thermoelectric applications, structural, electrical, optical and low temperature thermoelectric properties to enlighten the electron transport behavior, are also studied and presented.

Chapter 8: This is the concluding chapter of the thesis and in this chapter the salient observations and the inferences out of these investigations and the summary of results are presented. The scope for future work is also proposed here.

Journal Publications

- [1] **Namitha Asokan T.**, K. S. Urmila and B. Pradeep, “Structural, optical, transient photoconductivity studies and low temperature thermoelectric power measurements on reactively evaporated lead selenide thin films,” *J. Mater. Sci.: Mater.in Electron.*, vol. 27, pp. 5646–5653, 2016.
- [2] **Namitha Asokan T.**, K. S. Urmila, B. Pradeep, “Electrical and photoconductivity studies on AgSbSe₂ thin films,” *IOP Conf. Ser. Mater. Sci. Eng.*, vol. 73, pp. 012013 1–3, 2015.
- [3] **Namitha Asokan T.**, K. S. Urmila, Rajani Jacob, Rachel Reena Philip, G. S. Okram, V. Ganesan and B. Pradeep, “ Optical and electrical properties and phonon drag effect in low temperature TEP measurements of AgSbSe₂ thin film,” *J. Semicond.*, vol. 35, pp. 052001 1-6, 2014.
- [4] **Namitha Asokan T.**, K. S. Urmila and B. Pradeep, “Structural and Optical Studies on AgSbSe₂ thin films,” *AIP Conf. Proc.*, vol. 1576, pp. 60–62, 2014.
- [5] **Namitha Asokan T.**, K. S. Urmila and B. Pradeep, “An investigation on structural, optical and transport properties of Ag₂Se thin films deposited by reactive evaporation technique,” (communicated)
- [6] **Namitha Asokan T.**, K. S. Urmila and B. Pradeep, “Reactively evaporated Pb_{3.58}Sb_{4.42}Se₁₀ thin films - A novel chalcogenide for optoelectronic and

thermoelectric applications,”(communicated)

- [7] K. S. Urmila, **Namitha Asokan T.**, B. Pradeep, “Thermoelectric figure of merit in degenerate Cu_7Se_4 and non degenerate InSe thin films,” *Int. J. Recent. Res. Rev*, vol. 9, pp. 13, 2016.
- [8] K. S. Urmila, **Namitha Asokan T.** and B. Pradeep, “Analysis of structural parameters and low temperature electrical conductivity and thermoelectric power in slightly Cu rich p-type CuInSe_2 thin films,” *Int. J. Recent. Res. Rev*, vol. 8, pp. 1, 2015.
- [9] K. S. Urmila, **Namitha Asokan T.** and B. Pradeep, “Characterisation of defect levels and their influence in photoconductivity of p-type CnInSe_2 thin films,” *Int. J. Recent. Res. Rev*, vol. 8, pp. 10, 2015.
- [10] K. S. Urmila, **Namitha Asokan T.**, Rajani Jacob, Rachel Reena Philip, and B. Pradeep, “Optoelectronic properties and Seebeck coefficient in SnSe thin films,” *J. Semicond.*, vol. 37, no. 9, pp. 093002 1–6, 2016.
- [11] K. S. Urmila, **Namitha Asokan T.**, Rachel Reena Philip, V. Ganesan, G. S. Okram and B. Pradeep “Structural, optical, electrical and low temperature thermoelectric properties of degenerate polycrystalline Cu_7Se_4 thin films,” *Phys. Status Solidi B*, vol. 251, pp. 689–696, 2014.
- [12] K.S. Urmila, **Namitha Asokan T.**, Rachel Reena Philip and B. Pradeep, “Optical and low-temperature thermoelectric properties of phase-pure p-

- type InSe thin films,” *Appl. Phys. A*, vol. 120, no. 2, pp. 675–681, 2015.
- [13] Rachel Reena Philip, S. Dhanya, **Namitha Ashokan T.** and B. Pradeep, “Effect of Ga incorporation on valence band splitting of OVC CuIn_3Se_5 thin films,” *Journal of Phy. and Chem. of Solids*, vol. 72, pp. 294–298, 2011.
- [14] K.S. Urmila, **Namitha Asokan T.** and B. Pradeep, “Structural and optical characterization of reactive evaporated tin diselenide thin films,” *IOP Conf. Ser. Mater. Sci. Eng.*, vol. 73, pp. 012058 1–5, 2015.
- [15] K. S. Urmila, **Namitha Asokan T.**, Rajani Jacob, Rachel Reena Philip and B. Pradeep, “Photoconductivity in Reactively Evaporated Copper Indium Selenide Thin Films,” *AIP Conf. Proc.*, vol. 1576, no. 69, pp. 69–72, 2014.
- [16] K. S. Urmila, **Namitha Asokan T.** and B. Pradeep “Photoluminescence Study of Copper Selenide Thin Films,” *AIP Conf. Proc.*, vol. 1391, pp. 770–772, 2011.
- [17] R. Geethu , Dhanya S., Sreenivasan P. V., **Namitha Ashokan T.**, B. Pradeep and Rachel Reena Philip “Optoelectronic Properties of Nanostructured Cadmium Sulphide Thin Films,” *AIP Conf. Proc.*, vol. 1391, pp. 585, 2011.

Conference Publications

- [1] **Namitha Asokan T.**, K. S. Urmila and B. Pradeep, “Optical investigation on polycrystalline $\text{Pb}_{3.58}\text{Sb}_{4.42}\text{Se}_{10}$ thin films,” in *fourth international conference on frontiers in nanoscience and technology (Cochin NANO-2016)*, February 20-23, 2016 CUSAT, Kochi.
- [2] **Namitha Asokan T.**, K. S. Urmila and B. Pradeep , “Structural and Optical Studies on AgSbSe_2 Thin Films,” in *International Conference on Optoelectronic Materials and Thin Films (OMTAT)*, January 3-5, 2013 CUSAT, Kochi.
- [3] **Namitha Asokan T.**, K. S. Urmila and B. Pradeep , “Electrical and Photoconductivity studies on AgSbSe_2 thin films,” in *International Conference on Materials Science and Technology (ICMST)*, June 10-14, 2012 Pala.
- [4] **Namitha Asokan T.**, K. S. Urmila and B. Pradeep, “Optical and electrical characterisation of silver selenide thin films,” in *National conference on Advances in Materials Science: Macro to Nano Scales (NCAMS)*, March 16- 17, 2012 Aluva.
- [5] **Namitha Asokan T.**, K. S. Urmila, B. Pradeep, S. Dhanya and Rachel Reena Philip, “Optical characterisation of lead selenide thin films

prepared by reactive evaporation,” in *International Conference on Contemporary trends in Optics and Opto Electronics, January 17-19, 2011 Thiruvananthapuram*.

- [6] K. S. Urmila, **Namitha Asokan T.** and B. Pradeep “Sn₂Sb₄Se₈ thin films-a novel chalcogenide for energy applications,” in *International conference on materials for the millennium (MATCON 2016), January 14-16, 2016 Kochi*
- [7] K. S. Urmila, **Namitha Asokan T.** and B. Pradeep, “InSbSe₃ thin films – a prospective absorber layer material for thin film solar cells”, in *international conference on energy harvesting, storage and conversion (IC-EEE 2015)* , February 5-7, 2015 Kochi.
- [8] K. S. Urmila , **Namitha Asokan T.** and B. Pradeep, “Opto electronic properties of phase pure InSe Thin Films,” in *ICAFM 2014*, pp. 328–329.
- [9] K.S. Urmila, **Namitha Asokan T.** and B. Pradeep, “SnSe thin films-A prospective material for thermoelectric applications,” *NCAM 2014*, p. 35.
- [10] Simi George, **Namitha Asokan T.**, K. S. Urmila, Anuroop R. and B. Pradeep, “Structural and electrical studies of reactively evaporated lead selenide thin film,” *NCAM 2014*, p. 34.

- [11] K. S. Urmila, **Namitha Asokan T.**, B. Pradeep, Rajani Jacob and Rachel Reena Philip, "Photoconductivity in Reactively Evaporated Copper Indium Selenide Thin Films," in *International Conference on Optoelectronic Materials and Thin Films (OMTAT), January 3-5, 2013 CUSAT, Kochi.*
- [12] K. S. Urmila, **Namitha Asokan T.** and B. Pradeep, "Structural and Optical Characterization of reactive evaporated tin diselenide thin films," in *International Conference on Materials Science and Technology (ICMST), June 10-14, 2012 Pala.*
- [13] K. S. Urmila, **Namitha Asokan T.** and B. Pradeep, "Structural and Electrical Characterization of Copper Selenide thin films," in *National conference on Advances in Materials Science: Macro to Nano Scales (NCAMS), March 16-17,, 2012 Aluva.*
- [14] K. S. Urmila, **Namitha Asokan T.** and B. Pradeep, "Preparation and Optical Characterization of Indium Selenide thin films," in *National Seminar on Trends in Physical Sciences (TriPS), July 21- 22, 2011 Kalady.*
- [15] R. Geethu , S. Dhanya, P. V. Sreenivasan, **Namitha Ashokan T.**, B. Pradeep, Rachel Reena Philip, "Optoelectronic Properties of Nanostructured Cadmium Sulphide Thin Films," in *International Conference on light OPTICS' 11, May 23-25 2011 NIT Calicut.*

- [16] Urmila K. S. , **Namitha Asokan T.** and B. Pradeep. "Photoluminescence study of copper selenide thin films," in *International Conference on light OPTICS' 11, May 23-25 2011, NIT Calicut*
- [17] K.S. Urmila, **Namitha Asokan T.** and B. Pradeep, "Preparation and optical characterisation of copper selenide thin films," in *International Conference on Contemporary trends in optics and Opto Electronics, January 17-19, 2011 Thiruvananthapuram.*
- [18] Hiba Rahman, Reshmi Radhakrishnan, Nafsia Karim, Faseela K, Dhanya S., **Namitha Asokan T.**, B. Pradeep and Rachel Reena Philip. "Optical properties of flower like nanostructured films of PbS," in *International Conference on Contemporary trends in optics and Opto Electronics, January 17-19, 2011 Thiruvananthapuram.*

Contents

Chapter 1

***An introduction to semiconductors and chalcogenide thin films*01-48**

1.1	Introduction to semiconductors and chalcogenide thin films.....	01
1.2	Material properties and evolution of thin semiconducting films in PV technologies.....	06
1.3	Enhancement of direct solar energy conversion through thermoelectrics	12
1.4	Thermoelectrics–Basic principle, applications and advances in thermoelectric materials.....	14
1.4.1	Basic theory of thermoelectrics.....	17
1.4.2	Development of thermoelectric materials.....	24
1.5	Role of chalcogenide thin film in PV and TE applications.....	34
1.6	Aim and objective of the present work.....	35
	References.....	38

Chapter 2

***Transport and optoelectronic properties in semiconductors*.....49-76**

2.1	Introduction.....	49
2.2	Band theory of solids.....	50
2.3	Classification of semiconductors.....	53
2.4	Transport properties in semiconductors.....	56
2.4.1	Electrical conductivity.....	56
2.4.2	Hall effect.....	58
2.5	Optical absorption in semiconductors.....	59
2.6	Optical transmission in semiconductors.....	66
2.6.1	Determination of the optical constants and thickness of the film using Swanepoel method.....	66
2.7	Optical conductivity of semiconductors.....	71
2.8	Photoconductivity of semiconductors.....	72
	References.....	74

Chapter 3

Experimental techniques and characterization tools	77-121
3.1 Introduction.....	77
3.1.1 Physical evaporation technique	79
3.1.2 Evaporation Theory – General Considerations.....	80
3.1.3 Surface mechanism during the film growth.....	82
3.2 Gunter’s three temperature method.....	85
3.2.1 Condensation Phenomena Occurring With Binary Vapours.....	89
3.2.2 Advantages and limitations of reactive evaporation technique.....	93
3.3 Experimental details of the reactive evaporation technique used in present investigation.....	94
3.3.1 Vacuum coating unit.....	94
3.3.2 Deposition of thin films.....	96
3.4 Characterisation tools.....	98
3.4.1 XRay Diffraction.....	98
3.4.2 Measurement of film thickness.....	101
3.4.3 Measurement of conductivity type: hot probe method.....	104
3.4.4 Electrical conductivity measurement.....	106
3.4.5 Photoconductivity measurement.....	107
3.4.6 Scanning Electron Microscopy (SEM).....	108
3.4.7 EDAX.....	110
3.4.8 Atomic Force Microscopy (AFM).....	111
3.4.9 Thermoelectric power (TEP).....	113
3.4.10 X ray Photoemission Spectroscopy (XPS).....	115
3.4.11 Hall effect.....	117
3.5 Aim of the present work.....	118
References.....	118

Chapter 4	
<i>Reactively evaporated p-type lead selenide thin films and its characterization</i>	122-151
4.1 Introduction.....	122
4.2 Experimental details.....	126
4.3 Results and discussions.....	128
4.3.1 Structural analysis.....	128
4.3.2 Morphological and compositional analysis.....	129
4.3.3 Electrical analysis.....	132
4.3.4 Optical analysis.....	134
4.3.5 Low temperature TEP properties and Hall measurement.....	141
4.4 Conclusion.....	145
References.....	146
Chapter 5	
<i>Reactively evaporated p-type lead antimony selenide thin films and its characterization</i>	152-177
5.1 Introduction.....	152
5.2 Experimental details.....	154
5.3 Results and discussions.....	156
5.3.1 Structural analysis.....	156
5.3.2 Morphological and compositional analysis.....	157
5.3.3 Optical analysis.....	161
5.3.4 Low temperature TEP properties and Hall measurement.....	169
5.4 Conclusion.....	172
References.....	172

Chapter 6	
<i>Reactively evaporated n-type silver selenide thin films and its characterization</i>178-199	
6.1	Introduction..... 178
6.2	Experimental details..... 180
6.3	Results and discussions..... 181
6.3.1	Structural analysis..... 181
6.3.2	Morphological and compositional analysis..... 183
6.3.3	Electrical analysis..... 185
6.3.4	Optical analysis..... 187
6.3.5	Low temperature TEP properties and Hall measurement..... 191
6.4	Conclusion..... 194
	References..... 194
Chapter 7	
<i>Reactively evaporated n-type silver antimony selenide thin films and its characterization</i>200-228	
7.1	Introduction..... 200
7.2	Experimental details..... 202
7.3	Results and discussions..... 204
7.3.1	Structural analysis..... 204
7.3.2	Morphological and compositional analysis..... 205
7.3.3	Electrical analysis..... 209
7.3.4	Optical analysis..... 210
7.3.5	Low temperature TEP properties and Hall measurement..... 220
7.4	Conclusion..... 225
	References..... 225

Chapter 8

Summary and future outlook.....229-232

8.1 Summary and general conclusions..... 229

8.2 Future outlook..... 231

Chapter 1

An introduction to semiconductors and chalcogenide thin films

- 1.1 Introduction to semiconductors and chalcogenide thin films*
- 1.2 Material properties and evolution of thin semiconducting films in PV technologies*
- 1.3 Enhancement of direct solar energy conversion through thermoelectrics*
- 1.4 Thermoelectrics-Basic principle, applications and advances in thermoelectric materials*
- 1.5 Role of chalcogenide thin film in PV and TE applications*
- 1.6 Aim and objective of the present work*

1.1 Introduction to semiconductors and chalcogenide thin films

Recently semiconductors have become most commonly used material for electronic and optoelectronic devices including computers, detectors, solar cells, Flat Panel Display (FPD), Optical Coatings, Data Storage, Super capacitor, solid state lasers etc. [1]. The rapid developments in semiconductor technology affect many aspects of the technological society which make our daily life more reliable and comfort than earlier. The physics of semiconductor devices depends on the optoelectronic properties of the semiconductor materials themselves. Semiconductors are materials having electrical conductivity in the range 10^4 to $10^{-10} (\Omega\text{cm})^{-1}$ intermediate between good conductors (10^6 to $10^4 (\Omega\text{cm})^{-1}$) and insulators ($< 10^{-10} (\Omega\text{cm})^{-1}$) [2].

Semiconductors can also be defined as a material with a finite energy gap below 3 eV. The additional properties include negative temperature coefficient of resistance and sensitivity to light. Semiconductors have zero conductivity at 0 K and quite lower conductivity at finite temperature, but it is possible to alter their conductivity by order of magnitude by simple excitations like temperature, light or by adding impurities. This is the key reason why semiconductors can be used for active devices [3]. They are the class of elements which have four valence electrons. Typical elemental semiconductors are silicon (Si) and germanium (Ge). In addition to elemental semiconductors, compound semiconductors also exist. Typical compound semiconductors are gallium arsenide (GaAs), Indium antimony (InSb) indium phosphide (InP) and gallium nitride (GaN), zinc sulphide (ZnS). Most of the elemental and binary compound semiconductors with average four valence electrons per atom, crystallise in diamond or NaCl structure, preferentially form tetrahedral bonds. To date, most of the solid state devices have been made of semiconducting materials, and, as a result, a great deal of research has gone into the physical properties of these materials, in order to improve production and design processes.

Thin films are layer of materials ranging from fractions of nanometer to several micrometers in thickness. The thin film properties may be different from that of the bulk. The recent trends in the field of modern technology are based on the miniaturization; therefore, thin films become very important when hybrid hetero-structures have to integrate together. The thin film studies have advanced many new areas of research in solid state physics and chemistry

which are based on phenomena uniquely characteristic of the thickness, structure, optical and electrical properties of films [4]. Factually, over the past 50 years, the thin films have been used for manufacturing optical coatings, electronic devices, decorative parts, and instrument hard coatings [5].

The term “chalcogen” is used to describe the members of group 16 of the periodic table (figure 1.1). It consists of the elements oxygen (O), sulphur (S), selenium (Se), tellurium (Te) and polonium (Po). The generic term chalcogenide is commonly used in naming the compounds of chalcogen [6]. The name chalcogen was proposed by Wilhelm Blitz and his co-worker Werner Fischer of the institute of Inorganic chemistry at the university of Hannover, Germany in 1932. The term chalcogen was derived from the old Greek word *chalcos*, meaning “ore formers”. They have 6 electrons in their outermost shell. The formal oxidation number of the most common chalcogen compounds is -2. In pyrite it is found to be -1. The highest formal oxidation number +6 is found in sulfates, selenates and tellurates. These names were analogues to the well-known terms “halogens” (salt formers) and “halogenides” from the group 17 elements in the periodic table, the majority of halogenides being salts and chalcogenides being ores [7], [8]. As an element, oxygen is a gas and it is the most abundant element in the earth’s crust. The other elements are solids. Both O and S are non-metals, polonium is a radioactive metal and Se and Te are metalloid semiconductors. Generally for semiconducting chalcogenides the band gap is considerably smaller (1–3 eV). The binary, ternary and quaternary semiconductors belonging to the VA- VIA group chalcogenides, mixed chalcogenides, VIB–VA group chalcogenides, are

well known for their promising material applicable to solar cell, corrosion resistant coating, microelectronics, optics, magnetic, laser devices and gas sensor [9]. Therefore thin films based on sulfides, selenides and tellurides, have recently attracted much interest as materials for optoelectronics technology. Now a day there has been exponentially increasing interest in developing chalcogenide thin film for solar cell application because of the raw material can be obtained easily, cheaper and abundant.

IUPAC Periodic Table of the Elements

Key: Atomic number, Symbol, Name, Standard atomic weight

Notes:

- IUPAC 2011 Standard atomic weights abridged to four significant digits (Table 4 published in Pure Appl. Chem. 83, 1047-1078 (2011); <http://ci.ilo.org/ilo/1361/iupac-2011-3-20-2011>). The uncertainty in the last digit of the standard atomic weight value is listed in parentheses following the value. In the absence of parentheses, the uncertainty is one in that last digit. An interval in square brackets provides the lower and upper bounds of the standard atomic weight for that element. No values are listed for elements which lack isotopes with a characteristic isotopic abundance in natural terrestrial samples. See IUPAC for more details.
- "Aluminium" and "caesium" are commonly used alternative spellings for "aluminum" and "caesium."
- Claims for the discovery of all the remaining elements in the last row of the Table, namely elements with atomic numbers 113, 115, 117 and 118, and for which no assignments have yet been made, are being considered by a IUPAC and IUPAP joint working party.

For updates to this table, see http://iupac.org/iupac/periodic_table/. This version is dated 1 May 2013.
Copyright © 2013 IUPAC, the International Union of Pure and Applied Chemistry.

Fig.1.1. IUPAC Periodic Table of the Elements [10]

Ho Soonmin and T. Joseph Sahaya Anand [11] reviewed chalcogenide films prepared using various physical and chemical deposition methods. The authors concluded that thin films are considered as potential candidates for absorber materials of solar cells. It is because of band gap energy range of 1.0

to 2.0 eV, high absorption coefficient and successfully produce uniform layer so that they can efficiently absorb light on almost any surface. Currently, many scientists reported various binary and ternary chalcogenide thin films in solar cell application in their research findings including cadmium sulfide, tin sulfide, bismuth sulfide, iron sulfide, lead selenide, copper tin sulfide, copper indium selenide, silver indium sulfide and zinc indium selenide [12].

Among them selenium based chalcogenide thin films have received a lot of attention because of their potential in solar cell applications. Selenium was discovered by Jons Jacob Berzellius in 1817. The most stable and dense form of Se is grey in colour which acts as a semiconductor showing appreciable photoconductivity. Therefore Se happens to be the most important semiconductor of 19th century for its interesting optoelectronic properties which laid the foundation of photovoltaic engineering. Before the advent of silicon and germanium rectifiers, selenium happened to be one of the most important materials for the semiconductor industry. Unlike other materials of the 19th century, selenium did not lose its importance as semiconductor, Se compounds are still used as principle material in various electronic and optoelectronic devices because of [13]:

- (i) Se is highly photosensitive material
- (ii) it has a wide optical response from X-rays to NIR
- (iii) it can be prepared in amorphous, polycrystalline or crystalline forms.

Most of the semiconductor thin film technologies are based on chalcogenide thin films. In this thesis it is intended to introduce some chalcogenide thin films for possible photovoltaic and thermoelectric applications.

1.2 Material properties and evolution of thin semiconducting films in PV technologies

Photovoltaic (PV) comes from the Greek word ‘photo’, meaning light, and ‘voltaic’, meaning electricity [14]. Photovoltaic technology is a method of generating electrical power by converting solar radiation into direct current electricity using semiconductors that exhibit the photovoltaic effect [15]. PV power generation technology is one of the most renewable energy technologies which employs solar panels composed of a number of solar cells containing a photovoltaic material. The PV effect was discovered in 1839 by Edmond Becquere and the PV effect was first studied in selenium in the 1870s. The selenium PV cell exhibited an efficiency of 1-2%. The PV technology becomes one of the finest ways to harness the solar power after the introduction of silicon as the prime semiconductor material in the late 1950’s. The advantages and limitations of this technology includes:

Advantages

- no noise, no moving parts needed
- no pollutions
- environmentally friendly
- no use of fuels and water
- minimal maintenance requirements

- long lifetime, up to 30 years
- Electricity is generated whenever there is light, solar or artificial
- Operates even in cloudy weather conditions
- modular “custom -made” energy can be sized for any application from watch to a multi-megawatt power plant
- compact and less weight can operate at moderate temperature

Limitations

- PV cannot operate without light
- high initial costs that at the moment overshadow the low maintenance costs and lack of fuel costs
- for large scale applications large area is needed
- PV generates direct current special DC appliances or an inverter are needed in off-grid applications energy storage is needed.

The most significant material properties that are important for the preparation of high efficiency photovoltaic solar cells are:

1. Band gap of the absorbing material: The band gap of the absorbing material must be small enough to allow absorption of an appreciable portion of the solar spectrum.
2. Minority carrier diffusion length and minority carrier lifetime: The diffusion length of minority carriers must be larger than the thickness of the material needed to absorb the light. Indirect band gap materials typically have longer minority carrier diffusion lengths, but also require thicker layers to absorb the light. Direct band gap materials are usually

preferred, because thin layers may be adequate to absorb the light. If the material is a uniform single crystal that is free of impurities and defects, there is usually minimal scattering in the cell and the effective carrier mobility will be high, so the achievement of high efficiency relies primarily on achieving long minority carrier life times.

There are three types of electron–hole recombination that can reduce the minority carrier lifetime: Auger, radiative, and non-radiative. Auger recombination involves two photocarriers (two electrons or two holes), with the transfer of the recombination energy to another electron in the conduction band or another hole in the valence band. Thus, Auger recombination is important when the photocarrier concentrations become large, as for indirect – band gap materials under intense illumination. The non-radiative recombination is caused by impurities, native point defects, dislocations, grain boundaries, or the surface of the crystal. It is most important to eliminate deep traps in solar cell materials to avoid non-radiative recombination since most of the defects are caused by these traps [16]. The semiconductor industry has virtually eliminated crystallographic defects with the growth of high - purity, dislocation - free single crystals of Group IV or III–V materials. In contrast, III–V materials are known to maintain nearly stoichiometric compositions [17].

3. Highly stable: Instability problems may play a dominant role in determining cell efficiency and utility since solar cells are exposed for long periods of time

There are a large number of solar cell materials ranging from silicon to thin films suitable for PV cells. A material (or device) is said to be “photovoltaic” when exposure of the material to light that can be absorbed by the material is able to transform the energy of the photons into electrical energy in the form of a current and voltage. Figure 1.2 shows the materials presently used for photovoltaic’s technologies (first to third generation) [18], [19].

The first generation solar cell material is Si wafers, mainly single crystals and commercial modules showed 12-16% solar conversation efficiency. These cells have already proven their excellent stability and reliability, operating under outdoor conditions without any deterioration in their performance over several decades [20]. The main disadvantage associated with this technology is, however, the resulting high module price from the high cost of manufacturing and installation (presently about \$4.50 per 1-W peak power rating). Thus the second generation materials are semiconductor thin films which include thin films of amorphous Si, copper indium gallium selenide (CIGS), copper indium diselenide (CIS), cadmium telluride (CdTe), gallium arsenide (GaAs), etc.[21]. Solar conversion efficiency of about 12% has been achieved by the thin films with a remarkable cost reduction. The third generation materials are nano-structured semiconductors dye-sensitized materials and semiconducting polymers [22][23].

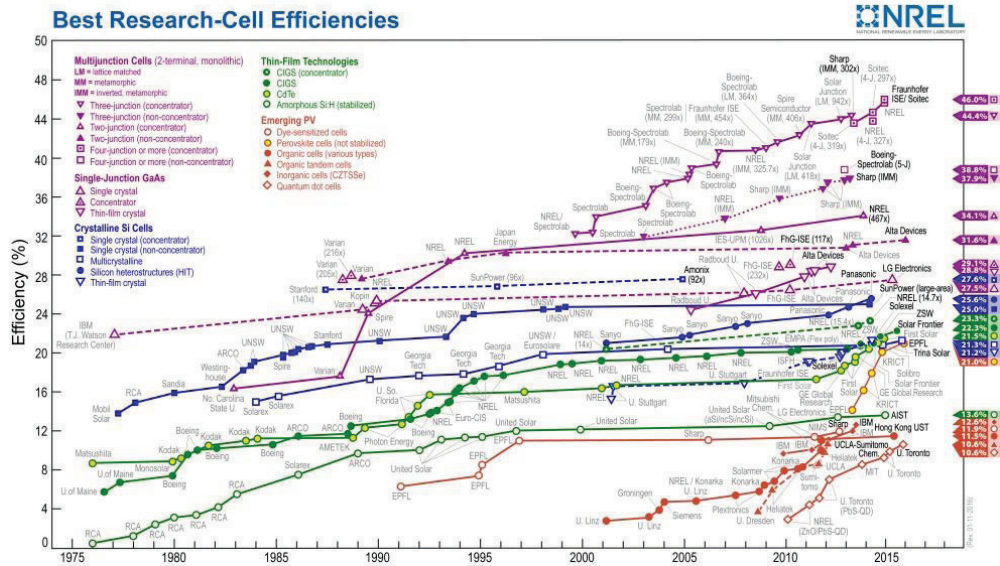


Fig. 1.2 The prominent materials used in solar cells from 1976 to the present [24].

Even though silicon wafer has been the prominent material used for fabrication of solar cells but due to high cost and low efficiency it has gradually lost the interest of researchers, recent interest has shifted to semiconductor thin films. A comparison of crystalline silicon and thin semiconducting material in PV application is shown in figure 1.3.

The comparison shows that thin films in contrast are cheaper and rapidly improving its performance in solar technology. Better technology through advanced materials can reduce costs and improve both the performance and reliability of solar electric systems. Moreover, for thin-film processes the following features have been shown to be of interest for PV technologies [26]:

CELL TYPE	CRYSTALLINE SILICON		THIN FILM		
	Monocrystalline	Polycrystalline	Cadmium Telluride	CIGS	Amorphous Silicon
EFFICIENCY (avg.)	14 – 17.5%	13 – 15%	9-11%	10-12%	5 – 7%
HIGH TEMP. PERFORMANCE	drops 10-15%	drops 20%	0% drop	0% drop	0% drop
OPTIMAL TEMP.	Performs well in cool weather, but poorly in extreme heat	performs well in cool weather, but poorly in extreme heat	performs well in hot weather, even extreme heat	performs well in hot weather, even extreme heat	performs well in hot weather, even extreme heat
COST	most expensive crystalline silicon	cheapest crystalline silicon	cheaper than crystalline silicon—most cost-effective thin film	cheaper than crystalline silicon	cheaper than crystalline silicon
ADDITIONAL DETAILS	oldest solar cell technology and most widely used	economical choice due to its cost to performance ratio	cadmium is toxic, though very small amounts are used	some CIGS panels have posted impressive 20% efficiency figures	requires a lot of roof space and can take longer to install than other cell technologies

Fig. 1.3 Comparison of crystalline silicon and semiconducting thin film materials in PV application [25].

- Small thickness required due to high absorption, small diffusion length & high recombination velocity
- Materials economy, very low weight per unit power
- Various simple & sophisticated deposition techniques are available for depositing thin-films.
- A variety of structures available : amorphous, polycrystalline, epitaxial
- Topography ranging from very rough to atomically smooth
- Tandem and multi junction cells possible
- In-situ cell integration to form modules
- Compatibility with solar thermal devices
- Tailorability of various optoelectronic properties (e.g.; energy gap, electron affinity, work function, graded gap etc.)
- Formation of hetero-junction and better device engineering are possible.

1.3 Enhancement of direct solar energy conversion through thermoelectrics

The spectral distribution of sunlight covers a broad range of wavelengths (figure 1.4) [27]. The radiation can be described as individual photons of energy $E = \frac{hc}{\lambda}$ with part of energy in the ultraviolet (UV) and part in the infrared (IR) region of the solar spectrum. The range of wavelength from 200-3000 nm corresponds to photon energies of 6.2–0.414 eV. About half of the irradiance occurs in the visible region.

The pure atmosphere is almost totally transparent to visible radiation, and becomes an open ‘window’ for solar energy to reach the earth. Nearly 50% of the extraterrestrial solar radiation is in the near IR region. Most conventional solar cells use visible light to generate electricity and IR radiation generates only waste heat in conventional semiconductor –solar photovoltaic cells.

The material parameters in solar cell, which mainly change with the temperature, are band gap energy, which usually decreases and the minority lifetime, which generally increases, with increasing temperature, and correspondingly, the efficiency will degrade [28]. Yongliang Li *et.al.* [29] also reported that cooling or super cooling PV cells decreases the operating temperature and thereby enhance the efficiency of PV cells. Since photons with energy lower than E_g are not absorbed by PV cells, removing this portion of energy from PV cells is beneficial not only for enhancing the cell performance but also for harvesting additional energy from waste heat.

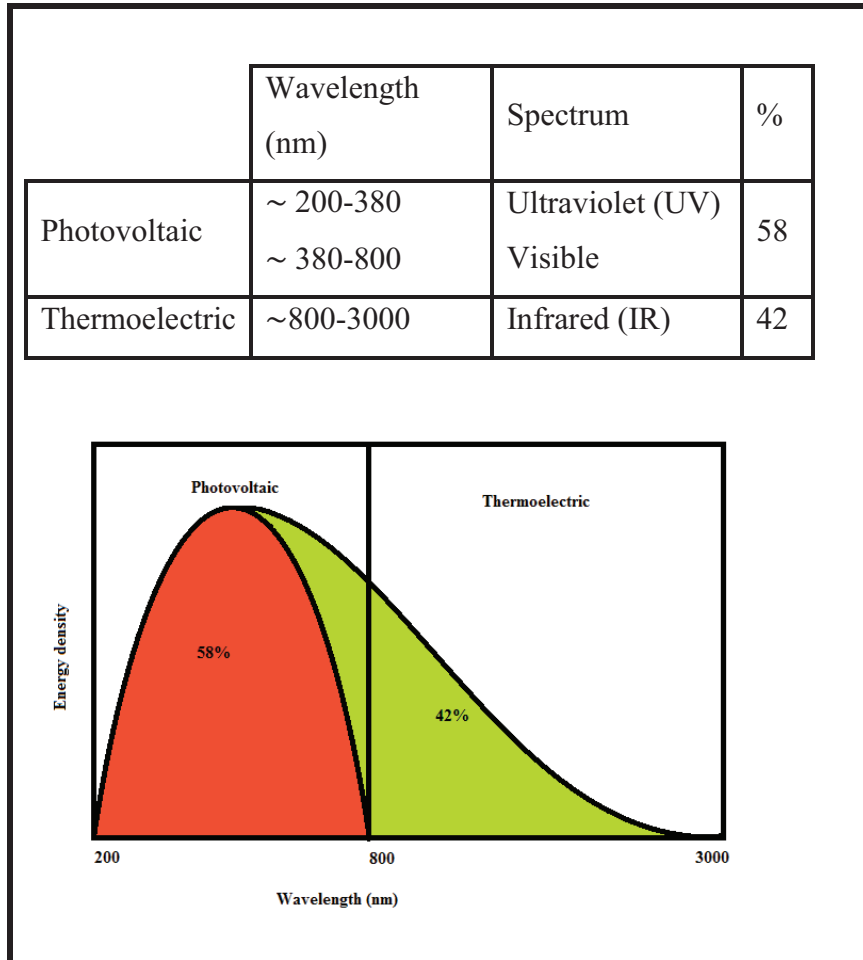


Fig. 1.4 Spectral distribution of sunlight

Enhancing the utilization of solar energy, in order to mitigate the global energy crisis, is in demand because these energy sources are readily accessible and abundant, in contrast to wind, water and pressure [30]. Based on U.S. Energy Information Administration report 2014, the energy currently produced from sunlight remains less than 0.1% of the global energy demand as shown in table 1.1.

Energy Resources	Energy consumption (%)	Renewable energies	Energy consumption (%)
Petroleum	35	Biomass	50
Natural gas	28	Hydroelectric	26
Coal	18	Wind	18
Nuclear electric power	8	Solar	4
Renewable energy	10	Geothermal	2

Table 1.1 The global energy consumption from different energy resources in 2014 [24].

Thus in order to realize widespread development of solar energy conversion applications and contribute to further development in civilization, development in the science and technology of solar energy is very important. Moreover, ~ 60% of energy produced in the United States is wasted in the form of heat. Home heating, automotive exhaust, and industrial processes all generate an enormous amount of unused waste heat. With such a huge potential, there is also significant interest in finding cost-effective technologies for generating electricity from waste heat [31]. One such technology developed so far is “Thermoelectrics”.

1.4 Thermoelectrics – Basic principle, applications and advances in thermoelectric materials

A thermoelectric (TE) structure produces electrical power from heat flow across a temperature gradient. Thermoelectric materials and devices are a solid-state technology that has been in use for decades, but research has been rapidly expanding over the last ten years. The primary reason is that these materials are of great technological importance and could provide significant

contributions as alternative energy materials. Moreover, this thermal structure has no moving parts and is completely quiet and clean, and can be used for years as a complement to photovoltaic systems [28]. Thus, with regard to solar energy conversion, photovoltaic (PV) systems will likely to use the UV and visible light of the solar spectrum while thermoelectric devices use the IR radiation.

TE phenomena enable the solid-state inter conversion of thermal and electrical energy. This conversion occurs through two primary phenomena: the Seebeck and the Peltier effect [32]. In 1821, Seebeck observed that, when the junctions of two dissimilar materials are held at different temperatures (ΔT), a voltage difference (ΔV) is generated that is proportional to ΔT . The ratio $\frac{\Delta V}{\Delta T}$ is related to the intrinsic property of the materials called the Seebeck coefficient or the thermoelectric power S [33]:

$$S = -\frac{\Delta V}{\Delta T} \quad (1.1)$$

A related effect called Peltier effect was discovered in 1834. He observed that when an electric current is passed through a thermoelectric couple, heat is either rejected or absorbed at the junction, depending on the direction of current. The effect is largely due to the differences in Fermi energies of the two materials.

The Peltier coefficient Π , is defined as heat rejected or absorbed per unit volume per unit time per unit current flow from material one to two.

$$\Pi = ST \quad (1.2)$$

where T is the temperature in Kelvin. Therefore the rate at which Peltier heat rejected or absorbed at the junction Q_p is given by [34]

$$Q_p = \Pi I \quad (1.3)$$

where I is the current flowing through the junction.

Thermoelectric module is a solid-state device that directly converts thermal energy into electrical energy [35]. The TE effect can be used for both power generation and electronic refrigeration. Seebeck effect is the basis for TE power generation devices and Peltier effect is the basis of TE refrigeration devices.

The potential of a material for thermoelectric applications both power generation and cooling is determined by a quantity called figure of merit ZT which is introduced by Altenkirch in 1912 as [36]:

$$ZT = \frac{S^2 \sigma T}{\mathcal{K}} \quad (1.4)$$

Where S is the Seebeck coefficient, σ is the electrical conductivity and \mathcal{K} is the total thermal conductivity ($\mathcal{K} = \mathcal{K}_{el} + \mathcal{K}_{ph}$, heat is carried both by electrons and phonons). High electrical conductivity (to minimise Joule heating), a large Seebeck coefficient (to maintain large potential difference) and low thermal conductivity (to maintain a large temperature difference) are necessary in order to realize high-performance TE materials [37]–[39]. The quantity $S^2 \sigma$ is called the power factor. Therefore there are two approaches to increase the value of ZT : either by increasing the power factor and/or by minimizing the thermal conductivity [40]. A good thermoelectric material has a Seebeck coefficient between $100 \mu V K^{-1}$ and $300 \mu V K^{-1}$.

The conversion efficiency of a thermoelectric device is determined as [36], [41]

$$\eta_{TE} = \eta_C \left[\frac{\sqrt{1+ZT}-1}{\sqrt{1+ZT}+\frac{T_C}{T_H}} \right] \quad (1.5)$$

where T_H and T_C are the hot and cold side temperature respectively and $\eta_C = \frac{T_H - T_C}{T_H}$ is the Carnot's efficiency. This equation indicates that increasing η_{TE} requires both high ZT values and a significant difference in temperature (a large ΔT) across the thermoelectric materials. With regard to solar energy conversion, the infrared region of the solar spectrum can supply the needed hot temperature since T_H is generating only waste heat in a conventional solar cell. Thus thermoelectric is potential source of electricity from heat sources through the use of thermoelectric materials and the heat can come from the combustion of fossil fuels, from sunlight, or as a byproduct of various processes.

1.4.1 Basic theory of thermoelectrics

(1) Seebeck coefficient

The TEP or Seebeck coefficient (S) can be thought of as the heat per carrier

$$S = \frac{c}{q} \quad (1.6)$$

where c the specific heat capacity and q is the charge of the carrier.

For degenerate semiconductors,

$$S = \frac{c_{el}}{Ne} = \frac{\pi^2 k_B^2 T}{3eE_F} \quad (1.7)$$

where c_{el} is the electronic specific heat capacity and N is the number of carriers. Since the value of $\frac{k_B}{e} = 87 \mu V K^{-1}$ and S is of the order of 1-

$10 \mu V K^{-1}$ since $E_F \gg k_B T$. The value of S for metals increases with increasing temperature. For non-degenerate semiconductors [42],

$$S = \pm \frac{k_B}{e} \left[A + \frac{E_F}{k_B T} \right] \quad (1.8)$$

where A is constant and E_F is the energy required to excite a carrier to conduction edge for n-type semiconductors or to valence edge for p-type semiconductors. Thus S is larger than the characteristic value of $87 \mu V K^{-1}$ and decreases with increasing temperature. The TEP for semiconductors exhibiting both electron and hole conduction is given by a weighted average of their electrical conductivity values.

$$S = \frac{s_n \sigma_n + s_h \sigma_h}{\sigma_n + \sigma_h} \quad (1.9)$$

(2) Electrical conductivity (σ)

The electrical conductivity for degenerate semiconductors is given by

$$\sigma = n e \mu \quad (1.10)$$

where n is the electron concentration and μ is the mobility given by

$$\mu = \frac{e \tau}{m_e} \quad (1.11)$$

where m_e is the effective mass and τ is the relaxation time. In metals, $n \approx 10^{22}$ carrier/cm³ and σ is large of the order of $10^6 \Omega^{-1} \text{cm}^{-1}$.

For non-degenerate semiconductors, the conductivity can occur through the contributions of both holes and electrons

$$\sigma = n e \mu_e + p e \mu_h \quad (1.12)$$

Again for semiconductors, the carries must be thermally excited across a gap for conduction to occur as

$$\sigma = \sigma_0 \exp\left(-\frac{E_a}{k_B T}\right) \quad (1.13)$$

Therefore there are two ways to achieve high conductivity in non-degenerate semiconductors either by having a very small gap to excite the carriers or by having very high mobility. Typical values of electrical conductivity for a good TE material are of the order of 10^{-4} to $10^4 \Omega^{-1}\text{cm}^{-1}$. In order to ensure large Seebeck coefficient, a single type of carriers (n-type or p-type) should be remained in the material.

(3) Thermal conductivity

The thermal conductivity \mathcal{K} is given by

$$\mathcal{K} = \mathcal{K}_{el} + \mathcal{K}_{ph} \quad (1.14)$$

It consists of two parts: \mathcal{K}_{ph} , which results from heat transporting phonons travelling through the crystal lattice, and \mathcal{K}_{el} , which arises from heat carrying charge carries (electrons or holes) moving through the crystal lattice.

The electronic contribution to thermal conductivity is given by [43]

$$\mathcal{K}_{el} = \frac{\pi^2}{3} \frac{k_B^2 n \tau T}{m} \quad (1.15)$$

And the electronic contribution to thermal conductivity and electrical conductivity are interrelated through Wiedemann- Franz relationship as:

$$\mathcal{K}_{el} = L \sigma T \quad (1.16)$$

where Lorentz number L is defined as:

$$L = \frac{\pi^2}{3} \left(\frac{k_B}{e}\right)^2 \quad (1.17)$$

The ratio \mathcal{K}_{el} is directly proportional to σ and temperature with the value of constant of proportionality is independent of the material. Therefore to reduce

the electronic contribution of the thermal conductivity for thermoelectric materials is not always best choice, since it will inversely affect the electrical conductivity and has little or no improvement of ZT.

The lattice thermal conductivity is given by [43]:

$$\mathcal{K}_{ph} = \frac{1}{3} C v_s l_{ph} \quad (1.18)$$

where v_s is the phonon velocity, C is the phonon heat capacity obeying Debye's model at low temperature and l_{ph} is the phonon mean free path. Thus at low temperature, it increases with temperature and at high temperatures ($T > 300$ K), v_s and C are essentially temperature independent. For a material to be a good candidate for TE performance, the lattice thermal conductivity needs to be as low as possible since K_{ph} is the only parameter not determined by the electronic structure.

How solar energy can be converted into electricity through photovoltaic and thermoelectric can be envisioned as follows (figure 1.5) [27]. Using a solar spectrum splitter, the sunlight with short wavelength portion (visible) is directed to the PV cells where it could be converted into electric energy, and the long wavelength portion (IR) is sent to TE devices to generate useful electricity. The cooling chamber with a low freezing point liquid as circulating fluid is used for reducing the operating temperature of both the PV cells and cold side of the TE generator.

In addition, the thermal energy stored in thermal bath can be used to supply heat for TE devices at off peak time. Therefore, more efficient solar energy utilization can be achieved through this system. Thermoelectric is

potential source of power from heat sources through the use of thermoelectric materials. Therefore, thermoelectric materials can play a role in both primary power generation and waste-heat harvesting.

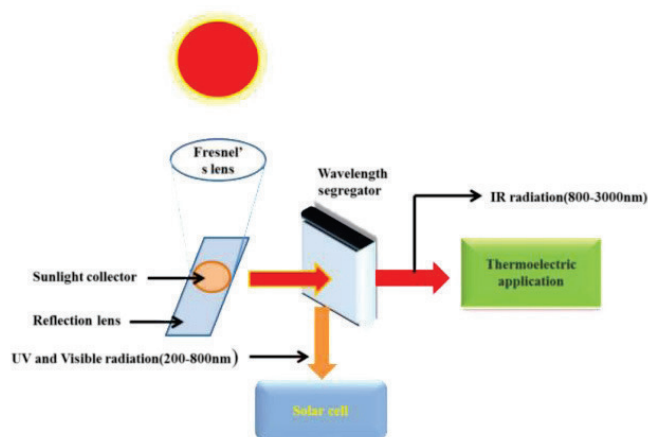


Fig. 1.5 Schematic illustration of PV-TE hybrid system

Approximately 90 per cent of the world's power is generated by heat engines that use fossil fuel combustion as a heat source and typically operate at 30–40 % efficiency, such that roughly 15 TW of heat is lost to the environment [44]. Thermoelectric modules could potentially convert part of this low-grade waste heat to electricity. Thus TE refrigeration is an environmentally “green” method of small scale localized cooling in computers, infrared detectors and in optoelectronic devices. Previously used TE applications include [45]–[47]:

- ✓ TE materials were responsible for power supply during Apollo mission
- ✓ The radioisotope TE generators are the power supplies used in deep-space mission beyond Mars of Naas's Voyager and Cassini missions
- ✓ Thermoelectric- powered radios
- ✓ TE climate control systems

- ✓ TE climate controlled seats that serves as both seat coolers and seat warms are being installed in luxury cars including Ford, GM, Hyundai, Jaguar, Nissan, Range Rover and Toyota
- ✓ Wrist watches marketed by Seiko and Citizen and TE pacemakers are being powered by small temperature differences within the body or between the body and surroundings

Due to the various advantages of no moving parts, long lifespan and quiet operation, thermoelectric devices, have been utilized or attempted to be used in many areas such as automobile, aerospace, industries and domestic sector. The efficiency of conventional thermoelectric modules is far too less to compensate the system cost due to low conversion efficiency, and therefore TEs are more suitable for micro/small applications or some specialized areas. The development of new thermoelectric materials with high efficiency is one of the key factors for expanding the range of thermoelectric applications to the medium/large scale [48].

Heat engine applications:

- ✓ Vehicles and building: Compact thermoelectric units can be installed in the seats, floor, dashboard and overhead for the driver and the front seat occupant. The buildings composited with thermoelectric cooling and heating systems using solar energy to cool rooms in summer and heat rooms in winter via thermoelectric devices and PV-TE system.
- ✓ Medical service and food industry: A portable thermoelectric medical cooling kit controlled by a microprocessor was developed for preserving human blood during transportation.

- ✓ Electronic device: TE refrigeration provides localized cooling in computers, infrared detectors, electronics, and in many other optoelectronics applications which will improve the performance and lifespan of the devices

Power generation applications:

- ✓ Automobile industry: Although an automobile efficiently converts the chemical energy in fossil fuels into mechanical work, a considerable amount of energy is dissipated to the environment through exhaust gas, cooling water, lubricating oils and radiation. Typical exhaust output at normal running speed for a family car is 20–30 kW [49]. Thermoelectric applications on Porsche, truck and passenger cars, and military vehicle have already been studied.
- ✓ Aerospace: Thermoelectric generators can provide electric power in applications such as space, advances in medical physics, deployment of marine and terrestrial surveillance systems and earth resources. For air craft industry thermo- electric device can capture waste heat from the engine and operate over the entire aircraft flight envelope without affecting engine's performance.
- ✓ Industries: The type of thermoelectric material used for industrial applications is dependent on the operating temperature range of the applied areas. In a typical steel plant, the furnace provides a steady source of convenient piped water which can be readily converted by thermo- electric generators into electricity when large amounts of cooling water were discharged at around 90⁰C [48].

- ✓ Domestic application: The houses where wood/diesel/biomass burning stove or other available heating facilities are regularly used have a great potential to generate electrical power using thermoelectric generator.

1.4.2 Development of thermoelectric materials

Initially thermoelectric materials studied were metals, which displays S of only few μVK^{-1} (typically 1-10 μVK^{-1}), and they exhibited small value of ZT even though they have high electrical conductivity. For insulators even though they have large S , their extremely low electrical conductivity results in small value of power factor and thus far small value of ZT than metals. Therefore the key factor of increasing the value power factor and decreasing the thermal conductivity is the development of high performance TE materials. The development of thermoelectricity become interesting when A.F. Ioffe in the 1930's developed thermoelectric semiconductors, which show S of few hundred μVK^{-1} [33].

Figure 1.6 shows the optimization of ZT at 300 K through carrier concentration and table shows the comparison of thermoelectric properties of metals, semiconductors and insulators at 300 K [50]. It is clear from the figure that the optimal TE materials with large value of $S^2\sigma$ is located in the region near the cross over between semiconductor and metal with carrier concentration of 10^{18} - 10^{19} cm^{-3} [31], [51]. Semiconductors and highly doped semiconductors are the class of material for potential TE applications.

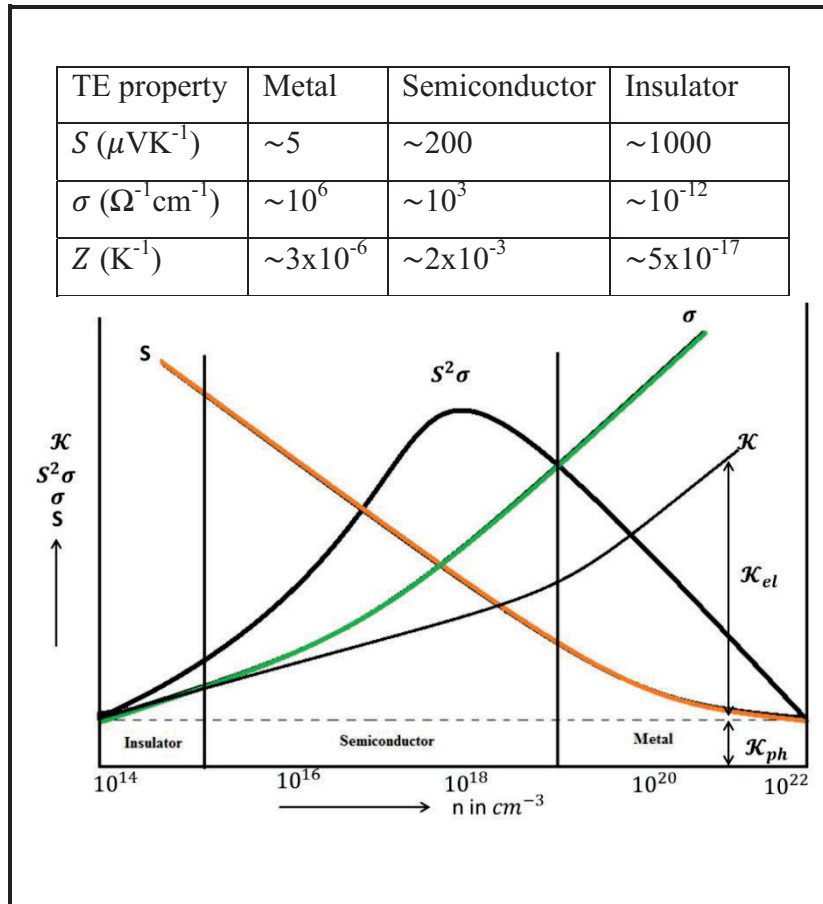


Fig. 1.6 Seebeck coefficient S , electrical conductivity σ , $S^2\sigma$, and electronic (\mathcal{K}_{el}) and lattice (\mathcal{K}_{ph}) thermal conductivity as a function of free charge carrier concentration.

Thus in the middle of the 20th century, interest turned towards semiconductors, as TE materials in which crystal structure and bonding strongly influence the mobility. Therefore alloys based on Pb, Hg, Bi, Ti or Sb and S, Se, or Te systems have been extensively studied and optimized for their

use as thermoelectric materials to perform a variety of solid-state thermoelectric refrigeration and power generation applications [52], [53].

(i) Established materials

Established thermoelectric materials (those which are employed in commercial applications) can be conveniently divided into three groupings with each dependent upon the temperature range of operation [54], [55]. Alloys based on Bi in combinations with Sb, Te or Se are referred to as low temperature materials and can be used at temperatures up to around 450 K. In which the bulk binary chalcogenide semiconductor Bi_2Te_3 , is the most studied and is still today the material with high ZT at room temperature [37]. In Bi_2Te_3 , Bi and Te layers are held together by strong covalent bond whereas adjacent Te layers are held together by weak van der Waals force. This weak binding energy between the Te layers accounts for the ease of cleavage along the plane perpendicular to the c-axis and the anisotropic thermal and electrical transport properties of Bi_2Te_3 [38]. Therefore the thermal conductivity along the plane perpendicular to the c-axis ($1.5 \text{ Wm}^{-1}\text{K}^{-1}$) is nearly twice that of the value along the c-axis direction ($0.7 \text{ Wm}^{-1}\text{K}^{-1}$). Alloying of Bi_2Te_3 could further reduce the thermal conductivity and in general, Bi_2Te_3 and its alloys are good TE materials near room temperature [39].

The intermediate temperature range – up to around 850 K is the regime of materials based on alloys of Pb while thermoelements employed at the highest temperatures are fabricated from silicon germanium alloys and operate up to 1300 K. Neither Si nor Ge is a good TE material, as the lattice thermal conductivity is very large ($150 \text{ Wm}^{-1} \text{K}^{-1}$ for Si and $63 \text{ Wm}^{-1}\text{K}^{-1}$ for Ge) [56].

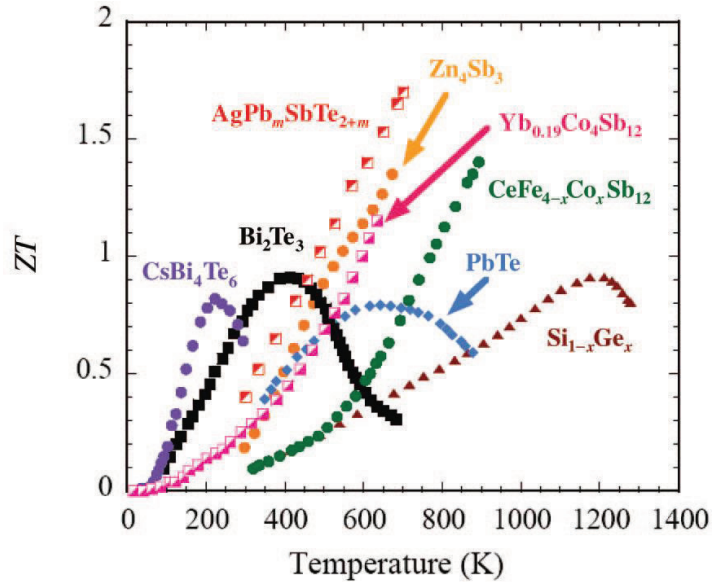


Fig. 1.7 A plot of the figure of merit (ZT) as a function of temperature for several bulk thermoelectric materials [57].

In contrast to Bi_2Te_3 , the isotropic lead telluride (PbTe) crystallizes in a cubic NaCl- type crystal structure with good TE properties in temperature range of 300-700 K [58]. Thus group IV telluride such as PbTe , GeTe or SnTe are typically used for mid temperature power generation (500-900 K). For high temperature (>900 K) TE generation, silicon, germanium alloys are typically used as n and p legs of TE devices. The ZT of this p-type material is fairly low because of high lattice thermal conductivity of the diamond structure [56]. The ZT values as a function of temperature for some bulk commercially available thermoelectric materials are shown in figure 1.7. Difficulties in increasing ZT in bulk materials is as σ increases S decreases and \mathcal{K} increases

Figure 1.7 shows the current thermoelectric materials having $ZT \approx 1$ and these exhibit conversion efficiencies of 7% - 8% depending on the specific bulk materials and the temperature differences involved. Thus the first generation thermoelectric materials, such as Bi_2Te_3 , PbTe and SiGe bulk thermoelectric materials were developed for applications at room temperature, intermediate temperature and high temperature, respectively and have shown a maximum ZT value about 1, which restricts the large-scale application of thermoelectric technology. Although the above mentioned materials still remain the cornerstone for commercial/practical applications in thermoelectric generation, significant advances have been made in 1990s to synthesise new materials and fabricate material structures with enhanced ZT . The benchmark of $ZT \approx 1$ was broken by two approaches: the first methodology is the development “phonon glass electron crystals” (PGECs) which are ideal thermoelectric materials having glass-like thermal conductivity and crystal-like electronic properties [59]. Typical examples of PGEC thermoelectric materials are skutterudites and the clathrates. The search for these materials is mainly motivated by the suggestion of Slack [60]. In typical PGEC materials, high mobility electrons are able to transport charge and heat freely, while the phonons are disrupted at the atomic scale from transporting heat. Generally, these materials contain a large amount of large interstitial sites filled with other element atoms, which act as “rattler” atoms that vibrate at low frequencies and consume thermal energy. Therefore, the PGEC materials act like a crystal for electrons while still efficiently scatter phonons, rendering these materials retaining high electrical conductivities and also obtaining low thermal

conductivities [36]. As a consequence, the thermal conductivity of skutterudites and clathrates can be reduced greatly while maintaining the electrical conductivity at a high level [61]. The other methodology is the nanostructuring of thermoelectric materials, which suggests that the ZT enhancement can be realized with nanoscale or nanostructured morphologies [36]. In low-dimensional material systems, the power factor can be enhanced through the use of quantum confinement effects.

(ii) New materials

Some of the recently developed materials under investigation include skutterudites [62]–[64], clathrates [65]–[68], half-Heusler alloys [69][70][71], complex chalcogenides [72]–[75], complex oxide materials [76], thin film superlattice structures [77] and nano structured materials [78]–[81]. Herein an overview of most recent thermoelectric materials is done.

Skutterudites

The skutterudites-type structure (CoAs_3 - type) is a cubic structure and contains 32 atoms per unit cubic cell (the skutterudite structure is indicated by MX_3 with $M = \text{Co, Rh, Ir}$; $X = \text{P, As, Sb}$). When atoms are placed into the interstitial voids or cages of these materials, the lattice thermal conductivity can be substantially reduced compared with that of un filled skutterudites; at the same time, the materials still have good electrical properties, thus the thermoelectric properties can be enhanced significantly [64].

Clathrates

Clathrates has open structures to host loosely bounded guest atoms and are generally low-thermal conductivity compounds ($\sim 1 \text{ Wm}^{-1}\text{K}^{-1}$ at room

temperature, that is comparable to that of amorphous germanium) in which tetrahedrally bonded atoms (typically Ge, Si, or Sn) form a framework of cages that enclose relatively large metal atoms. There are two main types of structure the so-called Type I and Type II [66], [82]. The Type I structures can be represented by the general formula $X_2Y_6E_{46}$ in which X and Y are guest atoms and E is Si, Ge or Sn and the Type II structures can be represented as $X_{24}E_{100}$ [54].

Half-Heusler alloys

Half-Heusler (HH) alloy possesses a cubic structure consisting of three interpenetrating FCC sublattices and one vacant sublattice, with high thermal stability and environmental friendliness. These intermetallic compounds can be represented by the chemical formula XYZ where X and Y are transition metals and Z is a main-group element [65]. Several HH alloys have been investigated to improve their thermoelectric properties and the most attractive feature of HH alloys as promising thermoelectric materials is the large room-temperature Seebeck coefficient of approximately $100 \mu \text{VK}^{-1}$ and high electrical conductivities of around $1000\text{--}10000 \text{ Scm}^{-1}$ [54]. In this ZnNiSn is the most intensively investigated member.

β -Zn₄Sb₃

β -Zn₄Sb₃ is a *p*-type intermetallic compound with hexagonal rhombohedral crystal structure [83]. Both single-crystal and polycrystalline samples of β -Zn₄Sb₃ have been investigated. Its high efficiency results from an extraordinarily low thermal conductivity in conjunction with the electronic structure of a heavily doped semiconductor [84].

Complex chalcogenides

Chalcogenide materials have had a prominent position in the field of thermoelectricity because of their versatility in combination with other elements and the small variation in electronegativity between sulfur, selenium, and tellurium, it is possible to obtain semiconductors with energy gaps appropriate for TE applications over a wide range of temperature [85].

Metal oxides

Not only metal oxides possess a high conversion efficiency, but they must also be composed of nontoxic and abundantly available elemental materials having high chemical stability in air, even at temperatures of 800–1000 K. The layered NaCo_2O_4 has a large enough thermopower and metal-like conductivity. The reported ZT values of TE oxides are given in table. Unfortunately, conversion efficiency of modules using oxides is lower than conventional TE modules. In order to enhance the thermoelectric properties of oxide modules, new materials with higher ZT values are to be investigated.

Thin film superlattice

Superlattices, are anisotropic, consist of alternating thin layers of different materials stacked periodically. The lattice mismatch and electronic potential differences at the interfaces and resulting phonon and electron interface scattering and band structure modifications showed the large figure-of-merit enhancements in V–VI- and IV–VI-based superlattices and quantum dot superlattices. The enhancement in ZT in these materials appears to be more from a reduction in the lattice thermal conductivity than an increase in power factor.

	Material	ZT (Wm ⁻¹ K ⁻¹)	\mathcal{K}_L (W m ⁻¹ K ⁻¹)	T
Skutterudites	Yb _{0.19} Co ₄ Sb ₁₂	1		600K
	Ba _{0.30} Ni _{0.05} Co _{3.95} Sb ₁₂	1.25		900K
	Ca _{0.18} Ni _{0.03} Co _{3.97} Sb _{12.4}	1		800K
	BaxCo ₄ Sb ₁₂	0.45		800K
Clathrates	Sr ₈ Ga ₁₆ Ge ₃₀	0.5		R T
	Ba ₈ In ₁₆ Sn ₃₀	1.7		800K
	Ba ₈ Ga ₁₆ Ge ₃₀	0.7		700K
	Ba ₈ Ga ₁₆ Si ₃₀	0.87		870K
	Eu ₈ Ga ₁₆ Ge ₃₀	0.3		400K
Half-Heusler Intermetallic Compounds	Zr _{0.5} Hf _{0.5} Ni _{0.8} Pd _{0.2} Sn _{0.99} Sb _{0.01}	0.7		800K
	(Zr _{0.5} Hf _{0.5}) _{0.5} Ti _{0.5} NiSn _{1-y} Sb _y	1.4		700K
	Hf _{0.75} Zr _{0.25} NiSn _{0.975} Sb _{0.025}	0.81		1025K
β -Zn ₄ Sb ₃ alloys	β -Zn ₄ Sb ₃	1.4	0.9	673K
	Hf _{0.60} Zr _{0.25} Ti _{0.15} NiSn _{0.975} Sb _{0.025}	6.4		
	Hf _{0.75} Zr _{0.25} NiSn _{0.975} Sb _{0.025}	0.81		1025 K
Metal Oxides	polycrystalline NaCo ₂ O ₄	0.8		1000 K
	single-crystal NaCo ₂ O ₄	1		800 K
	SrTiO ₃ , heavily doped with Nb	0.37		1000K
	SrTiO ₃ , heavily doped with La	0.26		1000K
	SrO(SrTiO ₃) ₂	0.012		
Chalcogenide Compounds	Tl ₉ BiTe ₆	1.2	0.39	500K
	AgPb _m SbTe _{m+2}	1.7		700K
	PbTe	0.8		773K
	Tl ₂ SnTe ₅	1		500K
2D Materials: quantum well or superlattices	PbSeTe/PbTe	2.0	0.58	RT
	Bi ₂ Te ₃ /Sb ₂ Te ₃	2.4	0.22	300K
	PbTe/PbSnSeTe	2.0		RT
Bi ₂ Te ₃ -based nanocomposites	Bi _{0.4} Sb _{1.6} Te ₃	1.8		316K
	BiSbTe	1.4		373K
	Bi ₂ Te ₃ n 10.3450K	1	0.3	450K
PbTe-based nanocomposites	AgPb ₁₈ SbTe ₂₀	2.2		800K
	Na _{0.95} Pb ₂₀ SbTe ₂₂	1.7	0.74	700K
	Ag _{0.8} Pb _{22.5} SbTe ₂₀	1.5	0.89	700K
New thermoelectric materials	In ₄ Se _{3-x} Cl _{0.03}	1.53		698K
	β -Cu _{2-x} Se	1.5	0.4	1000K
	In ₄ Se _{3-x}	1.48		705K

Table 1.2 Thermoelectric Properties of material systems at different temperatures.

Nanostructured Materials

Nano structured thermoelectric materials are believed to have higher thermoelectric properties than their bulk, because nanostructuring can enhance the density of states (DOS) near Fermi level via quantum confinement and therefore increase the thermopower, which provides a way to decouple thermopower and electrical conductivity and/or because mean free path (mfp) of electrons is much shorter than that of photons in heavily doped semiconductors, nanostructuring serves to introduce a large density of interfaces in which phonons over a large mfp range can be scattered more effectively and preferentially than electrons, hence reducing the lattice thermal conductivity effectively while preserving carrier mobility and electronic conduction [86]–[88]. Significant ZT enhancement has been found in two-dimensional (2D) including superlattices and quantum well materials and one dimensional (1D) thermoelectric materials. Table 1.2 gives a brief review of various thermoelectric material systems synthesized by various deposition methods in the past two decades

Tirtt *et. al.* proved that a value of $ZT > 4$ does not significantly increase the conversion efficiency over that of a material with $ZT = 2 - 3.5$ [57]. Thus recent reports indicate that, a large number of studies have focused on the development of TE materials based on chalcogenide compounds with a ZT value of the order of 2 - 3 as these materials are predominantly semiconducting, environmentally stable and have high melting point. The low thermal conductivity of chalcogenides also a key property that leads to high ZT values for these materials. Because of their versatility in combination with

other elements and the small variation in electronegativity between sulfur, selenium, and tellurium, it is possible to obtain semiconductors with energy gaps appropriate for thermoelectric applications over a wide range of temperature. The development of new TE material with large ZT and cheap price could make a big breakthrough for the application areas.

1.5 Role of chalcogenide thin film in PV and TE applications

Due to the great potential of power generation by using solar radiation and any other kinds of possible heat sources as well as the reliable long period maintenance-free operation, thermo- electric generators/coolers have become technically attractive. It is very suitable for power generation by using solar radiation and recovering heat from waste heat sources due to the low cost or free use. Moreover, solid-state Peltier coolers provide precise thermal management for optoelectronics devices and can act seat coolers/ warmers in automobiles. Relevant investigations have been carried out to seek for optimum and sustainable way so fusing them to the maximum level. The future expansion of many of the alternative energy technologies such as thermoelectrics and PV is tied primarily to enhanced materials performance along with better device design. In order to make the PV and TE applications more economically feasible, and environmentally beneficial, increasing efforts have been made to discover and develop high-performance materials, including bulk, film and nanowire materials. In which thin film technology allows an enlarged choice of the type of substrate and possibility of patterning the devices to micro or sub-micro dimensions. Moreover thin films greatly reduce the amount of semiconductor material in a module and hence lower the

cost of production of a device especially in waste heat or solar energy conversion technology. Preparation of chalcogenide materials in thin film form is highly required because of their potential application in the micro-fabrication of integrated TE devices and its flexibility in installation.

1.6 Aim and objective of the present work

Today we predominantly depend on fossil fuels (i.e. coal, oil and gas) and with the addition of electricity from nuclear power to meet our energy demands. The present global primary energy consumption (GPEC) is ~ 15 TW [89]. The conventional fossil-fuel are being quickly dwindling because of the insufficient fossil fuel supplies due to global population growth and economic development and the consequent record-high oil and gas prices [15]. Moreover, CO₂ emissions from the combustion of fossil fuels have significantly raised the concentration of CO₂ in the atmosphere. If the burning fossil fuel continues, it will enhance greenhouse gases emissions into the atmosphere, trapping the sun's heat and contributing to global warming [90], [91]. Climate scientists generally agree that the Earth's average temperature has risen in the past century. If this trend continues, sea levels will rise, and scientists predict that floods, heat waves, droughts, and other extreme weather conditions could occur more often [92].

Nuclear energy has a great establishment cost along with a number of safety concerns. Jacobson and Delucchi reported that the growth of nuclear energy has historically increased the ability of nations to obtain or enrich uranium for nuclear weapons and a large-scale worldwide increase in nuclear energy facilities would exacerbate this problem, putting the world at greater

risk of a nuclear war or terrorism catastrophe [93]. Nuclear energy also results in carbon emissions, in part due to emissions from uranium refining and transport and reactor construction, in part due to the longer time required to site, permit, and construct a nuclear plant, and in part due to the greater loss of soil carbon due to the greater loss in vegetation resulting from covering the ground with nuclear facilities. In addition, accidents at nuclear power plants have been either catastrophic or damaging and conventional nuclear power produces radioactive waste, which must be stored for thousands of years, raising technical and long-term cost questions. Therefore global environmental considerations linked with the global warming from greenhouse gas emissions due to increasing fossil fuel consumption/ CO_2 and ever-increasing demand for energy has opened up new opportunities for the utilization of renewable energy technologies [94].

Renewable energy uses energy sources that are continually replenished by nature—the sun, the wind, water, the Earth’s heat, and plants. We often call renewable energy technologies as “clean” or “green” technologies and they have started to play an important role in tackling the energy and environment issues arising in this technology oriented world [48]. The hydroelectric power plants are inexpensive but have a limited life span and mostly cannot be utilized due to seasonal irregularity of available water [95]. As a renewable energy source, the Sun is the oldest and most potent source of energy and life known to humanity.

With regard to solar energy utilisation and waste heat energy recovery, a significant improvement in performance of both PV and TE module can be

achieved by new developments in materials. The chalcogenide semiconducting thin films are good candidates for fabricating multi-junction solar cells for two reasons: they can be grown with excellent material quality; and their band gaps span a wide spectral range, mostly with direct band gaps, implying a high absorption coefficient. The enhanced interest in new TE materials has been driven by the need for enhancing the efficiency of thermoelectric devices (increase ZT) and has the capability of operating in new and broader temperature regimes. At low temperatures (below the Debye temperature) C_v and then \mathcal{K}_{ph} is directly proportional to T^3 . At this temperature phonon scattering is insignificant, because of low number of excited phonons and their very long wavelength. At above Debye temperature, C_v is a constant, making \mathcal{K}_{ph} primarily depend on mean free path which is determined by phonon-phonon scattering. The lattice thermal conductivity due to phonon-phonon scattering is related material property as [96]:

$$\mathcal{K}_{ph} \propto \frac{T_m^{3/2} \rho^{2/3}}{T \gamma^2 A_m^{7/6}} \quad (1.19)$$

where A_m is average atomic mass, ρ is the density, T_m is the melting point temperature, γ is the Gruneisen parameter which is a direct measure of the anharmonicity of a bond. Reducing \mathcal{K}_{ph} is an efficient way to enhance the TE performance. That is a low melting point, large atomic weight, large interatomic distance add/or large Grüneisen parameter lead to low thermal conductivity. High performance in TE materials with intrinsically low thermal conductivity may arise from large molecular weight, complex crystal structure, weak chemical bonding, ion liquid-like transport behavior, anharmonicity or

anisotropic bonding [97]. Taking into account of above facts, present work focuses on preparation and characterization of chalcogenide thin films for TE and PV applications using cost-effective technique in order to fulfill the world's future energy needs.

References

- [1] R. A. Smith, *Semiconductors*. Academic publishers, 1989.
- [2] K. Seeger, *Semiconductor physics- An introduction*. Springer, 2004.
- [3] J. Singh, *Semiconductor devices and basic principles*. John Wiley and sons, 2001.
- [4] K. L. Chopra, *Thin film phenomena*. Mc Graw. Hill Inc., 1969.
- [5] D. A. Jameel, "Thin Film Deposition Processes," *Am. Inst. Sci.*, vol. 1, no. 4, pp. 193–199, 2015.
- [6] Neil G. Connelly, Ture Damhus, Richard M. Hartshorn and Alan T. Hutton, "*Nomenclature of Inorganic Chemistry: IUPAC Recommendations 2005*," RSC Publishing.
- [7] W. Fischer, "A Second Note on the Term 'Chalcogen,'" *J. Chem. Educ.*, vol. 78, pp. 1333, 2001.
- [8] W. B. Jensen, "A Note on the Term 'Chalcogen,'" *J. Chem. Educ.*, vol. 74, no. 9, pp. 1063–1064, 1997.
- [9] S. M. Ho, P. Nilai, and N. Sembilan, "Review Article Chalcogenide Thin Films Prepared using Chemical Bath Deposition Method: Review," *Res. J. Appl. Sci. Eng. Technol.*, vol. 11, no. 10, pp. 1058–1065, 2015.

- [10] “<http://iupac.org>.” .
- [11] H. Soonmin and T. J. S. Anand, “A Review of Chalcogenide Thin Films for Solar Cell Applications,” *Indian J. Sci. Technol.*, vol. 8, pp. 67499 1–6, 2015.
- [12] H. O. Soonmin, “Power conversion efficiency in thin film Solar cell: a review,” *Int. J. Chem. Sci.*, vol. 14, no. 1, pp. 143–151, 2016.
- [13] D. Shikha, J. K. Sharma, and J. Sharma, “Review on Effect of Deposition Parameters and Annealing on Structural Properties of Nanocrystalline MSe Thin Films by Chemical bath Deposition,” *Sch. J. Eng. Tech.*, vol. 2, no. 5B, pp. 761–768, 2014.
- [14] Papadopoulou and V. M. Elena, *Photovoltaic Industrial Systems An Environmental Approach*, Springer, 2011.
- [15] K. Yu and A. J. Chen, “Enhancing Solar Cell Efficiencies through 1-D Nanostructures,” *Nanoscale Res.Lett*, vol. 4, pp. 1–10, 2009.
- [16] I. W. Siiocklev and W. T. Read, “Statistics of the Recombinations of Holes and Electrons,” *Phys. Rev.*, vol. 87, pp. 835–842, 1952.
- [17] F. Dimroth and S. Kurtz, “High - Efficiency Multijunction Solar cells,” *MRS Bull.*, vol. 32, pp. 230–235, 2007.
- [18] A. Shah, P. Torres, R. Tscharnner, N. Wyrsh, and H. Keppner, “Photovoltaic Technology: The Case for Thin-Film Solar Cells,” *Science*, vol. 285, pp. 692–698, 2000.
- [19] M. A. Green, K. Emery, Y. Hishikawa, and W. Warta, “Solar cell efficiency tables (version 37),” *Prog. Photovolt. Res. Appl.*, vol. 19, pp. 84–92, 2011.

- [20] T. Saga, “Advances in crystalline silicon solar cell technology for industrial mass production,” *NPG Asia Mater.*, vol. 2, pp. 96–102, 2010.
- [21] B. Parida, S. Iniyar, and R. Goic, “A review of solar photovoltaic technologies,” *Renew. Sustain. Energy Rev.*, vol. 15, pp. 1625–1636, 2011.
- [22] G. Conibeer, “photovoltaics,” *Mater. Today*, vol. 10, pp. 42–50, 2007.
- [23] M. Afzaal, P. O. Brien, and P. O. Brien, “Recent developments in II – VI and III – VI semiconductors and their applications in solar cells,” *J. Mater. Chem.*, vol. 16, pp. 1597–1602, 2006.
- [24] “<http://www.nrel.gov/ncpv>.” .
- [25] B. Srinivas, S. Balaji, M. Nagendra Babu and Y. Subba Reddy “Review on present and advance materials for solar cells,” *Int. J. Eng. Res. Online*, vol. 3, pp. 178–182, 2015.
- [26] Richard Bube, *Fundamentals of Solar Cells: Photovoltaic Solar Energy Conversion*, Academic press, 1983
- [27] Terry M. Tritt, Böttner Harald and Lidong Chen, “Thermoelectrics : Direct Solar Thermal Energy Conversion,” *MRS Bull.*, vol. 33, pp. 366–368, 2008.
- [28] M. Fisac, F. X. Villasevil, and A. M. López, “High-efficiency photovoltaic technology including thermoelectric generation,” *J. Power Sources*, vol. 252, pp. 264–269, 2014.
- [29] Y. Li, S. Witharana, H. Cao, M. Lasfargues, and Y. Huang, “Particuology Wide spectrum solar energy harvesting through an integrated photovoltaic and thermoelectric system,” *Particuology*, vol. 15, pp. 39–44, 2014.

- [30] K. Park, S. Shin, A. S. Tazebay, H. Um, and J. Jung, “Photovoltaic and thermoelectric devices,” *Sci. Reports*, vol. 3, pp. 1–6, 2013.
- [31] A. Shakouri, “Recent Developments in Semiconductor Thermoelectric Physics and Materials,” *AIP Conf. Proc.*, vol. 41, pp. 399–431, 2011.
- [32] W. Brostow, G. Granowski, N. Hnatchuk, J. Sharp, J. B. White and M. Industries, “Thermoelectric phenomena,” *J. Mater. Educ.*, vol. 36, pp. 175–186, 2014.
- [33] A. Bulusu and D. G. Walker, “Review of electronic transport models for thermoelectric materials,” *Superlattices Microstruct.*, vol. 44, pp. 1–36, 2008.
- [34] C. Wood, “Materials for thermoelectric energy conversion,” *Rep. Prog. Phys.*, vol. 51, pp. 459–539, 1988.
- [35] D. MacDonald, *Thermoelectricity: An Introduction to the Principles*. Dover Publications, New York, 2006.
- [36] Z. Chen, G. Han, L. Yang, L. Cheng, and J. Zou, “Nanostructured thermoelectric materials: Current research and future challenge,” *Chinese Mater. Res. Soc.*, vol. 22, pp. 535–549, 2012.
- [37] D. M. Rowe, *CRC Handbook of Thermoelectrics*. CRC, Boca Raton, FL, 1995.
- [38] D. M. Rowe, *Thermoelectrics Handbook: Macro to Nano*. CRC/Taylor & Francis, Boca Raton, FL, 2006.
- [39] X. Zhang and L. Zhao, “Thermoelectric materials: Energy conversion between heat and electricity,” *J. Mater.*, vol. 1, no. 2, pp. 92–105, 2015.
- [40] Arash Mehdizadeh Dehkordi, Mona Zebarjadi, Jian He and T. M. Tritt,

- “Thermoelectric power factor : Enhancement mechanisms and strategies for higher performance thermoelectric materials strategies for higher performance thermoelectric materials,” *Mater. Sci. Eng. R*, vol. 97, pp. 1–22, 2015.
- [41] T. Ursell, G. J. Snyder, and T. S. Ursell, “Thermoelectric Efficiency and Compatibility,” *Phys. Rev. Lett.*, vol. 91, pp. 10–14, 2016.
- [42] H. B. Kwok, “Thermoelectric and photothermoelectric effects in semiconductors: CdS single crystals,” *J. Appl. Phys.*, vol. 44, no. 1, pp. 138–144, 1973.
- [43] C. Kittel, *Introduction to Solid State Physics*. Wiley, New York, 2005.
- [44] A. I. Hochbaum, R. Chen, R. D. Delgado, W. Liang, E. C. Garnett, and M. Najarian, “Enhanced thermoelectric performance of rough silicon nanowires,” *Nanoscale Res.Lett*, vol. 451, pp. 163–167, 2008.
- [45] D. M. Rowe, “Review Thermoelectric Waste Heat Recovery as a Renewable Energy Source,” *Int. J. Innov. Energy Syst. Power*, vol. 1, pp. 13–23, 2006.
- [46] J. Yang and T. Caillat, “Thermoelectric Materials for Space,” *MRS Bull.*, vol. 31, pp. 224–229, 2006.
- [47] G. J. Snyder, “Small Thermoelectric Generators,” *Electrochem. Soc. Interface*, pp. 54–56, 2008.
- [48] X. F. Zheng, C. X. Liu, Y. Y. Yan, and Q. Wang, “A review of thermoelectrics research – Recent developments and potentials for sustainable and renewable energy applications,” *Renew. Sustain. Energy Rev.*, vol. 32, pp. 486–503, 2014.
- [49] S. B. Riffat and X. Ma, “Thermoelectrics : a review of present and

- potential applications,” *ISRN Renew. Energy*, vol. 23, pp. 913–935, 2003.
- [50] J. Zheng, “Recent advances on thermoelectric materials,” *Front. Phys. China*, vol. 3, pp. 269–279, 2008.
- [51] Z. Chen, G. Han, L. Yang, L. Cheng, and J. Zou, “Progress in Natural Science: Materials International Nanostructured thermoelectric materials : Current research and future challenge,” *Chinese Mater. Res. Soc.*, vol. 22, pp. 535–549, 2012.
- [52] J. Nolas, G. S. Sharp and J. Goldsmid, *Thermoelectrics Basic Principles and New Materials Developments*. Springer Verlag Berlin Heidelberg, 2001.
- [53] A. P. Gonçalves and C. Godart, “New promising bulk thermoelectrics: Intermetallics, pnictides and chalcogenides,” *Eur. Phys. J. B.*, vol. 87, pp. 1–29, 2014.
- [54] J. R. Sootsman, D. Y. Chung, and M. G. Kanatzidis, “New and Old Concepts in Thermoelectric Materials Angewandte,” *Reviews*, vol. 48, pp. 8616–8639, 2009.
- [55] H. J. Goldsmid and J. Sharp, “Extrapolation of Transport Properties and Figure of Merit of a Thermoelectric Material,” pp. 6451–6467, 2015.
- [56] T. M. Tritt and M. A. Subramanian, “Thermoelectric Materials , Phenomena , and Applications : A Bird ’ s Eye View,” *MRS Bull.*, vol. 31, pp. 188–198, 2006.
- [57] J. T. Jarman, E. E. Khalil, and E. Khalaf, “Energy Analyses of Thermoelectric Renewable Energy Sources,” *Open J. Energy Effic.*, vol. 2, pp. 143–153, 2013.

- [58] J. He, M. G. Kanatzidis, and V. P. Dravid, “High performance bulk thermoelectrics via a panoscopic approach,” *Mater. Today*, vol. 16, pp. 166–176, 2013.
- [59] T. M. Tritt, “Focus on Thermoelectrics and Nanomaterials,” *Phys. status solidi – Rapid Res. Lett.*, vol. 1, pp. A91–A92, 2007.
- [60] G. A. Slack, *CRC Handbook of Thermoelectrics*(Ed.: D. M. Rowe). CRC, Boca Raton, FL, 1995.
- [61] J. Li, W. Liu, L. Zhao, and M. Zhou, “High-performance nanostructured thermoelectric materials,” *NPG Asia Mater.*, vol. 2, pp. 152–158, 2010.
- [62] G. S. Nolas, M. Kaeser, R. T. Littleton and T. M. Tritt, “High figure of merit in partially filled ytterbium skutterudite materials,” *Appl. Physics Letters*, vol. 77, pp. 1855–1857, 2000.
- [63] X. Shi, J. Yang, J. R. Salvador, M. Chi, J. Y. Cho, H. Wang et. al., “Multiple-filled skutterudites: High thermoelectric figure of merit through separately optimizing electrical and thermal transports,” *J. Am. Chem. Soc. Chem. Soc.*, vol. 133, pp. 7837–7846, 2011.
- [64] G. S. Nolas and T. M. Tritt, “SKUTTERUDITES : A Phonon-Glass-Electron Crystal Approach to Advanced Thermoelectric Energy Conversion Applications,” *Annu. Rev. Mater. Sci.*, vol. 29, pp. 89–116, 1999.
- [65] T. Si, “Prediction of Giant Thermoelectric Power,” *Sci. Reports*, vol. 4, pp. 1–5, 2014.
- [66] T. Takabatake and K. Suekuni, “Phonon-glass electron-crystal thermoelectric clathrates : Experiments and theory,” *Rev. Mod. Phys.*, vol. 86, pp. 669–716, 2014.

- [67] G. S. Nolas, J. L. Cohn, G. A. Slack, and S. B. Schujman, "Semiconducting Ge clathrates: Promising candidates for thermoelectric applications Semiconducting Ge clathrates: Promising candidates for thermoelectric applications," *Appl. Physics Letters*, vol. 73, pp. 178–180, 2016.
- [68] G. S. Nolas, and G. A. Slack, "Thermoelectric Clathrates," *Sigma Xi, Sci. Res. Soc.*, vol. 89, pp. 136–141, 2016.
- [69] J. W. Simonson, D. Wu, W. J. Xie, T. M. Tritt, and S. J. Poon, "Introduction of resonant states and enhancement of thermoelectric properties in half-Heusler alloys," *Phys. Rev. B - Condens. Matter Mater. Phys.*, vol. 83, pp. 235211, 2011.
- [70] T. M. Tritt, "Holey and Unholey Semiconductors," *Science*, vol. 283, no. 1999, pp. 804–805, 1999.
- [71] George S. Nolas, J. Kanatzidis and Mercouri, "Recent Developments in Bulk Thermoelectric Materials," *MRS Bull.*, vol. 31, pp. 199–205, 2006.
- [72] D. Chung, T. Hogan, P. Brazis, M. Rocci-lane, C. Kannewurf, M. Bastea, C. Uher, and M. G. Kanatzidis, "CsBi₄Te₆: A High-Performance Thermoelectric Material for Low-Temperature Applications," *Science*, vol. 287, pp. 1024–1027, 2000.
- [73] Y. Pei, X. Shi, A. Lalonde, H. Wang, L. Chen, and G. J. Snyder, "Convergence of electronic bands for high performance bulk thermoelectrics," *Nature*, vol. 473, pp. 66–69, 2011.
- [74] N. Chen, F. Gascoin, G. J. Snyder, E. Müller, G. Karpinski, C. Stiewe, N. Chen, F. Gascoin, and G. J. Snyder, "Macroscopic thermoelectric inhomogeneities in (AgSbTe₂)_x(PbTe)_{1-x}," *Appl. Physics Letters*, vol. 87, pp. 171903, 2005.

- [75] S. D. Mahanti, P. Larson, Duck-Young Chung, S. Sportouch and M. G. Kanatzidis, "Electronic structures of complex chalcogenides and other narrow band gap thermoelectric materials," *Mat. Res. Soc. Symp. Proc.*, vol. 545, p. 23, 1999.
- [76] Kunihiro Koumoto, I. T. Funahashi and Ryoji, "Complex Oxide Materials for Potential Thermoelectric Applications," *MRS Bull.*, vol. 31, pp. 206–210, 2006.
- [77] G. C. Harald Böttner and R. Venkatasubramanian, "Aspects of Thin-Film Superlattice Thermoelectric Materials, Devices, and Applications," *MRS Bull.*, vol. 31, pp. 211–217, 2006.
- [78] M. G. Kanatzidis, "Nanostructured Thermoelectrics: The New Paradigm," *Chem. Mater. Rev.*, vol. 22, pp. 648–659, 2010.
- [79] C.J. Liu, T. M. Tritt, J. He, Y. Liu, Y.L. Liu, and D. Hitchcock, "Low temperature thermoelectric properties and aging phenomena of nanostructured p-type $\text{Bi}_{2-x}\text{Sb}_x\text{Te}_3$ ($x=1.46, 1.48, 1.52$ and 1.55)," *Funct. Mater. Lett.*, vol. 06, p. 1340008, 2013.
- [80] W. Xie, S. Wang, S. Zhu, J. He, X. Tang, Q. Zhang, and T. M. Tritt, "High performance Bi_2Te_3 nanocomposites prepared by single-element-melt-spinning spark-plasma sintering," *J. Mater. Sci.*, vol. 48, no. 7, pp. 2745–2760, 2013.
- [81] L.H. Ye, K. Hoang, A. J. Freeman, S. D. Mahanti, J. He, T. M. Tritt, and M. G. Kanatzidis, "First-principles study of the electronic, optical, and lattice vibrational properties of AgSbTe_2 ," *Phys. Rev. B*, vol. 77, p. 245203, 2008.
- [82] G. S. Nolas, J. L. Cohn, G. A. Slack, and S. B. Schujman, "Semiconducting Ge clathrates: Promising candidates for thermoelectric applications," *Appl. Physics Letters*, vol. 73, no. 2, pp.

- 178–180, 1998.
- [83] T. Caillat, J. P. Fleurial and A. Borshchevsky, “Preparation and thermoelectric properties of semiconducting Zn_4Sb_3 ,” *J. Phys. Chem. Solids*, vol. 58, no. 1997, pp. 1119–25.
- [84] G. J. Snyder, M. Christensen, E. Nishibori, T. Caillat, and B. O. B. Iversen, “Disordered zinc in Zn_4Sb_3 with phonon-glass and electron-crystal thermoelectric properties,” *Nat. Mater.*, vol. 3, no. July, pp. 458–463, 2004.
- [85] C. Chen, H. Wang, Y. Chen, and G. Je, “Thermoelectric properties of p-type polycrystalline SnSe doped with Ag,” *J. of Materials Chemistry A*, vol. 2, pp. 11171–11176, 2014.
- [86] J. R. Szczech, J. M. Higgins and S. Jin, “Enhancement of the thermoelectric properties in nanoscale and nanostructured materials, *J. of Materials Chemistry*,” *J. Mater. Chem.*, vol. 21, pp. 4037–4055, 2011.
- [87] S. K. Bux, J. P. Fleurial and R. B. Kaner, “Nanostructured materials for thermoelectric applications,” *Chem. Commun.*, vol. 46, pp. 8311–8324, 2010.
- [88] Apparao M. Rao, Xiaohua Ji and Terry M. Tritt, “Properties of Nanostructured One-Dimensional and Composite Thermoelectric Materials,” *MRS Bull.*, vol. 31, pp. 218–223, 2006.
- [89] H. Cotal, C. Fetzer, J. Boisvert, G. Kinsey, R. King, P. Hebert, and H. Yoon, “III – V multijunction solar cells for concentrating photovoltaics,” *Energy Environ. Sci.*, vol. 2, pp. 174–192, 2009.
- [90] M. I. Hoffert, M. I. Hoffert, K. Caldeira, G. Benford, D. R. Criswell, C. Green, H. Herzog, A. K. Jain, H. S. Kheshgi, K. S. Lackner, J. S. Lewis, H. D. Lightfoot, W. Manheimer, and J. C. Mankins, “Advanced

- Technology Paths to Global Climate Stability : Energy for a Greenhouse Planet,” *Science*, vol. 298, pp. 981–987, 2008.
- [91] H. Turton and L. Barreto, “Long-term security of energy supply and climate change,” *Energy Policy*, vol. 34, pp. 2232–2250, 2006.
- [92] C. S. Kaunda, C. Z. Kimambo, and T. K. Nielsen, “Hydropower in the Context of Sustainable Energy Supply : A Review of Technologies and Challenges,” *ISRN Renew. Energy*, vol. 2012, pp. 1–15, 2012.
- [93] M. Z. Jacobson and M. A. Delucchi, “Providing all global energy with wind , water , and solar power , Part I: Technologies, energy resources , quantities and areas of infrastructure and materials,” *Energy Policy*, vol. 39, no. 3, pp. 1154–1169, 2011.
- [94] A. Bauen, “Future energy sources and systems — Acting on climate change and energy security,” *J. Power Sources*, vol. 157, pp. 893–901, 2006.
- [95] A. Khaligh and O. G. Onar, *Energy harvesting Solar, Wind, and Ocean Energy Conversion Systems*. CRC Press Taylor & Francis Group, New York, 2010.
- [96] R. W. Keves, “High-Temperature Thermal Conductivity of Insulating Crystals: Relationship to the Melting Point,” *Physical Rev.*, vol. 115, pp. 56-567, 1959.
- [97] X. Zhang and Li-Dong Zhao, “Thermoelectric materials : Energy conversion between heat and electricity,” *J. Materiomics*, vol. 1, pp. 92–105, 2015.

Chapter 2

Transport and optoelectronic properties in semiconductors

- 2.1 Introduction***
- 2.2 Band theory of solids***
- 2.3 Classification of semiconductors***
- 2.4 Transport properties in semiconductors***
- 2.5 Optical absorption in semiconductors***
- 2.6 Optical transmission in semiconductors***
- 2.7 Optical conductivity of semiconductors***
- 2.8 Photoconductivity of semiconductors***

2.1 Introduction

One of the principal utilities of semiconductors in a wide range of electronic devices (i.e., devices that employ the transport properties of carriers in the material) and optoelectronic devices (i.e., devices for the generation and detection of light) is related to their capability to form various junctions for different materials [1]. The physics of semiconductor devices is naturally dependent on the properties of semiconductor materials themselves [2]. Since transport phenomena play a fundamental role in solid-state devices, this chapter covers the fundamentals of conduction mechanism in semiconductors [3]. Optical measurements have many unique and attractive features for studying semiconductor properties [4]. Furthermore, the chapter includes some analytical expressions that are in good agreement with the most interesting experimental data of the semiconductors, and which can be used for numerical

calculations in the prepared semiconducting thin films.

2.2 Band theory of solids

During the past hundred years, three approaches have been developed to explain the electronic properties of materials. First one is the “continuum theory,” considered only the macroscopic properties. Later the interpretation of the metallic properties in terms of motion of free electrons (free electron model using Maxwell Boltzmann distribution) was developed by Lorentz and Drude. But the classical theory fails to explain heat capacity, magnetic susceptibility etc. The free electron model along with Pauli’s exclusion principle and Fermi – Dirac distribution function gives an insight into the heat capacity, thermal conductivity, electrical conductivity, magnetic susceptibility and electrodynamics of metals (Sommerfeld’s quantum free electron theory). According to this, the valence electrons of the constituent atoms are free to move in a field free space, throughout the volume of the specimen, except at the boundary of the solid. The potential energy due to the field of all nuclei and all other electrons is assumed to be constant every- where inside the metal except at the boundary of the solid. But this model, fails to explain the distinction between metals, insulators, semiconductors; the occurrence of positive values Hall coefficient; the relation of conduction electron in the metal to the valence electrons of free atom; the magneto transport property etc. In order to understand the difference between insulators, semiconductors and metal, F. Bloch replaced the Sommerfeld potential by a periodic potential of the lattice [5]. The electrons moving in a periodically varying potential field may possess energy within certain energy bands only. The energy spectrum

consists of a number of energy bands separated by forbidden regions. For example the permitted energy level of an atom of lithium, its molecule and its crystal are schematically represented in the figure 2.1 [6].

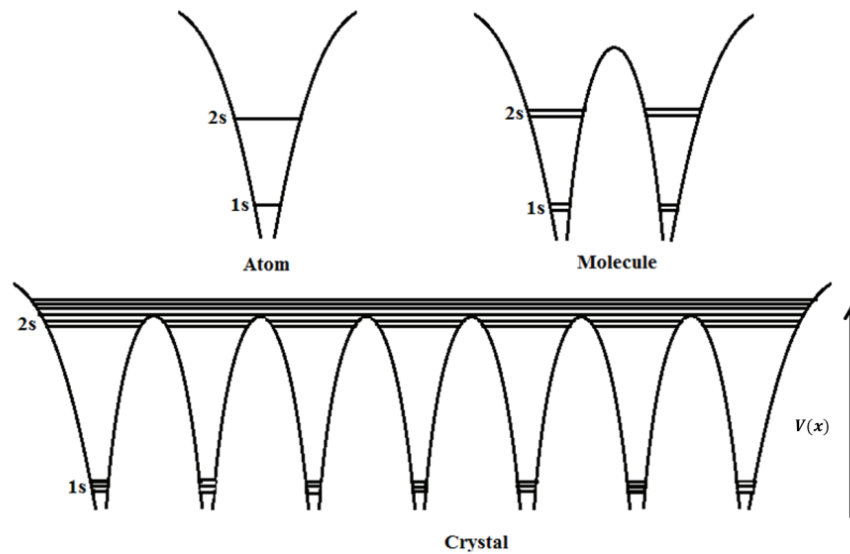


Fig.2.1 Periodic potential due to atomic core at the crystal lattice and the corresponding energy levels

The resulting electron band diagram is shown in figure 2.2. The discontinuities in the curve occur at $k = \pm n \frac{\pi}{a}$, where a is the lattice constant. These k values determine the boundaries of first, second etc. Brillouin zones. The presence of periodical potential also results in the electron mass (effective mass m^*). It is inversely proportional to the curvature of an electron band $E(k)$. Since the properties of the material are anisotropic, the effective mass may differ in each direction. Figure 2.2 shows the shape of energy band structure of a semiconductor as a function of wave vector (k) for a periodic

lattice of lattice constant a . The presence of these states does not mean that electrons are actually present in these states.

The Fermi Dirac distribution function $f(E)$ tells us the probability that an allowed level at energy E is occupied. When an allowed band is completely filled with electrons, the electrons being Fermions cannot carry any net current in a filled band since an electron can only move into an empty state.

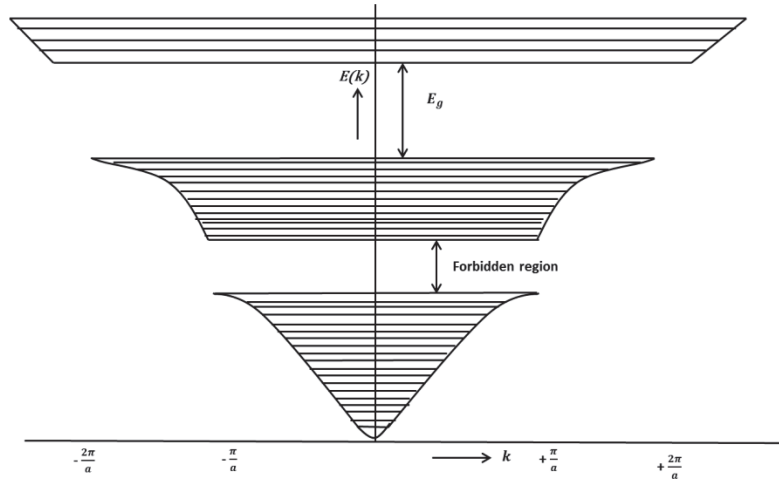


Fig. 2.2 Schematic representation of energy band diagram

The highest band normally filled with electrons at 0 K is called a valence band (VB) while the upper unfilled band above the VB is called conduction band (CB). Thus on the basis of energy bands the solids can be classified as follows [7][8].

- Insulator: - The material in which valence band is completely filled while the CB (separated by a band gap E_g) is completely empty is called insulator ($E_g > 3\text{eV}$).

- Metal: - The material in which an allowed band is only half or partially filled with electrons is called a metal.
- Semiconductor: - If the energy gap between the VB and CB is ≤ 3 eV, the material is called a semiconductor.

2.3 Classification of semiconductors

(a) Intrinsic semiconductors

In semiconductor materials (eg Si, Ge) each valence electron is shared by two atoms and are tightly bound to each other through covalent bonding. The semiconductor is said to be intrinsic if it is not contaminated with impurity atoms. At 0 K, all the bonds are strong, the semiconductor is said to be a perfect insulator. The situation is shown in figure 2.3.

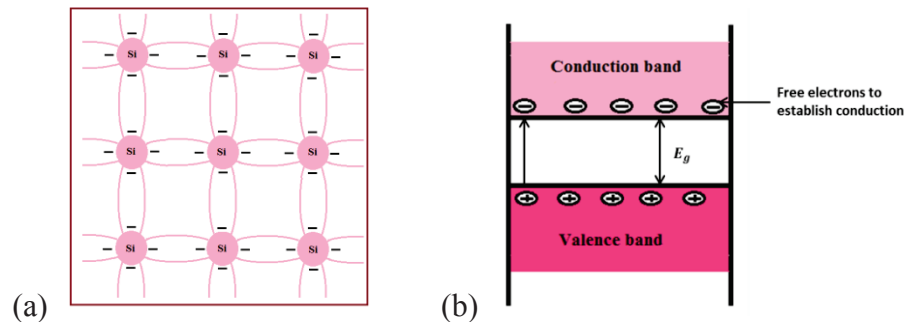


Fig.2.3 (a) Two-dimensional illustration of an intrinsic semiconductor at $T = 0$ K which behaves like insulator and (b) the basic energy band diagram at $T > 0$ K.

At practical operational conditions, for example room temperature, there are always some of the covalent bonds broken, resulting the liberation of the valence electrons from the bonds. We refer to these electrons as free electrons. The position of a missing electron in a bond, which can be regarded

as positively charged “vacancy or hole”. Figure 2.3(b) shows the energy-band diagram of an intrinsic semiconductor in which some electrons are shown in the conduction band. These have come from the valence band leaving equal number of holes there. Because breaking of a covalent bond leads to the formation of an electron-hole pair, in intrinsic semiconductors the concentration of electrons is equal to the concentration of holes.

(b) Extrinsic semiconductors

As the conductivity of an intrinsic semiconductor is low at room temperature, no important electronic devices can be developed, an improvement in conductivity can be achieved by doping with impurity atoms. The doped semiconductors are called extrinsic semiconductors [9]. There are two classes of impurities that are used. These are donor impurities and acceptor impurities. Typically one impurity atom is added per 10^8 semiconductor atoms. A semiconductor that is doped with a donor impurity is called an n-type semiconductor. One that is doped with an acceptor impurity is called a p-type semiconductor.

n -Type Semiconductor

An n-type semiconductor is produced by adding a donor impurity such as arsenic, antimony, or phosphorus to an intrinsic semiconductor. Each donor atom has five valence electrons. When a donor atom replaces an atom in the crystal lattice, only four valence electrons are shared with the surrounding atoms. The fifth valence electron becomes a free electron. The doping action can best be understood with the aid of the bonding model and is demonstrated in Figure 2.4. The number of free electrons donated by the donor atoms makes

the conductivity of the n-type semiconductor much greater than that of the intrinsic semiconductor. Above 0 K temperatures, hole-electron pairs are continually formed by the thermal agitation of the lattice.

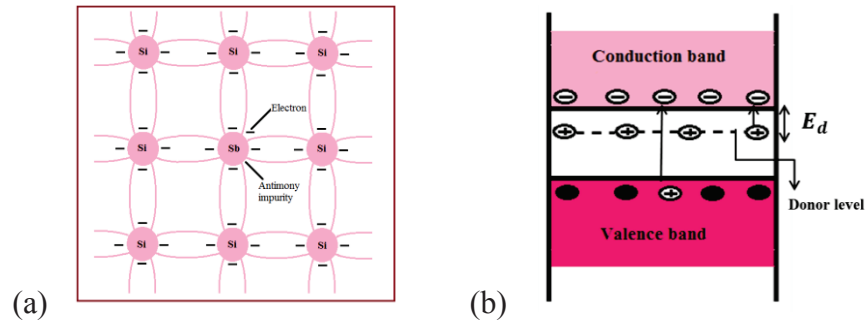


Fig.2.4 (a) Pentavalent donor atom (Sb) doped in tetravalent Si lattice giving n-type semiconductor and (b) energy bands of n-type semiconductor at $T > 0K$

Because the number of free electrons is far greater than the number of holes, the free electrons are the majority carriers. The semiconductor is called n-type because the majority carriers have a negative charge [10].

p -Type Semiconductor

A p-type semiconductor is produced by adding an acceptor impurity such as gallium, boron, or indium to an intrinsic semiconductor. Each acceptor atom has three valence electrons. When an acceptor atom replaces an atom in the crystal lattice, three valence electrons of acceptor are in covalent bonding and one bonding position is empty. This leaves a hole and the two dimensional illustration is shown in Fig. 2.5. The number of holes created by the acceptor atoms makes the conductivity of the p-type semiconductor much greater than that of the intrinsic semiconductor. Above 0 K temperatures, hole-electron

pairs are continually formed by the thermal agitation of the lattice. Because the number of holes is far greater than the number of electrons, the holes are the majority carriers. The semiconductor is called p-type because the majority carriers have a positive charge.

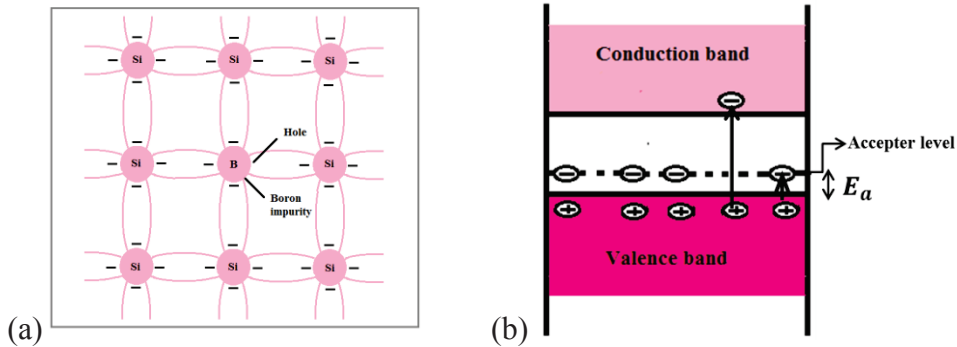


Fig.2.5 (a) Trivalent acceptor atom (B) doped in tetraivalent Si lattice giving p-type semiconductor and (b) energy bands of p-type semiconductor at $T > 0K$,

2.4 Transport properties in semiconductors

2.4.1 Electrical conductivity

In an intrinsic semiconductor, the hole concentration (p) must equal the electron concentration (n). Then

$$n = p = n_i. \quad (2.1)$$

where n_i is the intrinsic concentration. In the presence of an applied electric field E , the free electrons drift with a velocity

$$\vec{v}_e = -\mu_e \vec{E} \quad (2.2)$$

where μ_e is the electron mobility.

The holes drift with a velocity

$$\vec{v}_h = -\mu_h \vec{E} \quad (2.3)$$

where μ_h is the hole mobility. Although the free electrons and holes drift in opposite directions, the current densities add because the charge polarities are opposite.

The electron charge density is

$$\rho_e = -n_i q \quad (2.4)$$

and the hole charge density is

$$\rho_h = +n_i q, \quad (2.5)$$

The total current density can be written as

$$\vec{J} = \rho_e \vec{v}_e + \rho_h \vec{v}_h = n_i (\mu_e + \mu_h) q \vec{E} = \sigma \vec{E} \quad (2.6)$$

This equation defines the bulk conductivity σ of the intrinsic semiconductor. It is given by

$$\sigma = n_i (\mu_e + \mu_h) q \quad (2.7)$$

$$\mu_e > \mu_h \text{ since } m_e^* < m_h^* \quad (2.8)$$

where m_e^* and m_h^* are the effective masses of electron and hole respectively. From the temperature dependence of conductivity it is possible to determine the donor (or acceptor) levels in semiconductors using the relation

$$\sigma = \sigma_0 \exp\left(-\frac{E_a}{k_B T}\right) \quad (2.9)$$

where E_a is the activation energy as depicted in figures 2.4(b) and 2.5(b). As temperature increases, the carrier mobility in a semiconductor is determined by two mechanisms including impurity scattering and intrinsic phonon scattering [11].

Impurity scattering includes [12]

- Ionosied impurity scattering (μ_I) due to the Coulomb attraction or repulsion between the charge carriers and these ionized impurities.
- The neutral impurity scattering becomes considerable at sufficiently low temperature at which substantial number of impurity atoms become neutral

Phonon scattering (μ_{ph}) includes both acoustical and optical scattering and in practical semiconductors,

$$\frac{1}{\mu} = \frac{1}{\mu_I} + \frac{1}{\mu_{ph}} \quad (2.10)$$

In general, higher doping concentration results in increased scattering by the ionised impurities and there by decrease the mobilities. For ionised impurity scattering,

$$\mu_I \propto \frac{T^{3/2}}{N_I} \quad (2.11)$$

where N_I includes both ionized donor and acceptor impurities and T is the temperature.

For phonon scattering

$$\mu_{ph} \propto T^{-3/2} \quad (2.12)$$

where μ_{ph} is the phonon mobility.

2.4.2 Hall effect

In an isotropic material, the Hall coefficient is a measure of the induced voltage orthogonal to both an electric current and magnetic field. The van der Pauw (VDP) technique with four contacts is used to measure the Hall voltage.

Here a magnetic field of 0.55 T is used. A Hall effect measurement system can actually be used to determine the Hall voltage (V_H), carrier mobility (μ), carrier concentration (n), Hall coefficient (R_H), resistivity, magnetoresistance and the conductivity type [13].

The Fermi energy obtained is

$$E_F = \frac{h^2}{2m^*} \left(\frac{3n}{8\pi} \right)^{\frac{2}{3}} \quad (2.13)$$

where m^* is the effective mass and h is the Planck's constant

The relaxation time can be calculated as

$$\tau = \frac{\mu m^*}{e} \quad (2.14)$$

where e is the charge of electron.

The Fermi velocity and mean free path are

$$V_F = \left(\frac{2E_F}{m^*} \right)^{\frac{1}{2}} \quad \text{and} \quad l = \tau V_F \quad (2.15)$$

The density of states can be calculated as

$$N_V = 2 \left(\frac{2\pi m^* kT}{h^2} \right)^{\frac{3}{2}} \quad (2.16)$$

where k is the Boltzmann's constant and T is the temperature.

2.5 Optical absorption in semiconductors

Optical measurements are compatible, contactless, non-destructive technique for studying the optical properties of the materials. It involves the interaction between electromagnetic radiation and the material. The phenomenon studied to obtain the information on the optical properties of semiconductors is in general are absorption, transmission and photoconductivity. Optical absorption is described quantitatively through

absorption coefficient (α). If I_0 be the intensity of light incident on a material of thickness t , the intensity of the transmitted light is approximately

$$I = I_0 e^{-\alpha t} \quad (2.17)$$

The optical properties of semiconductors are integrally related to the particular nature of their electronic band structure. The most direct way of obtaining information about the energy gaps between band extrema is by measuring optical absorption over a wide range of wavelength. In the present work, absorption spectrum was recorded using JASCO V570 model UV-Vis-NIR spectrophotometer. The fundamental absorption edge is one of the most striking features of the absorption spectrum of a semiconductor. When a portion of energy equal to band gap of the material is absorbed, the semiconductor changes from being practically transparent to completely opaque, then the absorption coefficient changes by a factor of 10^4 or more. In semiconductors, a number of distinct optical properties take place independently.

(a) Fundamental Absorption Process

In fundamental absorption, an electron absorbs a photon (from the incident beam), and jumps from the valence band into the conduction band. The interband transitions near absorption edge are classified as direct or indirect [6][14].

Direct transition

In the transition process (photon absorption), the total energy and momentum of the electron-photon system must be conserved. Therefore

$$E_f = E_i + h\nu \quad \text{and} \quad k_f = k_i + q \quad (2.18)$$

where E_i and E_f are the initial and final energy of the electron in the valence and conduction bands, respectively, and k_i and k_f are the corresponding electron momenta. The vector q is the wave vector for the absorbed photon. Usually the wave vector of a photon in the optical region is negligibly small. The momentum condition given above therefore reduces to $k_f = k_i$. That is, the momentum of the electron alone is conserved.

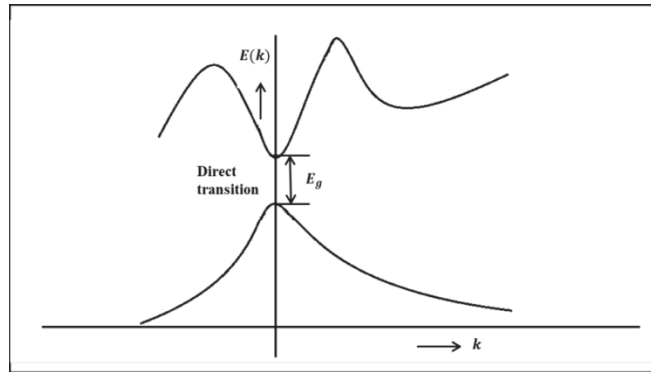


Fig.2.6 Direct transition from the valence band to the conduction band

The absorption coefficient of semiconductors, in high absorption region ($\alpha > 10^4 \text{ cm}^{-1}$) according to Tauc's relation for direct transmission is (figure 2.6) [15] [16]:

$$(\alpha h\nu) = A(h\nu - E_g)^m \quad (2.19)$$

where A is a constant E_g is the optical band gap and m is a constant. The value of $m = 1/2$ and $3/2$ represents the direct allowed and direct forbidden transition respectively. For direct band gap materials, transmission mostly occurs between two bands of the same k values as in figure. The direct allowed

transition can occur in all k values, while direct forbidden transition can occur only at $k = 0$. eg. GaAs, InP, InGaAs etc. are direct band gap materials.

Indirect transitions

There are also indirect-gap semiconductors, in which the bottom of the conduction band does not lie at the origin. Figure 2.7 shows the corresponding energy band diagram. In this case the electron cannot make a direct transition from the top of the valence band to the bottom of the conduction band because this would violate the momentum selection rule. Such a transition may take place, but as a two-step process. The electron absorbs both a photon and a phonon simultaneously. The photon supplies the needed energy, while the phonon supplies the required momentum.

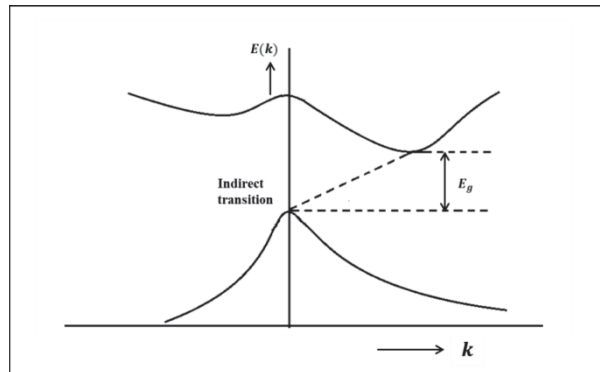


Fig. 2.7. Indirect transition from the valence band to the conduction band

Since phonons are involved in order to conserve momentum in indirect transitions, the above expression is modified to

$$(\alpha h\nu) = A(h\nu - E_g \pm E_p)^m \quad (2.20)$$

In these transitions, phonons (with energy E_p) are either by Beer's law are absorbed or emitted. The value of m is 2 and 3 for indirect allowed and forbidden transitions, respectively. For example Si, Ge, AlAs etc. are the indirect band gap materials. The band gap E_g is estimated by extrapolating the linear region of the plot $\ln(\alpha h\nu)^{1/m}$ versus $h\nu$.

(a) **Exciton absorption**

In fundamental absorption, it is assumed that the excited electron becomes a free particle in the conduction band, and similarly, the hole left in the valence band is also free. The electron and hole attract each other and may form a bound state, in which the two particles revolve around each other. That is they revolve around their center of mass. Such a state is referred as an exciton [17].

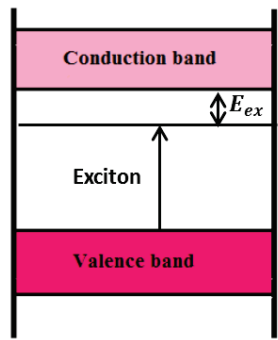


Fig.2.8 Exciton level and the associated absorption

The binding energy of the exciton is small and is nearly 0.01 eV, and hence the exciton level falls slightly below the edge of the conduction band, as indicated in figure 2.8. The exciton level is in the same neighborhood as the donor level. The energy of the photon involved in exciton absorption is given by

$$h\nu = E_g - E_{ex} \quad (2.21)$$

where E_{ex} is the Exciton binding energy. Absorption of an exciton introduces complications into the fundamental absorption spectrum, particularly near the edge and renders the determination of the energy gap in semiconductors more difficult. However, exciton absorption is important in discussion of optical properties of insulators in the ultraviolet region of the spectrum.

(b) Free-Carrier Absorption

Free carriers, both electrons and holes absorb radiation without becoming excited into the other band. In absorbing a photon, the electron (or hole) in this case makes a transition to another state in the same band. Such a process is usually referred to as an intraband transition. The free carrier absorption takes place when $h\nu < E_g$, and frequently this absorption dominates the spectrum below the fundamental edge. For $h\nu > E_g$, both type of absorption, fundamental and free-carrier absorption occur simultaneously.

(c) Absorption process involving impurities

The absorption processes involving impurities often take place in semiconductors. The type and degree of absorption depend on the type of impurity or impurities present, and on its concentration. Figure 2.9 shows the main classes of such processes. For low energy radiation a neutral donor absorbs a photon and the electron makes a transition to a higher level in the impurity itself or in the conduction band. The transition to higher impurity levels appears as sharp lines in the absorption spectrum.

Figure 2.9 (b) shows the transition from the valence band to a neutral acceptor, which is analogous to the donor-conduction band transition as in the case of figure 2.9 (a). Figure 2.9 (c) represents a process in which an electron

is excited from the valence band to an ionized donor, or from an ionized acceptor to the conduction band. Such processes lead to absorption, which is close to the fundamental absorption, and are seldom resolved from it. Figure 2.9 (d) illustrates an absorption process, involving transition from an ionized acceptor to an ionized donor. The energy of photon in this case is

$$h\nu = E_g - E_d - E_{im} \quad (2.22)$$

This leads to a discrete structure in the absorption curve, but this is often difficult to resolve because of its proximity to the fundamental edge.

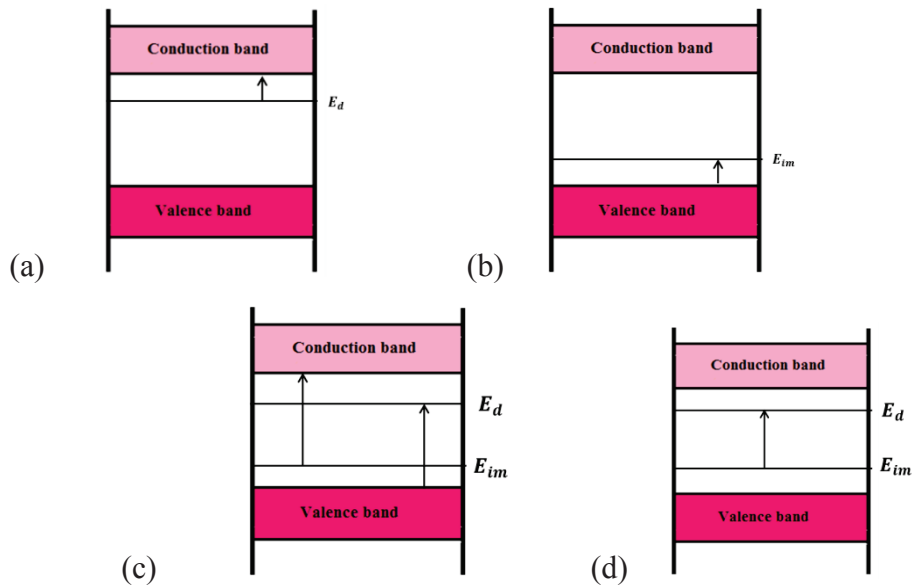


Fig. 2.9 Various absorption processes involving impurities

The impurities may also affect the absorption spectrum. For instance, an electron is often found to be trapped by an impurity. This may happen as follows: The impurity first traps an electron, now becoming a charged centre,

attracts a hole through the Coulomb force. Thus both an electron and a hole are trapped by the impurity.

2.6 Optical transmission in semiconductors

2.6.1 Determination of the optical constants and thickness of the film using Swanepoel method

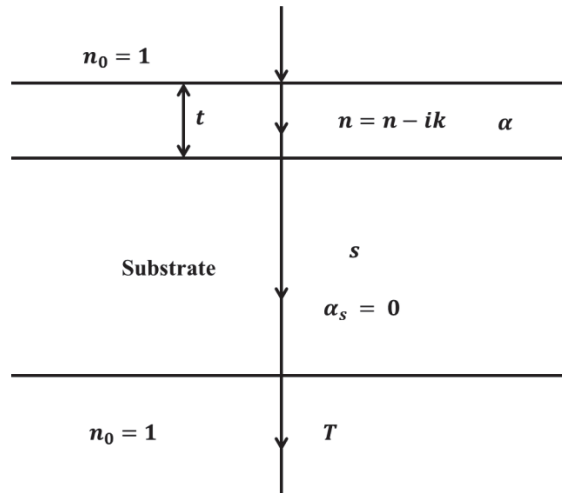


Fig. 2.10 The schematic representation for a thin film of thickness (t) on a transparent substrate

The ingenious exploitation of the optical phenomena such as reflection, absorption, transmission and polarization in the film has led to the development of various complex multilayer optical – device system for both industrial and laboratory applications. In addition, these optical properties has made it possible to determine the film thickness and the optical constants (extinction coefficient (k), absorption coefficient (α), refractive index (n)). A simple straight forward method has been developed by Swanepoel [18] for

calculating n and α using transmission spectra alone. The practical condition for a thin film of thickness (t) on a transparent substrate is shown in Figure 2.10.

The transparent substrate has a thickness of several orders of magnitude larger than t with index of refractions s and absorption coefficient $\alpha_s = 0$ and transmittance T_s . The index of refraction for air is taken to be $n_0 = 1$. If the thickness t is uniform, interference effects give rise to the spectrum, as shown in Figure 2.11 [18].

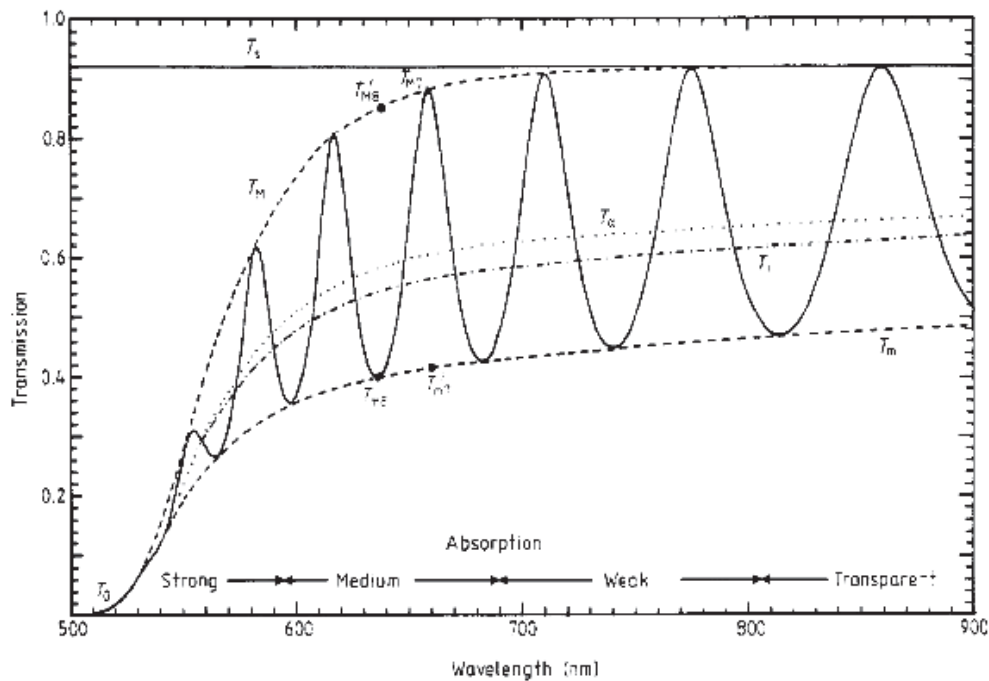


Fig. 2.11 Simulated transmission spectrum for a film on glass substrate

Considering the thick substrate alone in the absence of a film, the interference free transmission is given by the expression

$$T_s = \frac{(1-R)^2}{1-R^2} \quad (2.23)$$

where

$$R = \left(\frac{s-1}{s+1}\right)^2 \quad (2.24)$$

Then

$$T_s = \frac{2s}{s^2+1} \quad (2.25)$$

$$S = \frac{1}{T_s} + \left(\frac{1}{T_s^2} - 1\right)^{\frac{1}{2}} \quad (2.26)$$

The transmission T of the film for the case of figure 2.10 is a complex function and is given by

$$T = T(\lambda, s, n, t, \alpha) \quad (2.27)$$

Conveniently,

$$T = T(n, x) \quad (2.28)$$

where

$$x = e^{-\alpha t} \quad (2.29)$$

$$T = \frac{Ax}{B - Cx \cos \theta + Dx^2} \quad (2.30)$$

where

$$A = 16n^2s \quad (2.31a)$$

$$B = (n + 1^3)(n + s^2) \quad (2.31b)$$

$$C = 2(n^2 - 1)(n^2 - s^2) \quad (2.31c)$$

$$D = (n - 1)^3(n - s^2) \quad (2.31d)$$

$$Q = \frac{4\pi nt}{\lambda} \quad (2.31e)$$

Then the maxima and the minima of the interference figures from equation 2.30 is given by

$$T_M = \frac{Ax}{B-Cx+Dx^2} \quad (2.32)$$

$$T_m = \frac{Ax}{B+Cx+Dx^2} \quad (2.33)$$

For any λ , T_M has a corresponding T_m . The transmission spectra in figure 2.11 is divided into three regions and are described below

1. The transparent region

In this region $\alpha = 0$ and $x = 1$, then equations 2.32 and 2.33 becomes

$$T_M = \frac{2S}{S^2+1} \quad (2.34)$$

$$T_m = \frac{4n^2S}{n^4+n^2(S^2+1)+S^2} \quad (2.35)$$

From Equations 2.34 and 2.35, we have

$$n(\lambda) = [M + (M^2 - S^2)^{1/2}]^{1/2} \quad (2.36)$$

where

$$M = \frac{2S}{T_m} - \frac{S^2+1}{2} \quad (2.37)$$

From s and T_m , $n(\lambda)$ can be calculated and $k = \frac{\alpha\lambda}{4\pi} = 0$ since $\alpha = 0$

2. The region of weak and medium absorption

In this region $\alpha \neq 0$ and $x < 1$ and from equations 2.32 and 2.33, we give

$$\frac{1}{T_m} - \frac{1}{T_M} = \frac{2C}{A} \quad (2.38)$$

Substituting C and A from equation 2.31 into equation 2.38 leads to

$$n = [N + (N^2 - S^2)^{1/2}]^{1/2} \quad (2.39)$$

where

$$N = 2S \left[\frac{T_M - T_m}{T_M T_m} \right] + \frac{S^2 + 1}{2} \quad (2.40)$$

From equations 2.32 and 2.33, we give

$$\frac{2T_M T_m}{T_M + T_m} = \frac{Ax}{B + Dx^2} \quad (2.41)$$

Solving for x

$$x = \frac{F - [F^2 - (n^2 - 1)^3 (n^2 - S^4)]^{1/2}}{(n-1)^3 (n - S^2)} \quad (2.42)$$

where

$$F = \frac{8n^2 S}{T_i} \quad (2.43)$$

where

$$T_i = \frac{2T_M T_m}{T_M + T_m} \quad (2.45)$$

where T_i represents curve passing through the inflection point fringes as shown in figure 2.11. Knowing x , $x(\lambda)$ and $k(\lambda)$ can be determined

3. The region of strong absorption

In this region, the interference fringes will disappear. By using Cauchy's equation ($n = A^1 + \frac{B^1}{\lambda^2}$) where A^1 and B^1 are Cauchy's constants. n can be calculated in this region by extrapolating the values in the other regions. In strong absorption region, all the curves T_M , T_m and T_i converges into a single curve $T_0(\lambda)$ and

$$T_0(\lambda) = \frac{Ax}{B} \quad (2.46)$$

$$x = \frac{(n-1)^3 (n + S^2)}{16n^2 S} \quad (2.47)$$

Once x and thickness of the film are known, $\alpha(\lambda)$ can be calculated.

If n_1 and n_2 are the refractive indices calculated from two consecutive maxima or minima corresponds to two wavelengths of λ_1 and λ_2 then the thickness of the film t can be obtained from 2.38 [19]:

$$t = \frac{\lambda_1 \lambda_2}{2(\lambda_1 n_2 - \lambda_2 n_1)} \quad (2.48)$$

The values of $\alpha(\lambda)$ in strong absorption region can be used to determine the band gap of the material which in turn gives the variation of extinction coefficient with wavelength.

2.7 Optical conductivity of semiconductors

The optical conductivity is one of the powerful tools for studying the electronic states in the material [20]. If a system is subjected to an external electric field, then in general, a redistribution of charge occurs and currents are induced. For small enough fields, the induced polarization and currents are proportional to the induced fields. Experiments on optical transmission provide a way to determine the dielectric constants of the solids, which is related to the optical conductivity. Therefore optical conductivity is a measure of frequency response of the material when irradiated with light. If the refractive index and the extinction coefficient are known, the real (ϵ_r) and imaginary parts (ϵ_i) of dielectric constant of the film can also be estimated:

$$\epsilon_r = n^2 - k^2 \quad (2.49)$$

$$\epsilon_i = 2nk \quad (2.50)$$

The wavelength dependent optical conductivity (σ_{opt}) can be obtained as

$$\sigma_{opt} = \frac{\alpha n c}{4\pi} \quad (2.51)$$

where c is the velocity of light.

Using the single-oscillator model proposed by the Wemple-DiDomenico (WDD) [20][21] the dispersion of refractive index below the interband absorption edge can be analyzed as

$$n^2 - 1 = \frac{E_0 E_d}{E_0^2 - (h\nu)^2} \quad (2.52)$$

where E_0 is the single-oscillator energy and E_d is the dispersion energy. By plotting refractive index factor $(n^2 - 1)^{-1}$ versus $(h\nu)^2$ near the absorption edge and fitting the data to a straight line the values of WDD parameters E_0 and E_d can be obtained from the intercept E_0/E_d , and the slope $1/E_0 E_d$.

Urbach tail

The optical absorption coefficient near the fundamental absorption edge has an exponential dependency, which is given by the Urbach rule as [22]

$$\alpha = \alpha_0 \exp\left(\frac{E}{E_u}\right) \quad (2.53)$$

where E is the photon energy $h\nu$ and E_u is a constant or weakly dependent on temperature called Urbach energy which refers to the width of the exponential absorption edge. E_u can be estimated from the slope of the plot of $\ln(\alpha)$ versus photon energy graph. It corresponds to the optical transitions between the localised tail states adjacent to the valence band and extended states in the conduction band above the mobility edge.

2.8 Photoconductivity of semiconductors

The photocurrent measurements were done at room temperature by Keithley 2611A source meter, using silver paste as ohmic contact. An FSH

lamb (82 V, 300 W) was used as source of illumination. Under illumination electrons and holes are generated through the absorption of incident photon and are transported to the electrode at a constant bias voltage. The photocurrent at constant irradiance is studied. Photoconductivity is due to the absorption of photons (either by intrinsic or by extrinsic), leading to creation of free carriers in conduction and/or in the valence band.

The major transitions include [23]

- Band to band transitions
- Impurity level to band edge transitions
- Ionisation of donors
- Deep level (located in valence band) to conduction band transitions.

In semiconductors, the most widely used methods to determine localized state distributions are based on the analysis of non-exponential photocurrent transients. The transient photoconductivity measurements give the rise and decay of photocurrent under illumination. Under illumination, the photocurrent is found to increase with time since free carriers are generated through above mentioned transitions mechanism.

The rise of photocurrent with time is given by

$$I_{ph} = I_0 \left(1 - \exp\left(\frac{-t}{\tau}\right) \right) \quad (2.54)$$

where τ is the free carrier life time.

After the illumination is cut off, the current falls gradually with time. For exponential decay the differential life time is equal to the carrier life time. But for non-exponential decay the differential life time (τ_d) increases with

increasing time and τ_d at $t=0$ gives the carrier life time. In this case, from the slope of I_{ph} versus time plot, the differential life time can be calculated as [24]

$$\tau_d = - \left[\frac{1}{I_{ph}} \left(\frac{dI_{ph}}{dt} \right) \right]^{-1} \quad (2.55)$$

The non-exponential decay of photocurrent with time gives information about the presence of traps or recombination centres in the mobility gap of the materials. The traps originate from the defect states present in the materials which produces discrete energy levels in the band gap. The dispersion parameter (β) is calculated from the slope of $\ln(I_{ph})$ versus $\ln(t)$ plot. Using the value of β , the localized state distribution parameter E_l is also calculated by the relation

$$\beta = \frac{k_B T}{E_l} \quad (2.56)$$

where k_B is the Boltzmann constant and T is the ambient temperature. The value of E_l gives the trapping states or recombination centres present in the band gap. The recombination centres usually lie deeper within the band gap as opposed to the trap states which lie closer to the band gap edge.

References

- [1] B. G. Yacobi, *Semiconductor Materials-An Introduction to Basic Principles*. Kluwer Academic Publishers, 2004.
- [2] S. M. Sze and Kwok K. Ng, *Physics of Semiconductor Devices*, 3rd ed. A John Wiley & Sons, JNC., Publications, 2007.
- [3] C. Jacoboni, C. Canali, G. Otiaviani, and A. A. Quaranta, "A Review Of Some Charge Transport Properties Of Silicon," *Solid State Electron.*, vol. 20, pp. 77–89, 1977.

-
- [4] D. G. Seiler and Paul M. Amritharaj, *Handbook of Optics Volume II Devices Measurements and Properties*, 2nd ed. McGraw-Hill, 1994.
- [5] C. Kittel, *Introduction to solid state physics*, 7th ed. John Wiley & sons publishing, 2005.
- [6] J. P. Colinge and C. A. Colinge, *Physics of semiconductor devices*. Kluwe Academic Publishers, 2002.
- [7] J. Singh, *Semiconductor devices- Basic principles*. John Wiley & sons, Inc publishing, 2007.
- [8] G. Parker, *Introductory Semiconductor Device Physics*. Taylor and Francis, New York, 2004.
- [9] M. S. Tyagi, *Introduction to semiconductor materials and devices*. John Wiley & sons, Inc publishing, 2005.
- [10] H. T. Grahn, *Introduction to Semiconductor Physics*. World Scientific publishing, 1999.
- [11] Donald Neamen, *Semiconductor physics and devices-basic principles*. 3rd ed. Tata McGraw-Hill Publishing, 2002.
- [12] D. Chattopadhyay and H. J. Queisser, "Electron scattering by ionized impurities in semiconductors," vol. 53, pp. 745–766, 1981.
- [13] T. Matsumura and Y. Sato, "A Theoretical Study on Van Der Pauw Measurement Values of Inhomogeneous Compound Semiconductor Thin Films," *J. Mod. Phys.*, vol. 1, pp. 340–347, 2010.
- [14] M. S. Dresselhaus, *Solid State Physics Part II-Optical Properties of Solids*. MIT Solid state physics course, 2011, 2001.

- [15] J. Tauc, "Optical properties and electronic structure of amorphous Ge and Si," *MRS Bull.*, vol. 3, pp. 37–46, 1968.
- [16] J. Tauc, "States in the gap," *J. non-Cryst. solids*, vol. 10, pp. 569–585, 1972.
- [17] R. A. Smith, *Semiconductors*, 2nd ed. Academic publishers, 1978.
- [18] R. Swanepoel, "Determination of the thickness and optical constants of amorphous silicon," *J. Phys. E.*, vol. 16, pp. 1214–1222, 1983.
- [19] D. Dorranean, L. Dejam, and G. Mosayebian, "Optical characterization of Cu₃N thin film with Swanepoel method," *J. Theor. Appl. Phys.*, vol. 6 :13, pp. 1–9, 2012.
- [20] E. R. Shaaban, I. S. Yahia, and E. G. El-Metwally, "Validity of swanepoel's method for calculating the optical constants of thick films," *Acta Phys. Pol. A*, vol. 121, no. 3, pp. 628–635, 2012.
- [21] S. H. Wemple and M. DiDomenico, "Behavior of the Electronic Dielectric Constant in Covalent and Ionic Materials," *Phys. Rev. B*, vol. 3, pp. 1338–1351, 1971.
- [22] S. John, C. Soukoulis, M. H. Cohen, and E. N. Economou, "Theory of electron band tails and the urbach optical-absorption edge," *Phys. Rev. Lett.*, vol. 57, no. 14, pp. 1777–1780, 1986.
- [23] N. V. Joshi, *Photoconductivity: Art, Science and Technology*. Marcel Dekker, Inc., 1990.
- [24] W. Fuhs and J. Stuke, "Hopping Recombination in Trigonal Selenium Single Crystals," *Phys. stat.sol.*, vol. 27, pp. 171–184, 1968.

Chapter 3

Experimental techniques and characterization tools

- 3.1 *Introduction : Physical evaporation technique, evaporation theory and surface mechanism during film growth*
- 3.2 *Gunter's three temperature method*
- 3.3 *Details of the reactive evaporation technique used for present investigation*
- 3.4 *Characterisation tools*
- 3.5 *Aim of the present work*

3.1 Introduction

The majority of the material processes in semiconductor device technology are crucially dependent on film deposition technology because of the following reasons [1].

- Micro-electronic solid state devices are all based on material structures in thin film form.
- The better understanding of the physics and chemistry of films, surfaces etc are made possible by the remarkable advances in analytical instrumentation during the past years and it leads to expanded applications and new designs of the devices.

The detailed investigation of thin film properties such as structural, optical and electrical etc. becomes an important part of research and technological device applications. Different techniques have been employed for depositing thin films. The aim of this chapter is to provide a concise reference and description of the theory of evaporation and the surface mechanism during film

growth. The discussions of the theory of the reactive evaporation technique, its advantages, disadvantages etc are also included. Furthermore, the chapter contains a brief discussion of the experimental techniques used for the determination of the transport quantities, structural parameters and optical quantities.

The properties of thin films are extremely sensitive to the method of preparation, several techniques have been developed for the deposition of the thin films of the metals, alloys, ceramic, polymer and superconductors on a variety of the substrate materials [2]. Thin film deposition techniques are broadly classified into two headings [3]:

- Chemical deposition technique
- Physical vapour deposition technique

Chemical deposition technique exploits the creation of solid materials directly from chemical reactions in gas and/or liquid compositions or with the substrate material. The solid material is usually not the only product formed by the reaction, byproducts can include gases, liquids and even other solids. Chemical deposition falls into two categories namely gas phase deposition and liquid phase deposition.

The term physical vapor deposition (PVD) is used to denote those vacuum deposition processes such as physical evaporation and sputtering where the coating material is passed into a vapor transport phase by physical mechanism such as evaporation, sublimation, or ion bombardment [4]. Physical evaporation includes the vaporization of solid material on heating and condensation of these vapours on the substrate. Sputtering includes the ejection

of atoms from the surface of the target material by bombardment with energetic particles.

3.1.1 Physical evaporation technique

The process of physical evaporation, which is traditionally known as vacuum deposition, used as a simplest technique for preparing thin film. The thermal evaporation process consists of evaporating and condensing processes in a vacuum ($\approx 1 \times 10^{-5}$ mbar) chamber [5]. Firstly, source materials are evaporated by the heated source, which is maintaining a few centimeter distances from a substrate. Then, evaporated particles are condensed on the substrate. This process can use two types of sources that are resistive and electron beam source. Resistive thermal evaporation is one of the most commonly used metal deposition techniques in which a high current is passed through the source material (source material is usually in the shape of a basket, boat or crucible usually manufactured of refractory metals such as tungsten, molybdenum and tantalum with or without ceramic coating) in vacuum [6]. The properly evacuated chamber provides the following advantages.

- By reducing the ambient pressure in the chamber, the boiling point of the evaporant can be reduced.
- Formation of oxides is reduced considerably
- The incorporation of impurity atoms within in the growing film can be reduced considerably.
- It ensures straight-line propagation of particles from source to substrate.

3.1.2 Evaporation Theory – General Considerations

Different stages of film formation by vacuum evaporation process include mainly the following four sequential steps

1. Transformation of material from solid or liquid into gaseous state
2. Transfer of these particles from source to substrate
3. Deposition of these particles over the substrate surface
4. Rearrangement over the substrate surface

During the transfer of vapour particles, they collide with ambient gas molecules, a fraction of vapour atoms $e^{-\frac{d}{l}}$ will be scattered over a distance d . Here l is the mean free path (mfp). Mean free path (l) is the average distance travelled by a particle between two successive collisions at a given temperature as:

$$l = 5 \times \frac{10^{-3}}{P} \quad (3.1)$$

where P is the vapour pressure in torr at a temperature of 300 K. At a pressure of 10^{-3} and 10^{-5} torr, l is about 5 and 500 cm respectively. Thus a high vacuum of about 10^{-5} torr should be ensured in the chamber for the straight line propagation. The particle concentration at a given pressure P and temperature T can be calculated as Loschmidt's number:

$$n = \frac{9.656 \times 10^{18} P}{T} \text{ cm}^{-3} \quad (3.2)$$

That is even at a pressure of 10^{-8} torr and $T = 300$ K a high density of particles of about 3.2×10^8 molecules cm^{-3} are present in the chamber. These stray particles can cause the scattering of the material particles evaporated

from the source [7][8]. Normally the number of particles evaporated over unit area in unit time from a source can be determined as:

$$N_e = \frac{3.513 \times 10^{22} P_e}{\sqrt{M_e T}} \quad (3.3)$$

where P_e is vapour pressure of the evaporant material and M_e is the molecular weight of the evaporant material. This is known as Hertz-Knudsen equation. In this $(1 - e^{-\frac{d}{l}})$ fraction of particles are impinged on the substrate surface and the number of particles deposited on the substrate depends on the sticking coefficient S_c of the vapours. Then the number of particles impinged per unit area per unit time on the substrate $(\frac{dN_m}{A_r dt})$ is given by the expression.

$$\frac{dN_m}{A_r dt} = \frac{N_a \rho_m d'}{M_m} \quad (3.4)$$

where N_a = Avagadro number in mol^{-1}

ρ_m = density of the evaporant material in gcm^{-3}

M_m = molar mass of the material in gmol^{-1}

d' = deposition rate in cms^{-1}

A_r = Area of the substrate surface in cm^2

Moreover the rate of deposition of the vapour on a substrate depends on the source geometry, its position relative to the substrate and the condensation coefficient. According to Knudsen cosine law, for the ideal case of deposition from a clean, uniformly emitting point source onto a plane receiver, the rate of deposition varies as $\frac{\cos \theta}{r^2}$, where r is the radial distance of the receiver from the source and θ is the angle between the radial vector and the normal to the receiver distribution [6].

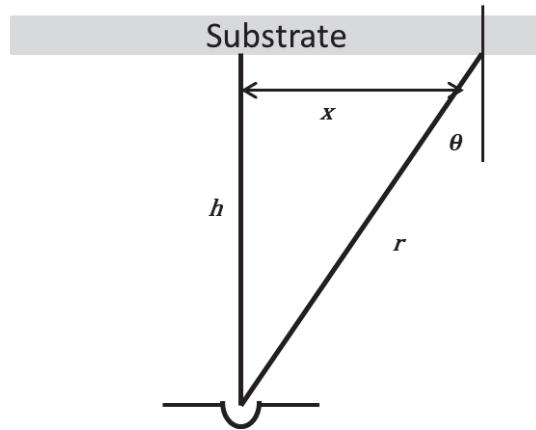


Fig. 3.1 Variation of film thickness along the length of the substrate

If t_0 and t are the thicknesses of the deposits at the receiver vertically below the source at a distance h , and at a horizontal distance x from the vertical line, respectively, the gradient of deposition (figure 3.1) is given by

$$t = \frac{t_0}{\left[1 + \left(\frac{x}{h}\right)^2\right]^{3/2}} \quad (3.5)$$

In the present study, the sample is supported by a dimple and in that case

$$t \sim \frac{3m}{2\pi r^2 \rho_m} \quad (3.6)$$

where r is the distance of the separation of source and the substrate. m and ρ_m be the mass and density of the material evaporated respectively from the source.

3.1.3 Surface mechanism during the film growth

Tailoring of various optoelectronic properties of thin films depend very strongly on nucleation and growth processes. Therefore the nucleation and growth process involved during thin formation is of great interest in various applications such as hetero-junction lasers, multiple quantum well structures,

optical coatings or wear – resistant protective layers [9]. The grain structures and the deposit morphologies interestingly determine many of the properties of thin film. For example columnar structures which interestingly develop in amorphous as well as polycrystalline films have a great effect on magnetic, optical, electrical and mechanical properties. These surface mechanisms responsible for the structure of the films can be divided into four sequential stages.

- Nucleation
- Growth of nuclei
- Coalescence
- Filling of channel

Nucleation and growth processes are responsible for the structure of thin films grown on surfaces [10]. During the earlier stages of film formation, a sufficient number of vapor atoms or molecules condense and establish a permanent residence on the substrate [11]. Soon after exposure of the substrate to the incident vapor, a uniform distribution of small but highly mobile clusters or islands are formed. In this stage, the prior nuclei incorporate impinging atoms and subcritical clusters and grow in size while the island density rapidly saturates. The next stage involves merging of the islands by a coalescence phenomenon. Coalescence continues until more or less connected network with unfilled channels in between develops. With further deposition, the channels fill in and shrink, leaving isolated voids behind. Finally, even the voids fill in completely, and the film is said to be continuous [11].

The impinged atoms can either be evaporated or reflected on the surface and the process depends on impingement rate and sticking coefficient (S_c). S_c describes the probability for the incoming atoms to lose its kinetic energy via energy transfer to the atoms of solid and to become trapped in a bound state at the surface. This bound state can be physisorbed or chemisorbed state. In physically adsorbed state, the binding energy is typically below 0.5 eV and the adsorbed atoms interact through Van-der-Waals force. In the chemisorbed state, the binding energy is above 0.5 eV and the adsorbed atoms form an ionic or covalent bond. Thus the physisorbed state can be represented as a precursor state for the chemisorbed state [12].

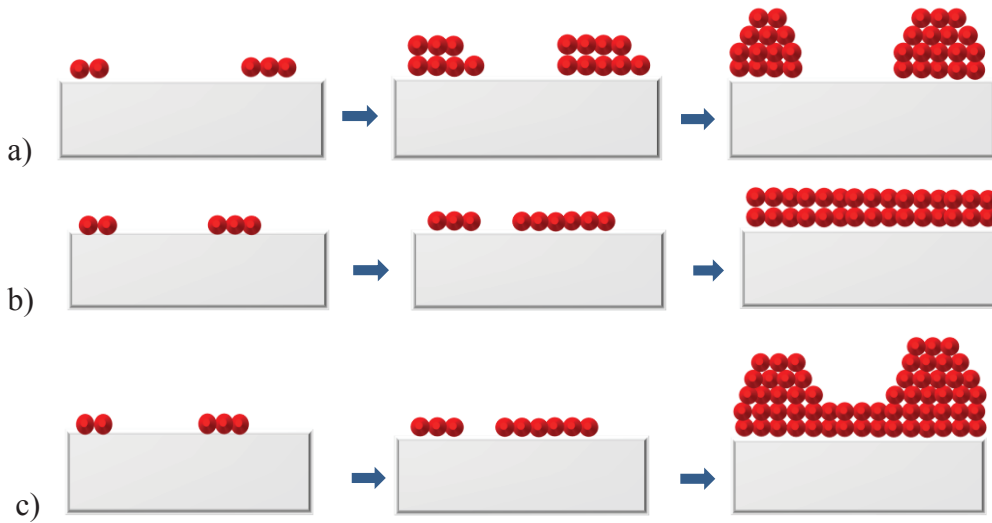


Fig. 3.2 Schematic illustrations of the basic growth modes including (a) Volmer-Weber (island), (b) Frank-Van der Merwe (layer-by-layer), and (c) Stranski-Krastanov growth (island-by-layer).

Generally, there are three different modes of thin film formation on the surface which are schematically illustrated in figure 3.2. According to Volmer-Weber model (Island growth model) firstly small clusters of nuclei are nucleated directly on the substrate surface and then grow into islands of the condensed phase. This happens when the atoms of the deposits are strongly bound to each other than the substrate.

The Frank Van Merwe growth mechanism is opposite to island growth. If the atoms are strongly bound to substrate than to each other, firstly a monolayer is formed on the surface and then this monolayer is covered with somewhat less tightly bound second layer. The Stranski-Krastanov's mode is a mixed mode of the above mentioned modes. The general feature of this mode is initially a monolayer or few monolayers are formed and then changes into island growth. This mode occurs when strain the intermediate layer accumulates in the growing film, it is released and then favors the island growth. Island growth is typically important for metals and semiconductors grown on insulators.

3.2 Gunter's three temperature method

As the name indicates, for the formation of the stoichiometric binary compound, generally three temperatures, that is substrate temperature and two evaporator temperatures are to be fixed and hence the process is called "three temperature method". Continuous condensation of a given vapour on a substrate is possible only if critical super saturation is exceeded, that is, continuous condensation of a particular vapour at a given deposition rate is possible only if the temperature of the substrate drops below a critical

temperature. When multicomponent alloys or compounds are thermally evaporated, the components may evaporate at different rates because of their different vapour pressures, their different tendencies to react with the support material and possible thermal decomposition of parent material. These factors will obviously produce non-stoichiometric films. A satisfactory method of preparing alloys and compounds with precisely controlled composition is to evaporate each component from a separate source with reaction and homogeneity brought about at the substrate at an elevated temperature. Such a method is referred to a “two source” or “three temperature” or “Gunther technique”. Here three heating arrangements are used in this method, one is for giving temperature to the substrates, and other two are for the two sources—molybdenum boat and glass crucible.

Furthermore, if different vapours are present in the vapour phase, they may interact with each other and thus influence considerably, the above mentioned critical values of supersaturation or super cooling. The adsorption or condensation of gases only loosely attracted on solid surfaces can be greatly accelerated by other components. These conditions process may be drastically changed in the presence of several vapours, which may interact and form stable compound [13].

The sticking coefficient (S_c) of a given vapour on a given substrate temperature, or the condensation flux N_k exceeds zero only if the ratio p/p_e of the actual vapour pressure p and the equilibrium pressure p_e exceeds a critical value q_c

$$N_K > 0 \text{ if } (P/p_e) > q_c \quad (3.7)$$

where

$$p_e = \text{const.} \exp\left(\frac{\Delta G_v}{kT}\right) \quad (3.8)$$

and ΔG_v is the vapourization energy. The pressure in the above expression is also related to the substrate temperature T . Let N_+ and N_e be the number of incident and emitted particles per unit time and area. Then from thermodynamic theory, one obtains

$$N_e = \alpha_c p_e / (2\pi m k T)^{1/2} \quad (3.9)$$

where α_c is the condensation coefficient and the condition (1) may be rewritten as

$$N_K > 0 \text{ if } \left(\frac{N_+}{N_e}\right) > \left(\frac{N_+}{N_e}\right)_c \quad (3.10)$$

At a given substrate temperature T , the equilibrium value N_e is given by

$$N_e = C \exp\left(\frac{\Delta G_v / kT}{2\pi m k T^{1/2}}\right) \quad (3.11)$$

The condition for progressive condensation at a given substrate temperature involves exceeding a critical incident flux, i.e.

$$N_K = 0 \text{ if } N_+ \leq N_{+c}(T) \quad (3.12)$$

$$N_K > 0 \text{ if } N_+ > N_{+c}(T) \quad (3.13)$$

where N_{+c} is the critical value of incident flux. If the flux exceeds N_{+c} , the condensation flux rises rapidly and approaches its maximum value given by

$$N_{K \max} = \alpha(N_+ - N_e) \quad (3.14)$$

This behaviour is shown schematically in fig 3.3.

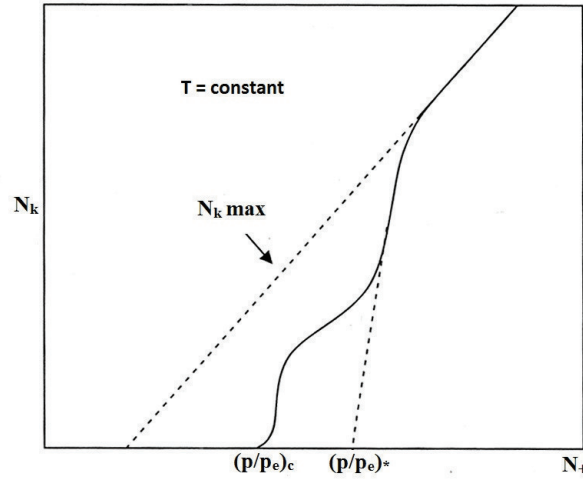


Fig. 3.3 Variation of condensation flux N_k with flux N_+ of incident particles.

The actual slope of the function $N_k = f(N_+)$ depends on the mechanism of nucleation, and can vary from one case to another. (p/p_e) corresponds to the beginning of nucleation due to surface diffusion. During deposition and condensation of the first monolayer of the incident vapour on an unlike substrate, the interfacial forces, and consequently the critical values q_c and the T_c/T_e may change, reaching constant values when the deposited layer itself act as substrate. Since we are concerned with continuous deposition, where the condensation of the first monolayer is only a negligible part of the process as a whole, all further considerations will be related to critical values for super saturation or sub cooling which are related to like substrates.

3.2.1 Condensation Phenomena Occurring With Binary Vapours

Consider the vapour phase consists of two components A and B, both being incident on the substrate under consideration. As in the cases of high vacuum deposition, vapour density may be low enough to neglect collisions between particles of the components A and B in the vapour phase. Interactions can take place between such particles within the adsorbed stage on the substrate surface. These interactions, due to the strong attractive forces between particles A and B lead to the formation of molecules,



Of a stable compound AB, A rough estimate of the interaction probability on the surface gives a density

$$n_{AB} = \text{const.} \times n_A n_B \bar{D} \quad (3.16)$$

of adsorbed molecules AB, which is proportional to the product $n_A n_B$ of adsorbed particles A, B and a mean diffusion coefficient D.

The density n_i of the adsorbed particles is given by the equation,

$$n_i = \left(\frac{N_{+i}}{\omega} \right) \exp \left(\frac{\Delta G_a}{kT} \right), \quad i = A, B \quad (3.17)$$

where ΔG_a is the interfacial energy with the substrate and ω is the transmission frequency. Since n_i is proportional to the actual vapour pressure p , or the incident flux, N_+ of the particular vapour, the density n_{AB} should also be proportional to the product of incident fluxes ($N_{+A} N_{+B}$) or vapour pressures ($p_A p_B$). Let the equilibrium pressures of the components be p_{eA} and p_{eB} and let p_{eAB} be that of compound. p_{eAB} usually corresponds to the dissociation

pressure of the compound, and is equivalent to the pressure $p_e \left(\frac{i}{AB} \right)$ of the more volatile component i in equilibrium with the compound. The critical value of one component i in the presence of other component j should vary as:

$$N_{+ci}(j) \ll N_{+ci}; p_e \left(\frac{i}{AB} \right) \ll p_{ei} \quad (3.18)$$

$$T_{ci}(j) > T_{ci} \quad (3.19)$$

with respect to the particular fluxes N_{+} . This behaviour is shown in figure 3.4.

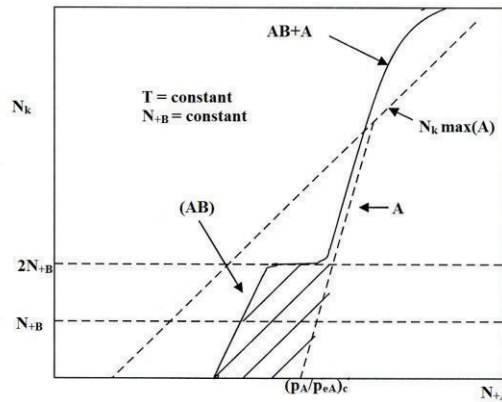


Figure 3.4 Condensation flux N_k with two incident components A, B

At a given temperature T and for incident fluxes $N_{+B} < N_{+cB}$, nocondensation of any kind is possible while the incident rate N_{+A} and the related adsorption density n_A are also very low. However, at a critical value $N_{+cA}(B)$ sufficient molecules AB are formed on the substrate, nucleation and progressive condensation of the compound AB starts and rapidly goes to the maximum flux.

The critical value $N_{+CA}(B)$ itself depends on the incident flux of compound B . The maximum value is reached when each impinging particle B reacts with one of the simultaneously impinging particles A . With further increase of flux N_{+A} , no increase of the condensation flux N_K is possible until, with $N_{+A} > N_{+CA}$, condensation of non-interacting particles A takes place thereby further increasing considerably the total condensation flux to the final value $(N_{+B} + N_{+A} - N_e)$. In terms of substrate temperature this is shown in figure 3.5.

In contrast to the conditions for singly components, the critical values T_{CAB} , N_{+CAB} of the compound can be different from the equilibrium values. As in figures 3.4 and 3.5, not only the condensation flux but also composition of the condensed layers are affected by the given incident fluxes and temperatures. These relations are shown in figure 3.6. It will be seen that well-defined areas with layers of different composition can exist as functions of the incident fluxes. There exists one region in particular where only pure compound layers of the composition AB are obtained, while the unsaturated components are reemitted in the vapour phase. This special region should occur in all cases, where the condition

$$p_e \left(\frac{i}{AB} \right) < p_{ei}; (i = A, B) \quad (3.20)$$

is satisfied that is a significant increase in adsorption energy due to the relation $A+B \rightarrow AB$ is necessary. The area of the region is dependent on the substrate temperature T and increase with T , but this is possible only within a limited T .

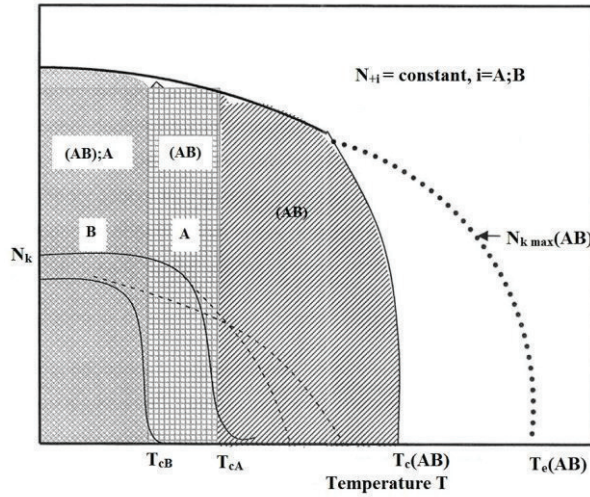


Fig. 3.5 Condensation flux as a function of temperature

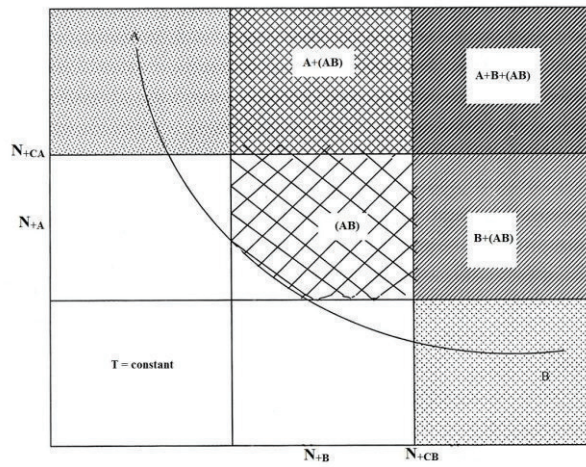


Fig. 3.6 Condensation diagram for two incident components A and B

Thus by selecting a method based on above assumption, the deposition of exact stoichiometric compound layers by simultaneous evaporation of the single components should be possible.

3.2.2 Advantages and limitations of reactive evaporation technique

The advantages of this technique includes

- The need to synthesize the compound from the elements prior to deposition which is a tedious and sometimes expensive metallurgical process is eliminated.
- High temperatures ($> 2000\text{ }^{\circ}\text{C}$) are frequently needed to evaporate high melting point carbides, nitrides and oxides as such and if resistive heating is used, the film will be contaminated as a result of evaporation of the source itself. This is avoided in reactive evaporation.
- The decomposition of the compound upon heating in vacuum and the consequent lack of stoichiometry in the films are avoided.
- High rates of deposition of the compounds are possible.
- Amorphous films can be prepared by this method, since the lowest substrate temperature possible is dictated by the condensation temperature of the more volatile component (usually low for O_2 , S_2 , and Se_2).
- Dopants can be evaporated simultaneously and a uniform dispersal of the dopant can be easily achieved.

This technique, which has been successfully used for many technologically important compounds, has the following limitations.

- The use of large volatile flux entails the loss of the volatile element.
- When high deposition rates are required, the use of large amounts of volatile flux leads to high volatile partial pressure ($10^{-4} - 10^{-2}$ torr), which reduces the mean free path and also scatters the nonvolatile

beam away from the substrate surface. Again the high pressure in the vacuum system reduces the evaporation rate of the nonvolatile component.

- Because of high volatile elemental pressure, some unreacted volatile element is likely to be entrapped in the growing film, changing the film properties, especially at low substrate temperatures.

3.3 Experimental details of the reactive evaporation technique used in present investigation

The method used in preparing the binary compound thin films in the present investigations is two source co-evaporation or reactive evaporation technique. For the formation of the stoichiometric binary compound, generally three temperatures, that is substrate temperature and two evaporator temperatures are to be fixed and hence the process is also called “Gunther’s three temperature method”.

3.3.1 Vacuum coating unit

The films were prepared using a conventional 12” bell jar vacuum coating unit manufactured by Indian High Vacuum Pumps with co-evaporation facility. It consists of facilities such as ion bombardment, substrate heating etc. The schematic representation of the vacuum system fitted with a 12" glass bell jar, used for the preparation of the films in the present study is shown in figure 3.7 [14]. The working chamber was evacuated initially to a pressure of 10^{-2} torr using the rotary pump. A 4” oil diffusion pump backed by a rotary pump attained the pressure of 10^{-5} torr. Two pirani gauge heads and a penning gauge head are provided to independently monitor the fore and high vacuum

respectively [15]. A water cooled baffle is normally used with diffusion pump to keep oil out of the pump.

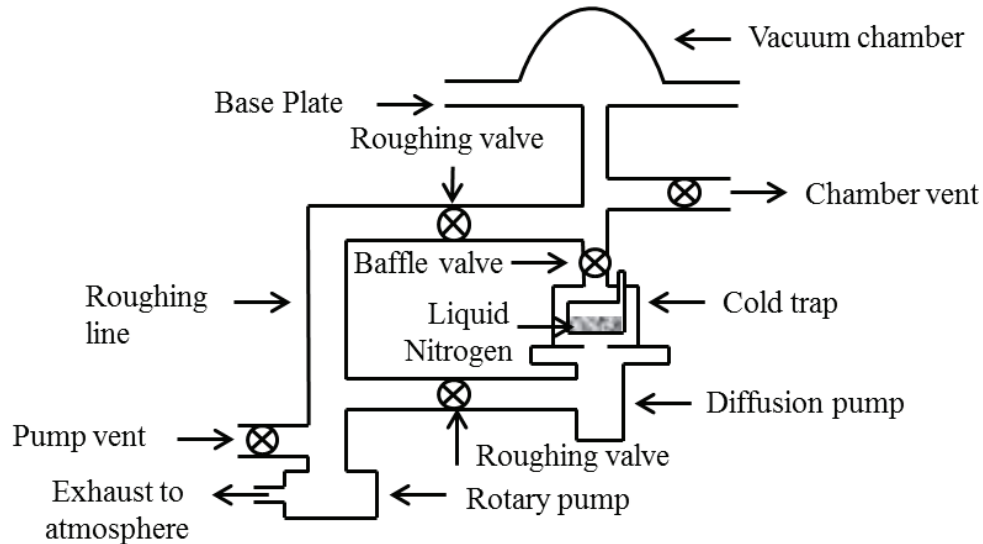


Fig. 3.7 Schematic diagram of the vacuum system

A molybdenum boat and a glass crucible kept in a molybdenum basket are used for the evaporation of the elements and they are connected between the electrodes at fixed, pre-determined distance from the substrates. High current sources, capable of supplying 200 A are used to provide current to the evaporators. The nature and finish of the substrates are extremely important because they greatly influence the properties of the film deposited on to them. The adhesion of adatoms to the substrate surface mainly depends on the cleanliness of the substrate. Also the cleanliness of the substrate determines the composition and the quality of films [2].

The substrate cleaning prior to deposition consists of the following sequential steps

- The substrates are initially cleaned by applying an industrial detergent.
- After this they are thoroughly washed in running water followed by distilled water.
- The slides are then arranged in specially made holder immersed in double distilled water and are subjected to cleaning by ultrasonic agitation for 15 minutes.
- Finally the substrates are dried with a hot air blower and are loaded into the vacuum chamber.

Cleaning the evaporators before loading into the vacuum chamber is also equally important to avoid the contamination of the film. It includes the following steps

- The molybdenum boat and basket are initially dipped in nitric acid
- Then they are thoroughly cleaned in running water followed by distilled water.
- Then they are dried with hot air blower and are connected between the electrodes in the vacuum chamber
- The glass crucible cleaned with acetone is placed in the basket.

3.3.2 Deposition of thin films

There are several steps to forming thin films on the substrate. The schematic representation of a vacuum system such as the one used for the preparation of the films in this study is given in figure 3.8. Firstly, load required amount of the evaporation materials into the source materials and also put substrates in the chamber. Then the system is pumped to a pressure of $\sim 10^{-7}$

⁵ torr. Ultrasonically cleaned flat glass slides are used as the substrates. A fine wire chromel-alumel thermocouple is used to measure the temperature of the substrate. When the substrates have attained the required temperature, it is maintained at that temperature with an accuracy of ± 5 K. Then high purity selenium (99.999%) from the glass crucible kept in molybdenum basket is evaporated. When sufficient flux of selenium is obtained, high purity metal from molybdenum boat is evaporated.

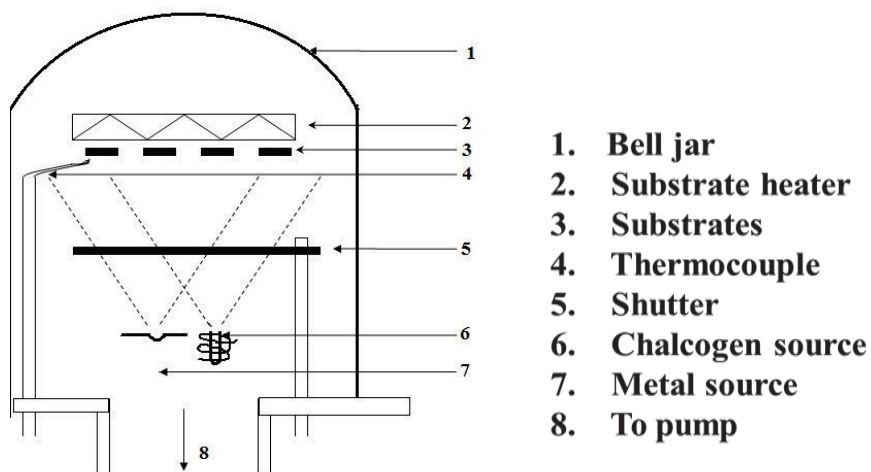


Fig. 3.8 Schematic diagram of the experimental set up for reactive evaporation.

The current through the sources are independently adjusted to a pre-determined value to obtain the required incident flux. Then the shutter is opened so that the vapours of individual elements reach the substrate and react to form the compound film on the substrates kept at an elevated temperature. Care is taken to keep the substrate and source temperatures stable throughout the time of deposition. When the deposition is completed, shutter is closed.

Then high current is passed through the boat to clean it and the source currents were adjusted to zero. The substrate temperature was slowly reduced to room temperature.

3.4 Characterisation tools

3.4.1 X-Ray Diffraction

X-Ray diffraction is versatile, non-destructive technique used for the determination of structure and for analyzing structural properties such as particle size, phase composition, strain, crystal orientation and defects. In a diffraction experiment, the wavelength of the incident wave is of the same order of magnitude as the spacing between atoms. Three types of waves (X-ray, Neutrons and electrons) have proved to be useful for the study of crystalline structures by diffraction experiments [16]. In XRD, pioneered by Von Law Braggs, when the incident monochromatic beam of X-ray strikes an atom the tightly bound electrons are set into oscillation and radiate x-rays of same frequency as the incoming radiation (Figure 3.9). However, the atoms in a crystal are arranged in a periodic manner, these currently scattered radiations from the atoms undergo constructive interference in certain direction and cancellation in another direction. Hence, diffraction is essentially reinforced coherent scattering and is nothing but Bragg's Law:

$$2d \sin \theta = n\lambda \quad (3.21)$$

when d is spacing between the (hkl) planes, λ is the wavelength of X-ray used, n is order of diffraction and θ is glancing angle.

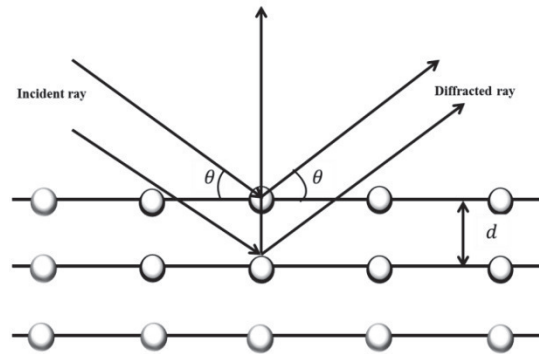


Fig. 3.9 Diffraction of X-rays from the crystal lattice

The most common technique for analyzing thin films as thin as 100 \AA is to use a ‘grazing incidence angle’ arrangement. Most instruments operate in Bragg- Brentano or para focusing $\theta:2\theta$ mode. The Bragg–Brentanno goniometers set up used in X-ray diffraction experiment is schematically represented in figure 3.10.

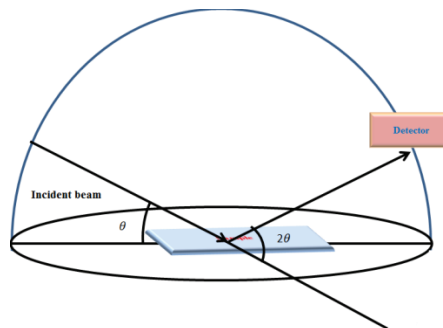


Fig. 3.10 Schematic representation of XRD in Bragg–Brentano geometry.

Here, the X- ray tube is stationary, the sample and the detector moves simultaneously. The incoming beam makes an angle θ w.r.t. the sample surface and the detector simultaneously makes an angle 2θ with the incoming ray. The XRD pattern typically contains many distinct peaks each corresponds

to different interplanes spacing d of the (h k l) planes causing reflections. Then the experimentally observed diffraction pattern is compared with (ICDD), is an organization that maintains the database of inorganic and organic spectra.

In the present investigation the following structural parameters are estimated from XRD using the relations:

1. The particle size is calculated using Debye Scherrer's formula [17]

$$D = \frac{0.9\lambda}{\beta \cos \theta} \quad (3.22)$$

where λ is the wavelength of X-ray used and β (in radian) is full width at half maximum (FWHM) of the most intense diffraction line.

2. The dislocation density (ρ) in the layers is calculated using the relation

$$\rho = \frac{1}{D^2} \quad (3.23)$$

3. The number of crystallites per unit area (N) is calculated as;

$$N = \frac{t}{D^3} \quad (3.24)$$

where t is the thickness of the film.

4. The strain in the film is calculated using the relation

$$T = \left(\frac{1}{\sin \theta} \right) \left[\frac{\lambda}{D} - \beta \cos \theta \right] \quad (3.25)$$

5. Lattice parameters for a cubic system can be calculated using the following relation

$$d = \frac{a}{\sqrt{(h^2+k^2+l^2)}} \quad (3.26)$$

In the present study of XRD analysis was done using Rigaku D Max C X-Diffraction with Cu-K α (with $\lambda=1.5406 \text{ \AA}$) as a source radiation with scan

speed of 5° per minute. The accelerating voltage is 30 KV and tube current is 20 mA.

3.4.2 Measurement of film thickness

Thickness is a most significant film property as compared to the bulk. Various techniques are available to characterize the film thickness, which are mainly divided into direct and indirect method. In this, thickness is measured either by in-situ monitoring of the rate of deposition or after the film deposition. Since the film thickness is generally of the order of the wavelength, various optical techniques such as optical interference and ellipsometry can be used. In addition to optical techniques, there are some mechanical, electrical and magnetic methods. In the present study, film thickness is measured using Fizeau's multiple beam interferometry techniques and stylus method.

(a) Fizeau's multiple beam interferometry technique

Tolansky has developed this interference fringe technique. The schematic representation of the apparatus for producing Fizeau's fringes is shown in figure 3.11(a). The film whose thickness is to be measured is deposited on a glass substrate with sharp edge. This technique is based upon situating two surfaces of reflectivity and beams have undergone multiples reflections between the surfaces. For this an over layer of highly reflecting opaque film is deposited on the sample under study and a semitransparent film is deposited on a bare substrate using thermal evaporation. These film surfaces are made in contact using a tightly fined circular jig with three tilt adjustment screws.

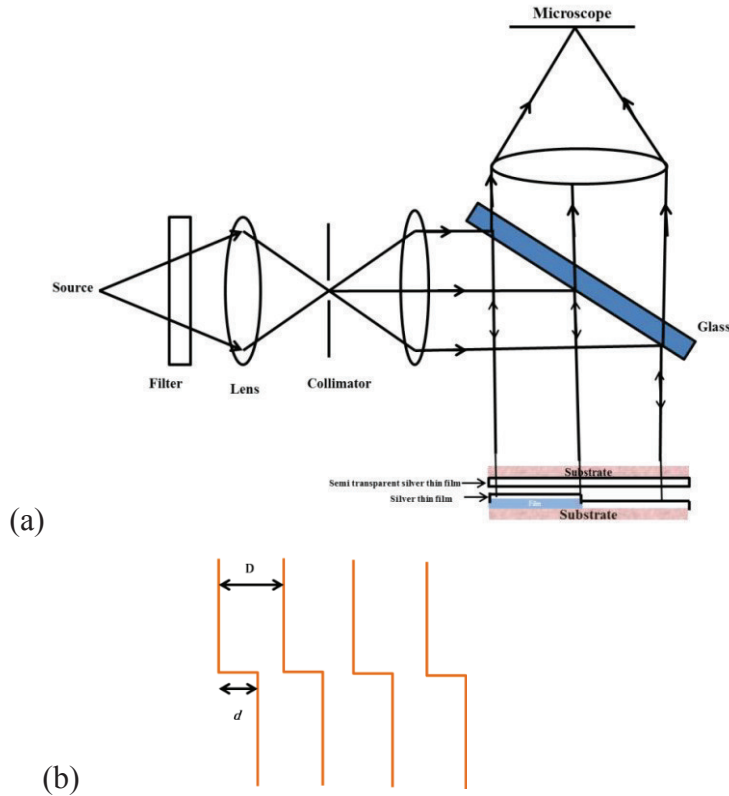


Fig. 3.11(a). Schematic illustration of multiple beam interferometer arrangement (b) Fringes with steps produced by multiple beam interferometry.

When this incident monochromatic beam normally enters this arrangement, multiple reflections between these opposite surface occur and the reflected fringe system consists of very fine dark lines against a green background with a maximum fringe width of $\frac{\lambda}{2}$ (Figure 3.11(b)). The interferometer consists of a very well collimated narrow band monochromatic beam of wavelength λ (green filter with $\lambda=546.1$ nm). The distance D between

successive fringes corresponds to $\frac{\lambda}{2}$. The abrupt displacement d of the fringe system due to sharp step on the substrate is a measure of film thickness t , which is given by

$$t = \frac{d\lambda}{2D} \quad (3.27)$$

The limit of measurement of this technique is therefore of the order of $\frac{\lambda}{2}$. The film thickness can be measured to an accuracy of $\pm 10 \text{ \AA}$.

(b) Stylus Method

Among the various thickness measurement methods most widely used technique is stylus method. The apparatus is known as Talysurf instrument consists of a diamond tipped probe, which can be mechanically driven across the work piece. Figure shows the basic block diagram of Veeco Dektak 6M surface profiler. The block diagram of the instrument is shown in figure 3.12.

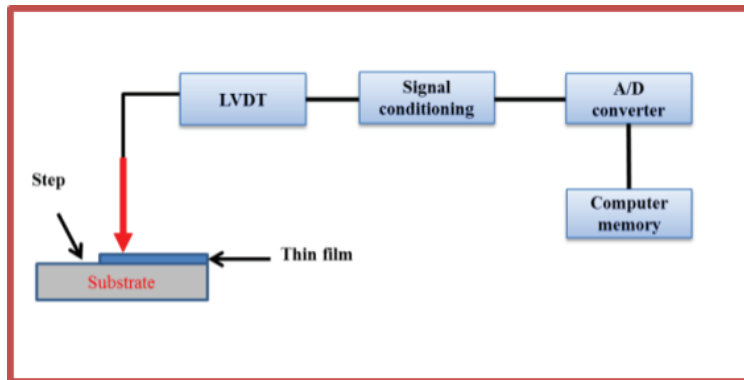


Fig. 3.12 Schematics representation of thickness profiler.

In principle, the instrument compares the vertical movement of the stylus travelling across the sample surface. When a scan routine begins the stylus lowers and the tip contacts the simple surface and the 6M profiler scan

routine consists of sixteen individual parameters such as scan length, stylus force, speed, leveling etc.

The stylus is mechanically coupled to the core of an LVDT (Linear Variable Differential Transformer). As the stage moves the sample, the stylus rides over the sample surface. Surface variations cause the stylus to be translated vertically. Electrical signals corresponding to stylus movement are produced as the core position of the LVDT changes. The LVDT scales an AC reference signal proportional to the position change, which in turn is conditioned and converted to a digital format through a high precision, integrating, analog-to-digital converter[17]. The surface feature encountered by the stylus are represented as a two dimensional profile which is plotted, scaled and displayed on the computer monitor.

3.4.3 Measurement of conductivity type: - hot probe method

Hall effect and thermoelectric power (TEP) measurements are useful methods to determine the type of carriers in semiconducting samples. But it requires a good deal of sample preparation. Hot probe experiments provide a very simple and convenient way to determine the type of conductivity of semiconductors using a soldering iron and a standard multimeter. In this method, the sign of thermal emf or Seebeck voltage generated by a temperature gradient determines the conductivity type. The experimental arrangement is shown in figure 3.13. It is performed by contacting one end of semiconducting sample with a hot probe such as heated soldering iron and other end with a cold probe. Both probes are wired to a sensitive voltmeter. The hot probe is connected to the positive terminal of the voltmeter while the cold probe is

connected to the negative terminal. When the probes are connected to a n-type material, one obtains a positive voltage while p-type material yields a negative voltage. Hot probes are effective over the resistivity range of about 10^{-3} to 10^3 Ωcm . The temperature gradient in the sample generates a current.

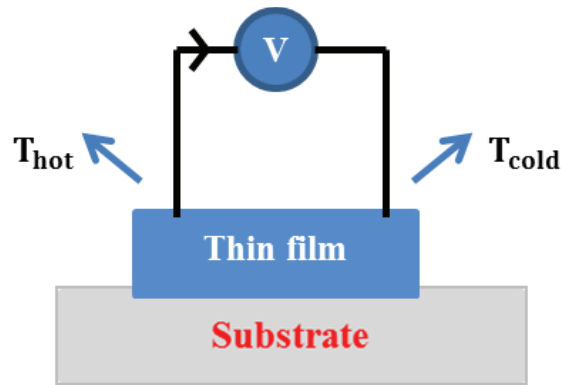


Fig. 3.13 Schematic arrangement for measurements of conductivity type

The majority carrier currents in n and p type material are given by

$$J_n = -qn\mu_n P_n \frac{dT}{dx} \quad (3.28)$$

$$J_p = -qp\mu_p P_p \frac{dT}{dx} \quad (3.29)$$

where $P_n < 0$ and $P_p > 0$ are differential temp. If $\frac{dT}{dx}$, electron current in n-type sample flows from hot to cold. That is electrons diffuse from hot to cold end setting up an electric field by the voltmeter with the hot probe positive with respect to the cold probe. The voltmeter tends to indicated n-type for high resistivity material even if the sample is weakly p-type because the method actually determines the $n\mu_n$ or the $p\mu_p$ product. With $\mu_n > \mu_p$ intrinsic or high resistivity material is measured n-type if $n \approx p$. In semiconductors with

intrinsic concentration $n_i > n$ or $n_i > p$ at room temperature, it may be necessary to cool one of the probes and let the room temperature probe be the hot probe.

3.4.4 Electrical conductivity measurement

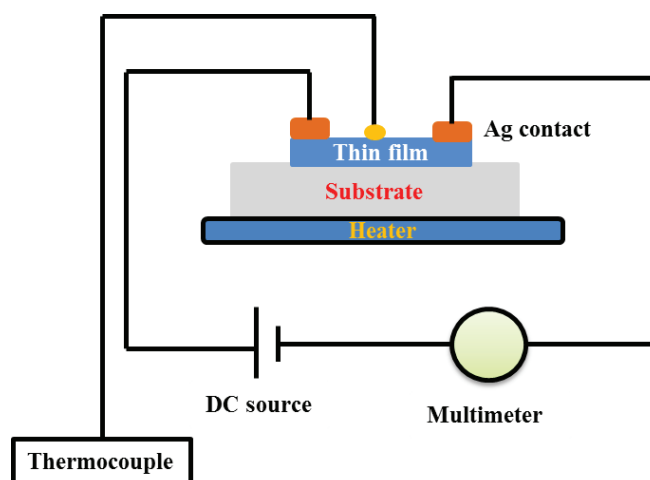


Fig. 3.14 Schematic arrangement for measurements of electrical conductivity

The electrical conductivity measurements were carried out by dc two probe method in a conductivity cells (figure 3.14). The cell was evacuated to 10^{-2} torr using a rotary pump to avoid the possibility of short-circuiting of the sample due to humidity present in the sample. Samples of dimension of about 3.2×1.4 cm were used for measurements with silver paste as ohmic contact. The variations of $\ln(I)$ with temperature at constant voltage was studied in the temperature range 300-443 K at an interval of 5 K for three continuous heating cooling cycles. The temperature of the specimen was measured using a

chromal-alumel thermocouple. The measuring cell and heater were earthed properly to avoid disturbances.

The resistivity ρ of a semiconductor depends on the free electron and hole densities (n and p) and the corresponding mobilities (μ_n and μ_p) as:

$$\rho = \frac{1}{q(n\mu_n + p\mu_p)} \quad (3.30)$$

For extrinsic semiconductor majority carrier density is much higher than the minority carrier density, it is generally sufficient to know majority carrier and its mobility. However if carrier densities and motilities are not known the alternative technique is the two probe or two contact arrangement. This is an easy technique to implement because only two probes need to be manipulated. Each contact serves as a current and as a voltage probe in two probes the total resistance R_T is given by

$$R_T = 2R_p + 2R_c + R \quad (3.31)$$

where R_p is the probe resistance, R_c is the contact resistance and R is the sample resistance under study. Here R_c is very small compared to R and by choosing suitable probes we make its contribution negligible.

3.4.5 Photoconductivity measurement

Photoconductivity studies involve I-V measurements conducted under illumination. Silver electrodes are deposited over the films for ohmic contact. Keithley 2611A sourcemeter is used to give DC bias voltage to the sample and current is measured at room temperature. The experimental set up used for recording the photocurrent is shown in the figure 3.15.

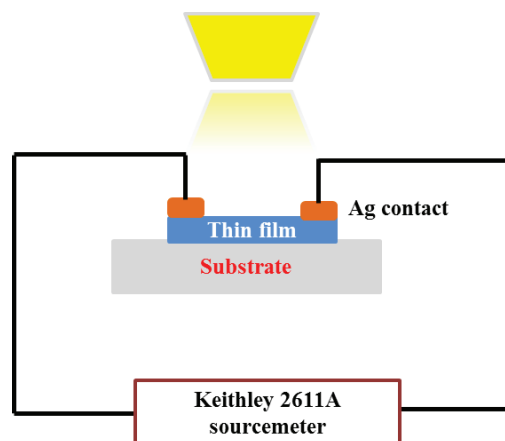


Fig. 3.15 Schematic arrangement for measurements of
Photoconductivity

3.4.6 Scanning Electron Microscopy (SEM)

The SEM provides the three dimensional high resolution images of organic and inorganic materials on a nanometer to micrometer scale. The type of signals produced from the interaction of the electron beams with the sample include secondary electrons (SE), back scattered electrons (BSE), characteristic x-rays and other photons of various energies. For SEM images, the signals of greatest interest are the SE and BSE because these vary primarily as a result of difference in surface topography [18]. In SEM (figure 3.16), the surface of sample is coated by an electrically conductive layer of gold. The coated sample is placed in vacuum so that highly energetic electron beams from electron gun (a thin tungsten wire) can move without interference. The electron gun works at a voltage between 2 to 50 KV and electrons are focused by magnets into the sample.

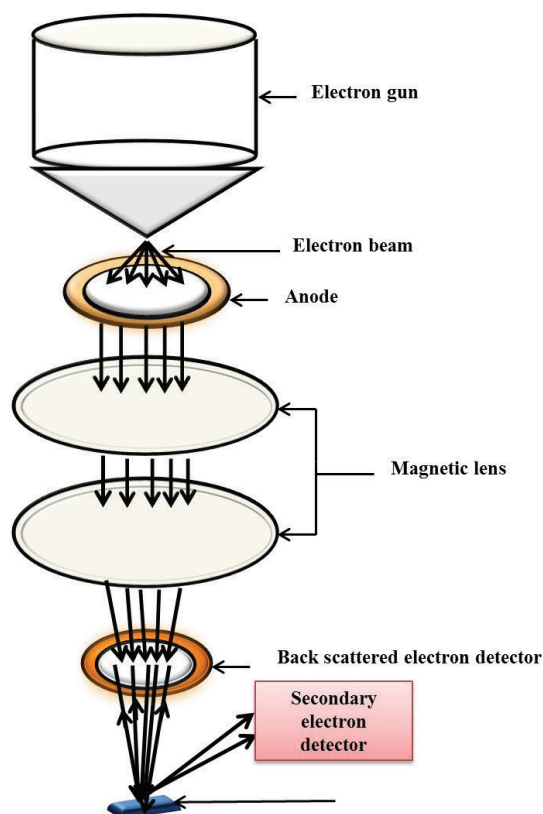


Fig. 3.16 Optical ray diagram of SEM instrument

The beam strikes the sample and it interacts with the specimen. The detector of the system collects the SE and BSE and generates signals to form image. Two pairs of electromagnetic deflection coils (scan coil) are used to sweep the beam across the specimen. In this work, the elemental analysis and surface morphology were studied using the SEM instrument JEOL Model JSM-6390 LV (magnification: 5X to 3, 00,000X, resolution: 4nm).

3.4.7 EDAX

Energy dispersive x-ray analysis (EDAX, EDS or EDX) is an analytical technique to obtain the elemental composition of a sample. The EDAX works as an integrated feature of a SEM and cannot be operated its own without the later[19]. As a type of spectroscopy, it relies on the investigation of a sample through interaction between the incident radiation and matter, analyzing x-rays emitted by the matter in response being hit with charged particles. Its characterization capabilities are due in large part to the fundamental principles that each element has a unique atomic structure allowing x-rays that are characteristics of an element's atomic structure to be identified uniquely from each other. During EDAX the specimen is bombarded with a high energy beam of charged particles such as electrons or x-rays [20]. At rest, an atom within the sample contains ground state electrons in discrete energy levels. The incident beam excites an electron in the inner shell, ejecting it from the shell and creates an electron hole. An electron from the outer shell then fills the hall and the difference in energy between the higher energy and lower energy shells is released in the form of x-rays. As the energy of the x-rays are characteristics of the difference in energy between the two shells and of the atomic structure of the element from which they are emitted, by measuring the number and energy of the x-rays emitted the identity of the atom from which x-rays are emitted can be established. The characteristics x-ray lines are named according to the shell in which the initial vacancy occurs and the shell from which electron drops to fill those vacancies (Figure 3.17).

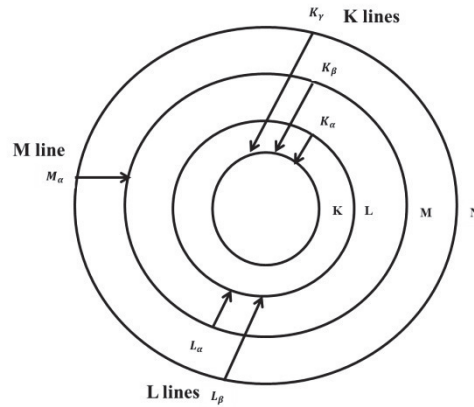


Fig. 3.17 Schematic of electron transitions responsible for the production of K_α , K_β , K_γ , L_α , L_β and M_α x-rays

For example if initial vacancy occurs in the K shell electron drops from the adjacent (L) shell, to fill it, the emitted x-ray is K_α x-ray [21]. If the electron drops from M shell, the emitted x-ray is K_β x-ray. Similarly if an L shell electron is ejected and an electron from M shell fills the vacancy L_α radiation will be emitted. When a K shell vacancy is created, the most probable transmission is the L to K transmission. Therefore K_α radiation will always be more intense than K_β radiation. The energy released during electron transmission between adjacent electrons shells become less, progressing outward from the nucleus. That is for a given atom, M_α radiation will be lower than the L_α radiation, which in turn will be of lower energy than K_α radiation.

3.4.8 Atomic Force Microscopy (AFM)

The atomic force microscope is a part of large family of instruments termed scanning tunneling microscope (STM). The common factor in all STM technique is a very sharp probe which is scanned over the area of interest of the

sample and interacts directly, simultaneously monitoring the high resolution image of the sample surface. AFM was first described by Binnig et al as a new technique for imaging topography of the surfaces at high resolution [22].

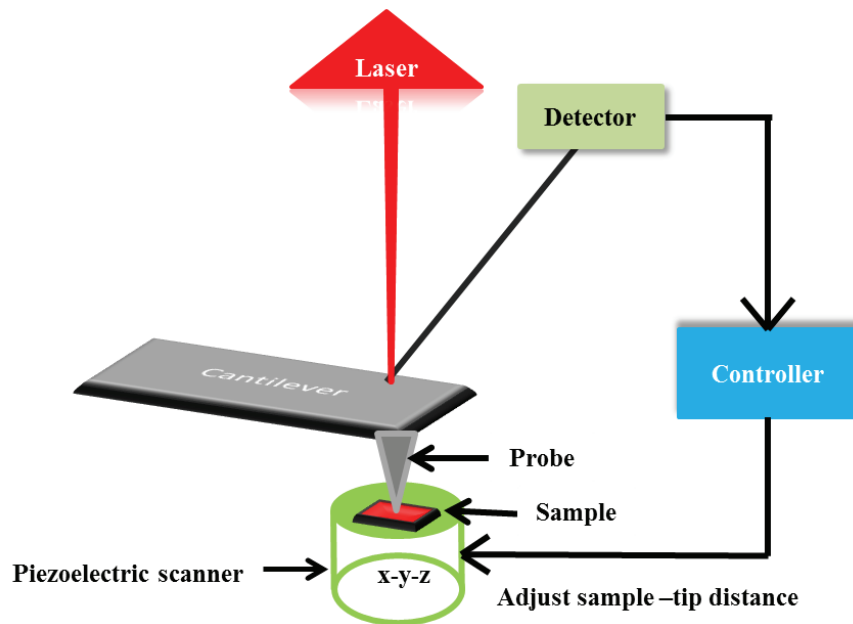


Fig. 3.18 Schematic diagram of AFM

In AFM the probe is a stylus, mounted near to the end of a flexible cantilever. The cantilever is typically silicon or monolithic Si_3N_4 with a tip radius of curvature of the order of nanometers. The dominant interactions at short probe-sample distances in the AFM are Van der Waals interactions. Depending upon the properties of the samples and information to be extracted from it, two techniques of imaging are done: static technique (contact mode or repulsive mode) where the probe remains in constant contact with the sample

and dynamic technique (intermittent or non-contact mode) where the cantilever may be oscillating. The basic set up for an AFM is shown in figure 3.18. The sharp probe tip is attached to the end of a spring cantilever with a low spring constant, typically between 0.06 Nm^{-1} and 0.6 Nm^{-1} .

As the sample is scanned under the tip, the x , y and z position of the sample surface with respect to the tip is determined by a piezoelectric tube scanner. Deflection of the cantilever is monitored by the measuring the change in the path of the laser beam deflected from the upper side of the end of the cantilever by a photodetector. Any deflection of the cantilever will produce a change in the position of the laser spot on the photodetector and it is monitored. This can be used to calculate the interaction force between the probe and the sample.

3.4.9 Thermoelectric power (TEP)

Automated precision measurement setup for electrical resistivity and thermoelectric power of different types of samples in the temperature range of 5–325 K have been used in the present study for low temperature electrical and thermoelectric power measurements. The experimental set up is shown in the figure 3.19.

The cryostat with a vacuum maintained inside better than 10^{-6} mbar houses the sample holder assembly. The cryostat is essentially fabricated using an SS tube brazed with oxygen free highly conducting copper (OFHC) solid rod made as cup at the bottom, a ball valve, and a vacuum port near the neck with the top-end fitted with an appropriate sample holder. The thermoelectric power (S) measurement system is configured for differential dc method with OFHC as reference. The sample with freshly clean surfaces is secured between

two cylindrical OFHC blocks using an SS spring and an axial brass screw. The two junctions of the chromel-Au-Fe thermocouple are anchored thermally to the two OFHC blocks to which electrical leads are attached that enable good electrical contacts for the thermally generated potential difference (ΔV) measurements. A temperature controller is used to maintain the temperature difference (ΔT) between the two OFHC blocks using the chromel-Au-Fe thermocouple and a heater wire wound on the lower OFHC block. The schematic representation of the experimental arrangement is shown in figure 3.19.

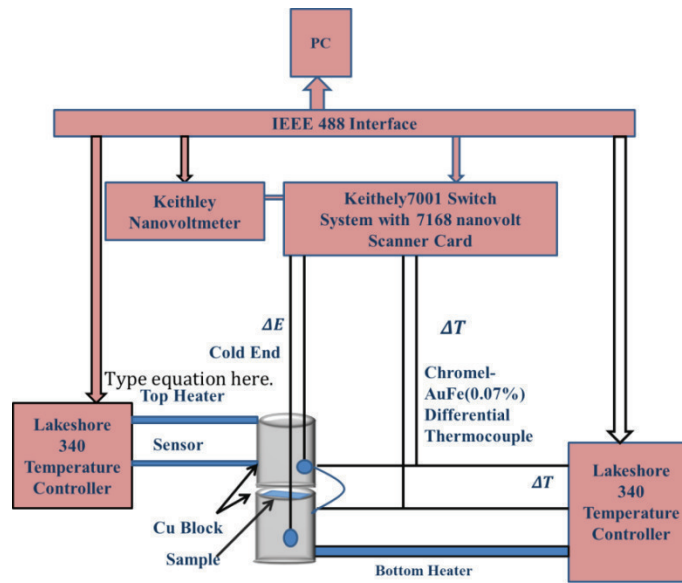


Fig. 3.19. The experimental set up for TEP measurement

The ΔT is set to 2 K. A silicon diode and another heater anchored to the upper OFHC block are connected to another temperature controller to sustain a desired controlled sample temperature of ± 10 mK. The nanovoltmeter

measures ΔV and ΔT via the chromel-Au-Fe thermocouple. The sample holder is attached to a heat sink via three SS rods and a hylum disk. A removable cylindrical OFHC jacket fits at the bottom of the brass flange as a radiation shield.

The measured TEP data gives S_{meas} as [23]

$$S_{meas} = \frac{\Delta V}{\Delta T} \quad (3.32)$$

The Seebeck coefficient of the copper reference S_{Cu} is subtracted from the measured S_{meas} such that the sample S is given as

$$S = S_{meas} - S_{Cu} \quad (3.33)$$

The reliability of the S_{Cu} data used for subtraction from the measured S_{meas} has been satisfactorily proven as the measured data on the standard samples match the published data.

3.4.10 X ray Photoemission Spectroscopy (XPS)

XPS is a surface sensitive technique used to analyze surface chemical composition and bonding. A sample is irradiated with monoenergetic soft x-rays beam while the identification of the elements in the sample can be made directly from the number of photoelectrons that escape and the kinetic energies of these ejected photoelectrons.. An important advantage of XPS is its ability to obtain information on chemical states from the variations in binding energies, or chemical shifts, of the photoelectron lines.

The interaction of an X-ray photon with a sample leads to the ejection of photoelectrons (dominates at high energy x-rays of about 10 KeV), as shown schematically in Figure 3.20(a). After the initial photoelectron, an upper level valence electron relaxes into the vacant core-level state, followed by an

ejection of Auger electron (dominates at low energy x-rays of about 1 KeV, in which photon ionises a core level, leaving a hole. The hole is filled by a higher energy electron and the subsequent energy is transferred to another electron, which then escapes.) as in figure 3.20(b) [24].

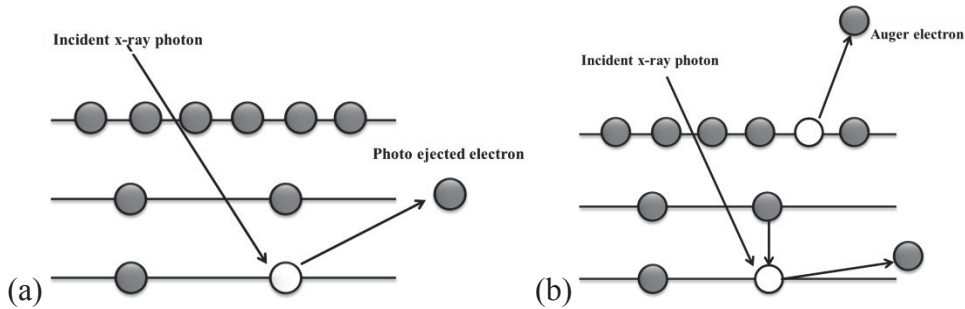


Fig. 3.20 Process involved in (a) photoelectron emission, (b) Auger electron emission

When an X-ray beam directs to the sample surface, the core electron of an atom adsorbs the energy of the X-ray photon completely. If the photon energy, $h\nu$, is large enough, the core electron will then escape from the atom and emit out of the surface. The emitted electron with the kinetic energy of E_k is referred to as the photoelectron. The binding energy (BE) of the core electron E_b is given by the Einstein relationship [25]:

$$h\nu = E_b + E_k + \varphi_s \quad (3.34)$$

E_k can be measured by the energy analyzer; and φ_s is the work function induced by the analyzer, about 4~5 eV. Since the work function φ_s can be compensated artificially, it is eliminated, giving the binding energy as follows:

$$E_b = h\nu - E_k \quad (3.35)$$

Thus by measuring the KE of the photoelectrons we can determine the BE of the electrons. An XP spectrum is generated by plotting the measured photoelectron intensity as a function of BE. The BEs of these lines is characteristic for each element, and is a direct representation of the atomic orbital energies.

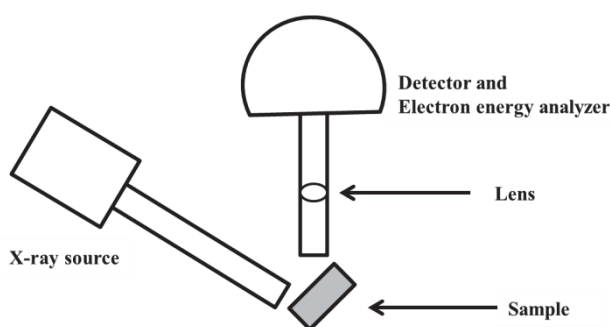


Fig. 3.21. The basic set up for XPS

Basic requirements for XPS measurement are shown in figure 3.21. A high vacuum environment is required (a) to enable the emitted photoelectrons to be analyzed without interference from gas phase collisions); XPS system (b) To avoid contamination of active surface; (c) To extend the lifetime of X-ray source and other electronic optics in the XPS system. The sample is irradiated with monochromatic X rays, and the resultant photoelectrons are collected by a transfer lens. The photoelectrons are selected based on their kinetic energy by the hemispherical analyzer and collected at the detector [26].

3.4.11 Hall effect

The electrical resistivity and Hall coefficient are important material properties. They play an important role in any field of research concerned with the electronic transport properties of materials such as semiconductors and

metals. From the Hall coefficient, the charge carrier concentration can be directly calculated [27]. The van der Pauw (VDP) method is a convenient measurement method for the evaluation of various properties such as resistivity, carrier density, type of carriers and mobility of carriers of semiconductor thin films. For the present study, Ecopia HMS-3000 using van der Pauw technique with a magnetic field of 0.55 T was used to measure the transport properties at room temperature.

3.5 Aim of the present work

As part of our work, we have selected certain semiconducting chalcogenide thin films like lead selenide (PbSe), lead antimony selenide ($\text{Pb}_{3.58}\text{Sb}_{4.42}\text{Se}_{10}$), silver selenide (Ag_2Se) and silver antimony selenide (AgSbSe_2) which are preferred candidates for improving the potential of green technologies such as photovoltaic and thermoelectric in tackling the energy needs and environment issues arising in this technology oriented world. Therefore the present work aims on transport and optoelectronic properties of these thin films prepared using reactive evaporation technique.

References

- [1] K. Seshan, *Handbook of Thin-Film Deposition Processes and Techniques*, 2nd ed. Noyes Publications / William Andrew Publishing, 2002.
- [2] Gary E. McGuire, *Semiconductor Materials and Process Technology Handbook for Very Large Scale Integration (VLSI) and Ultra Large Scale Integration (ULSI)*. Noyes Publications/William Andrew Publishing, 1988.
- [3] M. Ohring, *Materials Science of Thin Films Deposition and structures*,

- 2nd ed. Academic Press, 2002.
- [4] H. Frey and H. R. Khan, *Handbook of Thin Film Technology*. Springer, 2015.
- [5] Dler Adil Jameel, “Thin Film Deposition Processes,” *Int. J. Mod. Phys. Appl.*, vol. 1, no. 4, pp. 193–199, 2015.
- [6] K. L. Chopra, *Thin Film Phenomena*. McGraw-Hill, New York, 1969.
- [7] L. I. Maissel and R. Glang, *Handbook of thin film technology*. McGraw-Hill, India, 1970.
- [8] A. Goswami, *Thin Film fundamentals*. New age international Pvt. Ltd. New Delhi, India, 1996.
- [9] J. A. Venables, G. D. T. Spiller and M. Hanbucken, “Nucleation and growth of thin films,” *Rep. Prog. Phys*, vol. 47, pp. 399–459, 1984.
- [10] J. A. Venables, “Nucleation and growth processes in thin film formation,” *J. Vac. Sci. Technol. B*, vol. 4, pp. 870–873, 1986.
- [11] M. Ohring, *The Materials Science of Thin Films*. Academic Press, 1992.
- [12] A. Von Keudell, “Surface processes during thin-film,” *Plasma Sources Sci. Technol.*, vol. 9, pp. 455–467, 2000.
- [13] K. G. Gunther, *The Use of Thin Films in Physical Investigations (J.C. Anderson Ed)*. Academic Press, London, 1966.
- [14] A. Guthrie, *Vacuum Technology*. John Wiley & sons, Inc publishing, 1963.
- [15] G. L. Weissler and R. W. Carlson, *Vacuum Physics and Technology*.

- Academic Press, 1980.
- [16] B. D. Culity, *Elements of X-ray diffraction*, 2nd ed. Addison- Wesley publishing company, Inc, 1977.
- [17] “Dektak 6M Manual.”
- [18] J. R. Michael, K. Joseph Goldstein, Dale E. Newbury, David C. Joy, Charles E. Lyman, Patrick Echlin, Eric Lifshin and Linda Sawyer, *Scanning Electron Microscopy and X-ray Microanalysis*, 3rd ed. Academic/Plenum publishers, 2003.
- [19] D. K. Schorder, *Semiconductor material and device characterisation*, 3rd ed. John Wiley & sons, Inc publishing, New York, 1998.
- [20] C. Jacoboni, C. Canali, G. Otiaviani and A. A. Quaranta, “a review of some charge transport properties of silicon,” *solid state Electron.*, vol. 20, pp. 77–89, 1977.
- [21] C. Suryanarayana, *Experimental Techniques in Materials and Mechanics*. CRC Press Taylor and Francis group, 2011.
- [22] W. Richard Bowen and Nidal Hilal, *Atomic Force Microscopy in Process Engineering: An Introduction to AFM for an improved processes and products*. Butterworth-Heinemann publishing, 2009.
- [23] A. Soni and G. S. Okram, “Resistivity and thermopower measurement setups in the temperature range of 5 – 325 K,” *Rev. Sci. Instrum.*, vol. 79, no. 2008, p. 125103 1–4, 2008.
- [24] Charles C. Chusuei and D. W. Goodman, *X-ray photoelectron spectroscopy*. Academic Press, 2002.
- [25] J. F. Watts, “X-ray photoelectron spectroscopy,” vol. 45, pp. 653–671,

1994.

- [26] T. Nunney and R. White, “Characterizing Materials for Energy Generation Using X-ray Photoelectron Spectroscopy (XPS),” *Micros. Today*, pp. 22–28, 2011.
- [27] K. A. Borup, E. S. Toberer, L. D. Zoltan, G. Nakatsukasa, M. Errico, K. A. Borup, E. S. Toberer, L. D. Zoltan, G. Nakatsukasa, and M. Errico, “Measurement of the electrical resistivity and Hall coefficient at high temperatures,” *Rev. Sci. Instrum.*, vol. 83, p. 123902 1–7, 2012.

Chapter 4

Reactively evaporated p-type lead selenide thin films and its characterization

4.1 Introduction

4.2 Experimental details

4.3 Results and discussions

4.4 Conclusion

4.1 Introduction

The use of thin film semiconductors has recently been attracted much interest due to their remarkable applications in various electronic and optoelectronic devices. Among IV-VI semiconducting narrow band gap compounds, lead chalcogenides attract considerable scientific attraction due to the technological importance of these materials, in crystalline and polycrystalline forms as IR detectors, solar cell, solar control coatings, photographic plates and photoconductive absorber and analyzers [1]–[4]. Among the available lead chalcogenides, semiconductor PbSe has been extensively studied due to its unique optical and electrical properties. Since most sensitive detectors for mid-infrared range are obtained with narrow band gap semiconductors, several researchers interested to introduce PbSe in thin film and nano particle form. Also PbSe quantum dot (QD) plays an important

role in multiple Exciton generation and the quantum efficiency is high due to the direct band gap [3]. Thin films of PbSe have been prepared by researchers using various experimental techniques including electrochemical deposition [5], [6], thermal evaporation [7], [8], physical vapor transport method [9], chemical deposition [10]–[13]. Several techniques such as photochemical, sonochemical, pulsed laser deposition, pulse sonochemical method and successive ionic layer adsorption and reaction method have also been used in the deposition of PbSe thin films [14], [15]. Of the various methods, the changes in physical properties of thin film are caused by method of deposition, substrate material, substrate temperature, cleanliness of the substrate, rate of deposition and the background pressure.

For several decades, efforts have been made to achieve the goal of finding high-temperature infrared detectors based on lead selenide, attempts have been made to grow high-quality and high-resistivity materials. It was observed by Wagner et al [8] that substrate temperature and source purity have a pronounced effect on the morphology, resistivity, and crystallinity of PbSe thin film produced by physical vapour transport method. Tetyorkin [11] reported photosensitivity of n-type (001) oriented PbSe films grown on Si substrates using a thin YbS buffer layer. By using atomic force microscopy it is also observed that the growth of PbSe thin films could be optimized in terms of the modifications of the surface topography by properly controlling the deposition periods [16]. Recently vacuum evaporation technique is employed in order to study the thickness dependence structural, electrical and optical properties of PbSe thin films [3]. Here it is found that the obtained optical band

gap of the films lies between 1.5 and 1.9 eV, provides potential for application in solar cell.

A survey of literature reveals that metal chalcogenide compounds which are predominantly semiconductors have appropriate band gap for thermoelectric (TE) applications over a wide range of temperatures typically 100-1400 K [17]. Moreover the low thermal conductivity of chalcogenides due to high atomic weight is a key property that leads to high figure of merit and the dimensional reduction could further boost the TE properties of the semiconducting compounds [18]. Over the past decades alloys based on Bi₂Se₃, PbTe and SiGe systems have been studied extensively and are used as TE materials in various solid state TE power generation and refrigeration applications. Thermoelectric devices based on thin film materials have attracted considerable attention because of, due to small thickness, thin film applications allow high heat fluxes and low thermal resistances which deliver much higher power densities compared with conventional modules [19]. However, bismuth, lead and antimony chalcogenide compounds are investigated in the form of thin films, the best quality thin film obtained is co-evaporated Bi₂Te₃, has room temperature power factor = $2.05 \times 10^{-3} \text{ Wm}^{-1}\text{K}^{-2}$ for p-type and $3.09 \times 10^{-3} \text{ Wm}^{-1}\text{K}^{-2}$ for n-type [20]. Although some thermoelectric materials, such as Bi₂S₃ and Bi₂Te₃ films, have found particular applications, their efficiencies are not enough for wider utilization in commercial applications. Thus it is timely and necessary to search for novel TE materials with high performance in different temperature ranges and low cost and to seek economical ways of manufacturing TE materials.

The recent progresses on thermoelectric materials are discussed in various articles [18], [21]–[23]. The narrow band gap is one of the most essential properties of lead selenide semiconductors ($E_g > 0.29$ eV) leading to the huge experimental exploration in these materials, especially for direct-gap semiconductors as a TE device, the optimal gap is found to be higher than $6k_B T$ where k_B is the Boltzmann constant and T is the ambient temperature [24]. V. Damodara Das and K. Seetharama Bhat [25] reported that as PbTe, PbSe films are also nonstoichiometric in nature and their carrier concentration is quite higher than that reported for the bulk. As PbTe, lead selenide also crystallises in the NaCl crystal structure with Pb atoms occupying the cation sites and Se forming the anionic lattice [26].

In the present work, reactive evaporation technique has been employed for the preparation of p-type PbSe thin films. In this thesis the X-ray diffraction studies, which illustrate the formation of PbSe, morphological, electrical as well as its optical properties, are reported. Transient photoconductivity measurements are important because the rise and decay of photocurrent with time shows the presence of traps or recombination centres in the band gap of the materials. The traps originate from the defect states present in the materials. The photoconductive measurements under illumination are also presented. To our knowledge, there have been a little studies on the thermoelectric properties of PbSe thin films. Therefore this chapter emphasize on investigation of TE properties of p-type PbSe thin films for low temperature TE applications.

4.2 Experimental details

Thin films of lead selenide were deposited onto ultrasonically cleaned glass substrates using the Gunther's three temperature method under a working pressure of 10^{-5} torr. In this three temperature means, lead and selenium can be evaporated from separate sources and the PbSe films are deposited on the glass substrate kept at a constant temperature of about 373 ± 5 K. The molybdenum boat and a glass crucible kept in molybdenum basket, which could be heated to different temperatures, were loaded with lead (99.999%) and selenium (99.999%) respectively. Initially sufficient selenium atmosphere was attained inside the chamber by adjusting the current through the selenium source and then boat was heated to evaporate lead. The shutter was opened and constant rate of deposition was maintained throughout the deposition period. The substrate temperature was measured using a fine wire chromel-alumel thermocouple. Immediately after deposition, the substrate temperature was reduced stepwise and the samples were cooled down to room temperature.

Substrate temperature and impingement rates are important parameters as they are directly related to the growth process, thereby the morphology and properties of the thin films deposited using reactive evaporation. Condensation of exact stoichiometric compound by simultaneous evaporation of individual components should be possible only if a critical temperature and critical incident flux were achieved [27]. The optimized deposition parameters used for the preparation of the samples in the present work are given below.

Table 4.1 Deposition parameters:

Impingement rate of lead	$\approx 1.13 \times 10^{15} \text{ atoms cm}^{-2} \text{ s}^{-1}$
Impingement rate of selenium	$\approx 6 \times 10^{14} \text{ atoms cm}^{-2} \text{ s}^{-1}$
Substrate temperature	$= 373 \pm 5 \text{ K}$

Rigaku D-MaxC diffractometer was used to determine the X-ray diffraction pattern of the as prepared PbSe thin film with Cu-K α (wavelength $\lambda = 1.5406 \text{ \AA}$) as source radiation with scan speed of 2°/minute. The optical properties of the film were studied by the absorbance spectra recorded using JASCO V570 UV-Vis-NIR spectrophotometer. The surface morphology of the film was done by means of Scanning Electron Microscope (SEM) using JEOL JSM 6390 scanning electron microscope and Atomic Force Microscopy (AFM). Thickness of the film was measured using the Tolansky's multiple beam interferometric technique [28]. The photoconductivity measurements were done using Keithly 2611A source meter after illuminating the samples using a FSH lamp (82 V, 300 W). When the film is not illuminated, the current is mainly due to the flow of thermally generated carriers. Under illumination, free carriers are generated through the absorption of the incident photon, resulting in enhanced conductivity. Under the influence of an electric field these carriers are transported through the sample and the carriers start recombines after switching off of the light source. To record the photoconductivity of the films, a bias voltage was given and current was measured. The carrier concentration and mobility were measured at room temperature by means of Hall coefficient measurement (Ecopia HMS-3000/MS 0.55T Model, Korea). The thermoelectric power measurements were done

using automated precision measurement setups for electrical resistivity and thermoelectric power of different samples in low temperature region; the experimental set up used is described elsewhere [29].

4.3 Results and discussions

4.3.1 Structural analysis

Figure 1 shows the X-ray diffraction pattern of a typical PbSe thin film with thickness 170 nm. The presence of structural peaks in the XRD of PbSe thin films corresponding to (111), (200), (220), (311) and (222) reflections confirm the polycrystalline nature of the sample.

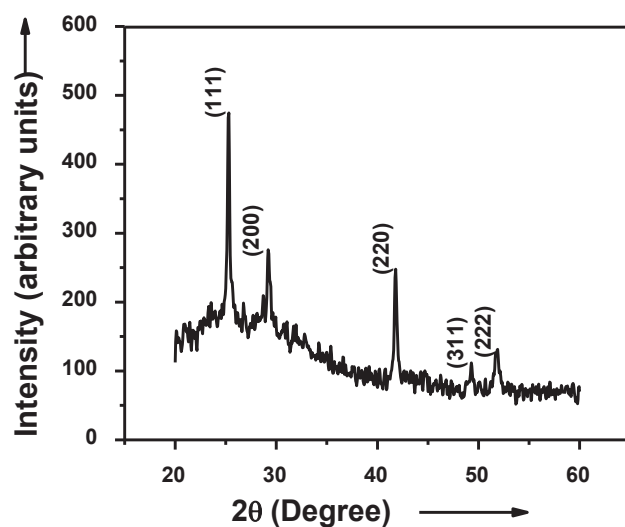


Fig. 4.1 X-ray diffraction pattern of a typical PbSe sample

Table 4.1 gives the comparison of the observed “d” values of as prepared sample with standard “d” values of ICDD Card No: 78-1903 [30]. Comparing the reflection planes of Figure 4.1 with the standard XRD data,

indicates that all the reflection planes can be indexed to face centred cubic phase of the binary compound PbSe ($f\bar{m}\bar{3}m$) with a lattice constant $a = 0.610$ nm. The values of microstructural parameters such as particle size, dislocation density, number of crystallites per unit area and strain calculated are tabulated in table 4.3 [31], [32].

Table 4.2 The observed XRD data along with standard ICDD data

Standard pattern(ICDD Card No: 78-1903)			As prepared film	
(hkl)	d(Å)	I/I ₀	d(Å)	I/I ₀
111	3.5341	37	3.522	100
200	3.0606	100	3.059	57
220	2.1642	66	2.162	52
311	1.8456	15	1.849	23
222	1.7670	21	1.762	28

Table 4.3 Microstructural parameters:

Average particle size D (nm)	38
Dislocation density ρ (lines m^{-2})	6.93×10^{14}
Number of crystallite per unit area N (m^{-2})	3.098×10^{15}
Strain T	2.253×10^{-3}

4.3.2 Morphological and compositional analysis

Figure 4.2 shows the SEM image of a typical PbSe thin film with 5,000 magnifications. It is observed that the film consists of irregularly shaped grains with well-defined boundaries are uniformly and thickly packed over the surface. The average grain size obtained is 500 nm which is much greater than

the size calculated from Scherrer's formula. This means that large grains consist of a large number of smaller crystallites which have the size estimated from Scherrer's formula. Figure 4.3 shows the EDX spectra for a typical sample of PbSe film deposited onto glass substrate.

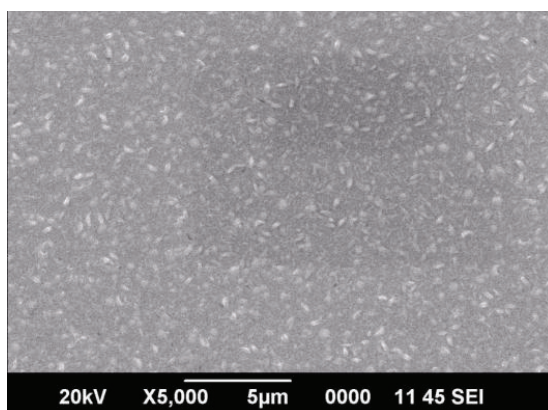


Fig. 4.2 Surface Morphology of lead selenide thin film

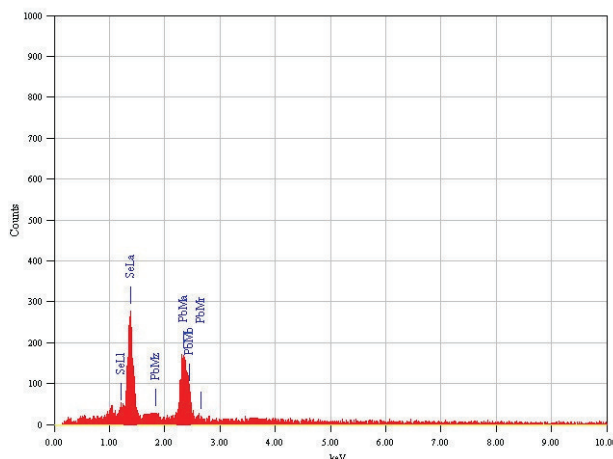


Fig. 4.3 EDAX spectra of a typical lead selenide thin film

Figures 4.4(a) and 4.4(b) illustrate the X-ray photoelectron spectra of Pb 3p, and Se 3d for a typical PbSe thin film. As can be observed, the Pb 3p_{1/2}

peak shown in Figure 4.4(a) is centered at about 112.42 eV. The Se 3d_{5/2} peak is shown in Figure 4.4(b) with binding energies of about 54.49 eV. The above results are compared with the standard elemental peak positions and it confirms the formation of PbSe thin film. The chemical composition of PbSe films has elemental composition of 50.7:49.3 corresponding to Pb:Se, which indicating a nearly stoichiometric composition.

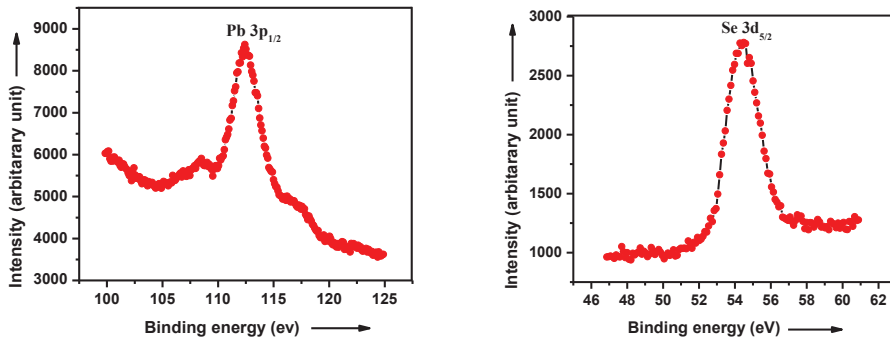


Fig. 4.4 Plots of (a) lead 3p spectra and (b) selenium 3d spectra of PbSe thin film

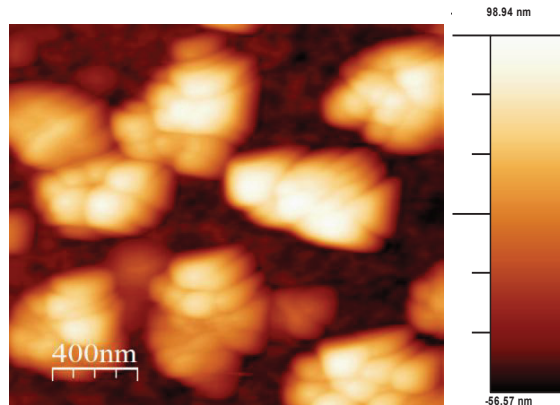


Fig. 4.5(a) The two dimensional AFM image of PbSe thin film (area 2 X 2 μm)

Figures 4.5(a) and 4.5(b) represent the two dimensional and three dimensional AFM images of PbSe thin film over an area of $2 \times 2 \mu\text{m}$. The figures show the formation of well-defined grains. The grain size obtained from the 2D image is 500 nm which is in agreement with the results obtained from the SEM analysis. Since the grains are grown with different size and shapes, the root mean square value of the surface roughness is estimated. The average surface roughness obtained from 3D image is 40 nm.

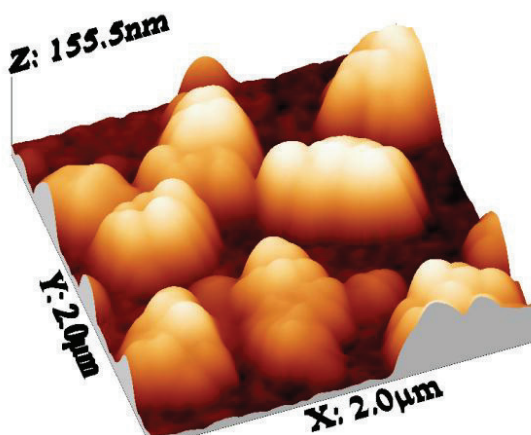


Fig. 4.5(b) The three dimensional AFM image of PbSe thin film (area $2 \times 2 \mu\text{m}$)

4.3.3 Electrical analysis

The hot probe method was used to check the type of conductivity of the samples, the films showed p-type conductivity. The temperature dependent electrical conductivity measurements are done in the range 300–423K, at a pressure of 10^{-2} torr using a two probe set up. Figure 4.6 shows the Arrhenius plot of current versus inverse of temperature for three continuous cycles. The activation energy is found to be 0.063 eV. As the conductivity of the samples is

p-type, acceptor-like levels is expected to be present in the band gap. During first heating, initially a uniform increase of current with temperature and after 393 K a relatively sudden decrease in current is observed. While cooling the plot is linear, exhibiting the semiconducting behaviour. This can be explained on the basis of the same observation seen in PbSe thin film prepared by thermal evaporation of the bulk proposed by Damodara Das V and Seetharama Bhat [24] through studying the electrical conductivity of the as-grown and air-exposed thin films.

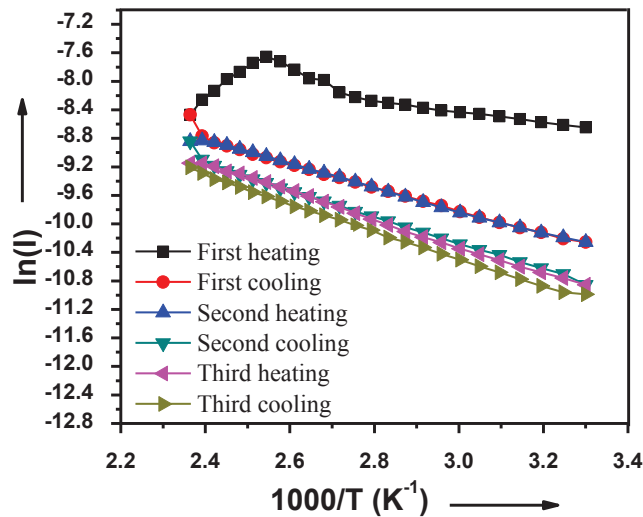


Fig. 4.6 Plot of $\ln(I)$ versus inverse of temperature for a typical PbSe film

In a typical air exposed sample, large number of oxygen atoms gets adsorbed on the film surface. During heating, in a typical PbSe thin film the observed initial decrease of resistance with temperature may be due to the intrinsic

conduction. Immediately after 393 K a rise in resistance with temperature is attributed to the desorption of these oxygen from the film surface and thereby bringing down the carrier concentration in a p-type sample. The formation of thermally generated defects at high temperature also decreases the mobility of the carriers. On cooling the thermally generated defects exhibit a hysteresis nature since the desorbed gas molecules are not adsorbed immediately in the vacuum chamber. The hysteresis reduces for other two cycles and it is also observed that cooling curves always lie below the heating curves.

4.3.4 Optical analysis

The absorbance spectra of a typical PbSe thin film recorded using the JASCO spectrophotometer is shown in Figure 4.7(a). The fundamental absorption edge in most of the chalcogenides follow an exponential law and above the absorption edge, the absorption coefficient (α) follows the Tauc relation as [33]

$$(\alpha h\nu) = A(\nu - E_g)^m \quad (4.1)$$

where ν is the frequency of the incident photon, A is a constant, E_g is the optical band gap and n is an exponent. The value of $m = 1/2, 3/2, 2$ and 3 for direct allowed, direct forbidden, indirect allowed and indirect forbidden transitions, respectively. The electronic transition between the valence and conduction bands starts at the absorption edge corresponding to the minimum energy difference between the lowest energy of the conduction band and the highest energy of the valence band in crystalline materials. Plot of $(\alpha h\nu)^2$ versus the photon energy for PbSe film is shown in Figure 4.7(b). Linearity of the plots indicates the allowed electronic transition across a direct band gap of

the PbSe film. Extrapolation of the linear part of the graph to the x-axis at $\alpha = 0$ gives the band gap energy E_g , which is 2.02 eV.

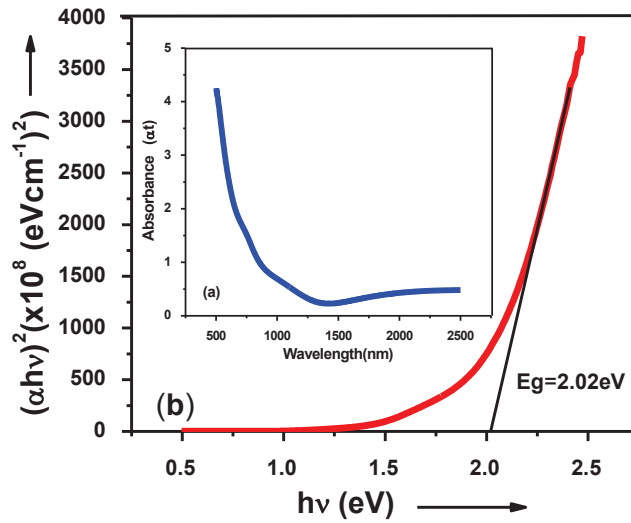


Fig. 4.7 Plots of (a) absorption spectra for a typical PbSe thin film, (b) the dependence of $(\alpha h\nu)^2$ vs $h\nu$.

The value of the absorption coefficient is found to be in the range 10^4 cm^{-1} to 10^5 cm^{-1} and the film is highly absorbing. Prabahar et al [34] studied optical properties of PbSe thin films in the spectral range 2500-5000 nm. The variations of band gaps from 0.299 eV to 0.279 eV were also observed for films of thickness in the range 50-200 nm. In the present study the obtained value of E_g is well in agreement with reported values of band gaps in the range of 1.58-2.20 eV for PbSe films of different thickness grown by chemical bath deposition technique [35].

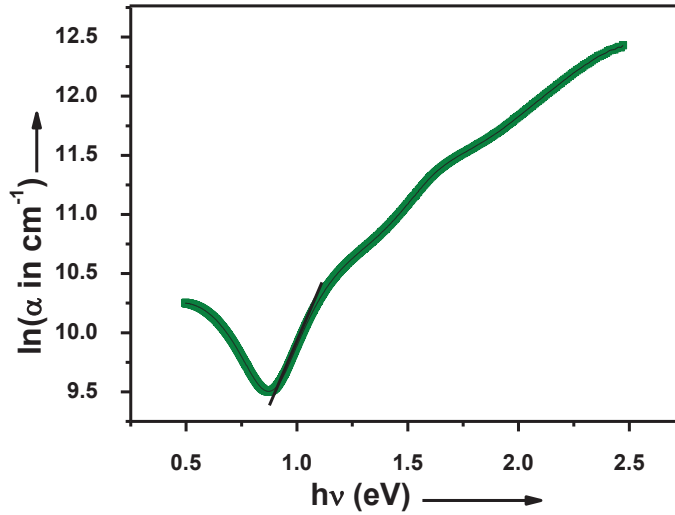


Fig. 4.8 Plot of $\ln(\alpha)$ against the photon energy for PbSe thin film

The weak absorption below the absorption band edge is observed and is found to follow Urbach tail rule [36]:

$$\alpha \propto \exp\left(\frac{E}{E_u}\right) \quad (4.2)$$

where E is the photon energy $h\nu$ and E_u is a constant or weakly dependent on temperature called Urbach energy which refers to the width of the exponential absorption edge. Tailing in the bandgap is related to disorder and imperfections, and it causes narrowing in the bandgap. The dependence of the optical absorption coefficient with photon energy may arise from trapping levels at grain boundaries.

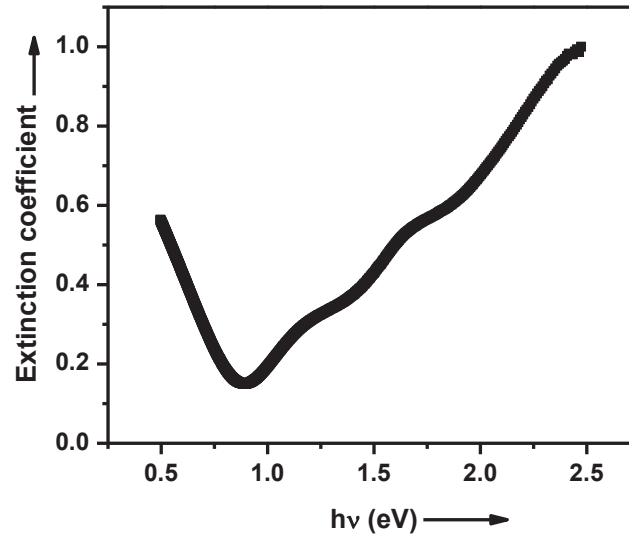


Fig. 4.9 Variation of extinction coefficient with photon energy

A plot of $\ln(\alpha)$ versus photon energy is performed and is shown in Figure 4.8. The width of the tail of the localised energy states estimated from the slope of the plot to be around 256 meV. The extinction coefficient (k) is related to the absorption coefficient (α) by the relation [36]

$$\alpha = \frac{4\pi k}{\lambda} \quad (4.3)$$

where λ is the wavelength of light that is used. In order to study the wavelength dependence of the extinction coefficient of the PbSe thin film, the variation of the extinction coefficient with photon energy is plotted and shown in Figure 4.9. It is found to vary from 0.1 to 1.0 with increase in photon energy.

The photoconductivity of the sample is studied at room temperature in order to understand the kinetics of the charge carriers. A typical PbSe film with dimensions 2.6 cm X 1.2 cm is used with silver paste as ohmic contact. The photoresponse of a typical PbSe film is shown in Figure 4.10. The photocurrent is found to increase with time since the free carriers are excited into the localized energy levels by absorbing the photons incident on the material and when the illumination is removed the current falls gradually with time. The slow decay is present in the sample since the decay curve is not linear and the slope of the curve goes on decreasing as the decay time is increasing indicates the non-exponential decay of the photoconductivity.

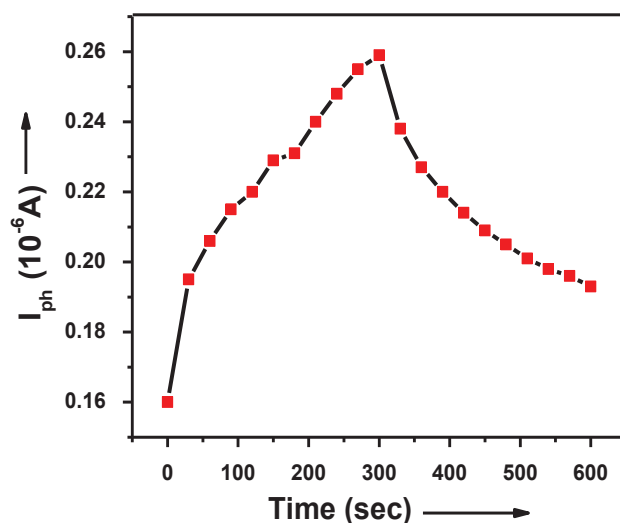


Fig. 4.10 The rise and decay of photocurrent in PbSe film at room temperature

For the non-exponential decay the differential life time can be calculated using Fuhs and Stuke relation [37].

$$\tau_d = - \left[\frac{1}{I_{ph}} \left(\frac{dI_{ph}}{dt} \right) \right]^{-1} \quad (4.4)$$

The differential life time versus time is plotted and is shown in Figure 4.11. It is found that the decay time is increasing with increasing time. This indicates that traps or localized states are present which arises from the structural imperfections or from impurities and it creates trapping sites for electrons above the Fermi level or hole trapping sites below the Fermi level in the material [38].

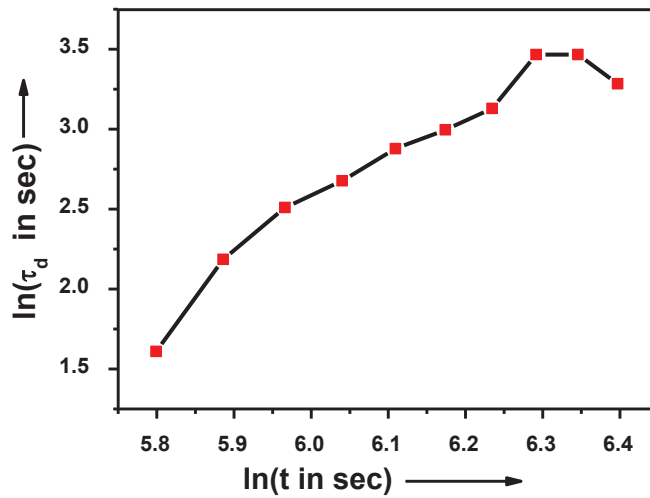


Fig. 4.11 The variation of differential life time with increasing decay time

Therefore when the illumination is cut off, before the disappearance of the carriers through recombination, they have been immobilised by various traps

present in the sample. Presence of these defects can lead to carriers in localized states near the band edge. This can be explained on the basis of grain boundary model including trapping states as proposed by Seto [39]. A polycrystalline material is composed of small crystallites joined together by grain boundaries. At the grain boundary the atoms are disordered which results a large number of defects. It can act as trapping centres. From the electrical conductivity measurement, it is found that acceptor-like levels are located at 0.063 eV near the valence band edge, may act as trapping centres. These trapping centres traps the carries and then the traps become electrically charged, creating a potential barrier which impedes the motion of carriers from one crystallite to another, thereby immobilising the carriers.

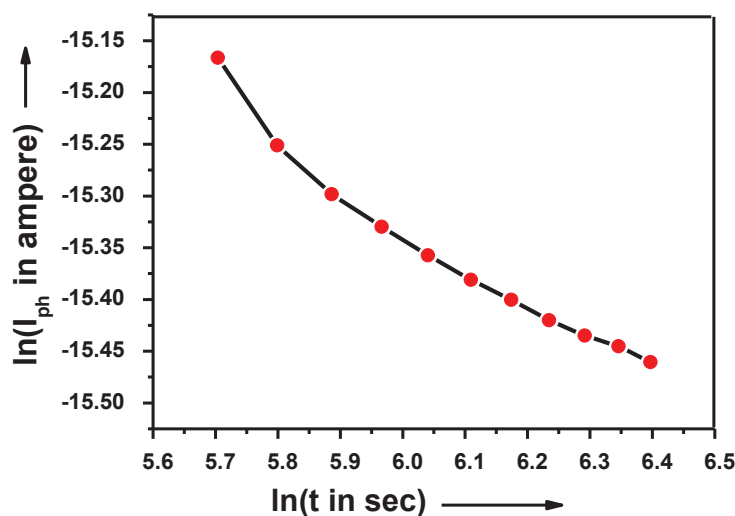


Fig. 4.12 The plot of $\ln(I_{ph})$ versus $\ln(t)$

The localised state energy distribution parameter E_l can be calculated using the relation [37]:

$$\beta = \frac{k_B T}{E_l} \quad (4.5)$$

where β is the dispersion parameter, k_B is the Boltzmann constant and T is the ambient temperature. The dispersion parameter β is calculated from the slope of $\ln(I_{ph})$ versus $\ln(t)$ graph and the plot is shown in Figure 4.12. The value of E_l obtained is 0.066 eV. The recombination centres usually lie deeper within the band gap as opposed to the trap states which lie closer to the band gap edge. The value of the localized energy distribution parameter, near to the band edge indicates the presence of traps in the material.

4.3.5 Low temperature TEP properties and Hall measurement

Table 4.3 Room temperature hall measurement results:

Carrier concentration n (cm^{-3})	Mobility μ ($\text{cm}^2\text{V}^{-1}\text{s}^{-1}$)	Hall coefficient R_H ($\text{cm}^3\text{C}^{-1}\text{V}^{-1}$)	Magnetoresistance (Ω)	Conductivity σ ($\Omega^{-1}\text{cm}^{-1}$)
8.75×10^{18}	18.67	0.71	2.31	26.16

PbSe compound exhibits a rock-salt structure with octahedral bonding and the space group $f\bar{m}\bar{3}m$. It is closely related to PbTe (tetrahedral bonding) in structure. Bond length in octahedral structures (PbSe = 0.6120 nm) is nearly as large as in tetrahedral structures (PbTe = 0.6480 nm) resulting in weaker bonding and lower thermal conductivity. Weak sp hybridisation in chemical bonding also leads to strong anharmonicity in the chemical bond. Therefore the

intrinsically low thermal conductivities of PbSe compounds come from the larger Grüneisen parameter ($\gamma = 1.65$) [40]. Hall measurements are carried out to know the room temperature conductivity and carrier concentration (table 4.3).

It is observed that films show p-type conductivity with optimized carrier concentration for thermoelectric applications. TEP is particularly useful in the studies of strongly disordered electronic systems exhibiting variety of electronic transport mechanisms including conduction or valence band states as well as impurity bands or hopping mechanism. The Seebeck coefficients (S) were evaluated for a typical lead selenide sample from the obtained data of thermal emf as a function of temperature and plotted in the temperature range 10-293 K as given in Figure 4.13. The positive values of S indicate that the conduction should occur predominantly due to holes which established the p-type conductivity of the lead selenide thin films. The thermoelectric power (S) of a semiconductor at low temperature consists of two components [41]: $S = S_d + S_p$ where S_d is the drift-diffusion contribution and S_p is the phonon-drag contribution. S_d is due to the normal tendency of the carriers to diffuse from cold to hot through the conductor when a steady temperature difference is maintained across the ends. S_p is produced by the drag on the carriers exerted by the phonons streaming from hot to cold in thermal conduction. The plot in figure 4.13 shows that thermoelectric power increases with temperature which is typical of a degenerate semiconductor. The temperature dependence of TEP results in our samples are almost consistent with the results of Gayner et.al. [42]. It may be considered that during TEP measurements the thermal

gradients established changes the density of charged defect state by capturing electrons and holes. The motion of electrons and holes can take place through the process of diffusion. In this case the density of the holes giving TEP is greater than that of electrons and the p-type nature established.

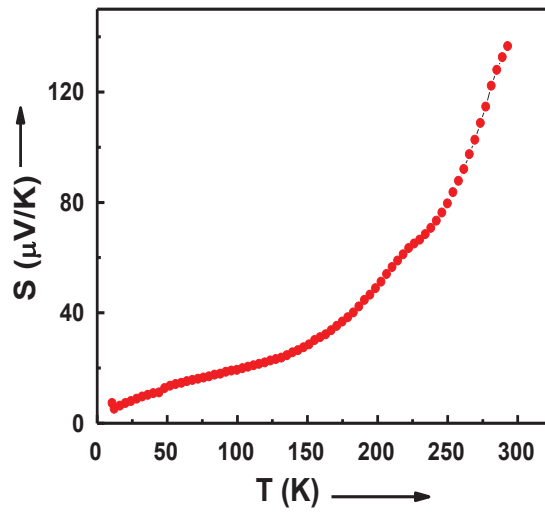


Fig. 4.13 Temperature variation of TEP for a typical PbSe thin film

For a p-type degenerated semiconductor thermoelectric power is given by [43]:

$$S = \frac{\pi^2 k_B^2 T}{3eE_F} \quad (4.6)$$

and

$$m^* = \frac{\hbar^2}{2E_F} \left(\frac{3n}{8\pi} \right)^{2/3} \quad (4.7)$$

Then

$$S = \frac{8\pi^2 k_B^2 T m^*}{3eh^2} \left(\frac{\pi}{3n} \right)^{2/3} \quad (4.8)$$

where E_F is the separation of the Fermi level from the top of the valence band or conduction band, e is the charge of the electron, m^* is the effective mass, n

is the carrier concentration, h Planck's constant, T is the temperature and k_B is the Boltzmann's constant.

Table 4.4 The semiconductor properties of PbSe film at Fermi level

Fermi level E_F (eV)	Effective mass m^*	Density of states N (cm ⁻³)	Relaxation time τ (s)	Fermi velocity v_F (m s ⁻¹)	Mean free path l (nm)
~ 0.054	~ 0.29 m_0	~ 3.88 × 10 ¹⁸	~ 3.1 × 10 ⁻¹⁵	0.256 × 10 ⁶	~ 0.79

At first, we calculated the Fermi levels from the experimental Seebeck coefficient data using eq. 4.6. Then, the hole effective mass (eq. 4.7) is determined using the calculated Fermi energies and the experimental Hall carrier-concentration values. The transport properties of the PbSe thin film at the Fermi level are calculated and tabulated (table 4.4). The Seebeck coefficient of the PbSe thin film reaches a maximum of about 137 μVK^{-1} at 293 K. The closeness of Fermi level (0.054 eV) to the valence band edge leads enhancement of TEP near room temperature, is found to be almost comparable to that reported in pristine p-type PbSe [42]. At a carrier concentration of $8.75 \times 10^{18} \text{ cm}^{-3}$, the effective mass obtained is $0.29 m_0$, whereas for p-type PbSe $0.17 m_0$ has been reported [42]. The thermoelectric power factor ($S^2\sigma$), which represents the electrical contribution to the thermoelectric performance is calculated at room temperature with measured result of electrical conductivity and it is obtained as $12 \times 10^{-4} \text{ Wcm}^{-1}\text{K}^{-2}$. The power factor obtained here is comparable to the commercially used Bi_2Te_3 [44]. The intrinsically low thermal conductivity together with the obtained

power factor of the PbSe film and the rapid increase of Seebeck coefficient with temperature can be exploited in the room temperature thermoelectric applications including small-scale electronic and opto-electronic devices.

4.4 Conclusion

Using Gunther's technique, good quality p-type thermoelectric PbSe films are prepared on glass substrates and the preparative parameters like the substrate temperature, as well as incident fluxes of lead and selenium are optimized. XRD and AFM show these films are polycrystalline in nature. The various structural parameters such as particle size, number of crystallites per unit area and strain are estimated. The SEM image confirms the growth of randomly oriented grains which are uniformly distributed over the substrate surface. The film shows an electrical conductivity of $26.16 \Omega^{-1}\text{cm}^{-1}$ with thermal activation energy of 0.063 eV. The lead selenide thin films have high optical absorption coefficient. The material possesses a direct allowed optical band gap of 2.02 eV and the absorption coefficient is found to be in the range 10^4 cm^{-1} to 10^5 cm^{-1} . The Urbach tail width is estimated and is around 0.256 eV. The rise and decay of the photocurrent at room temperature which gives an insight into the localized energy states in the band gap of the material. The differential life time measurements reveal the presence of defect levels in the energy gap of the material. The localised state energy distribution parameter E_0 is obtained as 0.066 eV, it is well nearer to the band edge indicates the presence of trapping states. The low temperature thermoelectric power measurements show that TEP has positive values, consistent with effective hole type carriers. The Fermi energy is estimated as 0.054 eV. The

maximum Seebeck coefficient obtained is about $137 \mu\text{VK}^{-1}$ at 293K. The power factor of the p-type PbSe film is found to be $12 \times 10^{-4} \text{ Wcm}^{-1}\text{K}^{-2}$ with optimised carrier concentration of $8.75 \times 10^{18} \text{ cm}^{-3}$. The preparation method and the results obtained in this study may be useful as a guideline for the future study of the potential applications of p-type PbSe thin film in thermoelectric devices.

References

- [1] P. P. Hankare, S. D. Delekar, V. M. Bhuse, K. M. Garadkar, S. D. Sabane, and L. V Gavali, "Synthesis and characterization of chemically deposited lead selenide thin films," *J. Mater. chem. and Phys.* vol. 82, pp. 505–508, 2003.
- [2] M. T. Rodrigo, F. J. Sanchez, M. C. Torquemada, V. Villamayor, G. Vergara, G. M. Verdu, L. J. Gomez, J. Diezhandino, R. Almazan, P. Rodriguez, J. Plaz, I. Catalan and M. T. Montojo, "Polycrystalline lead selenide x-y addressed uncooled focal plane arrays," *Infrared Phys. Technol.*, vol. 44, pp. 281–287, 2003.
- [3] V. Arivazhagan, M. Manonmani Parvathi, and S. Rajesh, "Impact of thickness on vacuum deposited PbSe thin films," *Vacuum*, vol. 82, pp. 1092-1096, 2012.
- [4] I. A. Ezenwa, "Optical Properties of Chemical Bath Deposited Lead Selenide Thin Films," *Advances in Appl. Sci. Research*, vol. 3, no. 2, pp. 980–985, 2012.
- [5] A. N. Molin and A. I. Dikumar, "Electrochemical deposition of PbSe thin films from aqueous solutions," *Thin Solid Films*, vol. 265, pp. 3–9, 1995.
- [6] Heini Saloniemi, Tapio Kanninen, Mikko Ritala, Markku Leskela,

- Reijo Lappalainen, "Electrodeposition of lead selenide thin films," *J. of Mater. Chem.*, vol. 8, no. 3, pp. 651–654, 1998.
- [7] Swapan K. Datta and A. K. Chaudhuri, "On the mechanism of photoconductivity in polycrystalline lead selenide films," *Semiconducting Sci. Technol.*, vol. 4, pp. 376–381, 1989.
- [8] S. Prabakar, N. Suryanarayanan, K. Rajasekar, and S. Srikanth, "Compositional and electrical resistivity studies on thermal evaporation lead selenide thin films," *Chalcogenide letters*, vol. 6, no. 6, pp. 227–232, 2009.
- [9] B. Wagner, N. B. Singh, S. McLaughlin, A. Berghmans, D. Kahler and D. Knuteson, "Effect of growth parameters on the morphology and resistivity of PbSe," *J. Cryst. Growth*, vol. 311, no. 4, pp. 1080–1086, 2009.
- [10] R. B. Kale, S. D. Sartal, V. Ganesan, C. D. Lokhande, Yi-Feng Lin and Shih-Yuan Lu "Room temperature chemical synthesis of lead selenide thin films with preferred orientation," *Appl. Surf. Sci.*, vol. 253, pp. 930–936, 2006.
- [11] E. Barrios-Salgado, M. T. S. Nair, P. K. Nair, and R. A. Zingaro, "Chemically deposited thin films of PbSe as an absorber component in solar cell structures," *Thin Solid Films*, vol. 519, no. 21, pp. 7432–7437, 2011.
- [12] I. Grozdanov, M. Najdoski and S. K. Dey "A simple solution growth technique for PbSe thin films," *Mater. s Lett.*, vol. 38, pp. 28–32, 1999.
- [13] S. Sagadevan, J. Podder, and I. Das, "Structural , morphological , optical and electrical properties of PbSe thin films grown by chemical bath deposition," *Adv. Mater. Lett.*, vol. 7, no. 5, pp. 410–413, 2016.

- [14] V. V. Tetyorkin, A. Yu. Sipatov, A. I. Fedorenko and A. Fedorov, “(001) -oriented lead selenide films grown on silicon substrates,” *Infrared Physics & Technol.*, vol. 37, pp. 379–384, 1996.
- [15] R. T. Rumianowski, R. S. Dygdala, W. Jung, and W. Bala, “Growth of PbSe thin films on Si substrates by pulsed laser deposition method,” *J. Cryst. Growth*, vol. 252, pp. 230–235, 2003.
- [16] K. Anuar, H. A. Abdul, S. M. Ho and N. Saravanan, “Effect of Deposition Time on Surface Topography of Chemical Bath Deposited PbSe Thin Films Observed by Atomic Force Microscopy ,” *Pacific J. Sci. Technol.*, vol. 11, no. 1, pp. 399–403, 2010.
- [17] J. R. Sootsman, D. Y. Chung, and M. G. Kanatzidis, “New and Old Concepts in Thermoelectric Materials,” *Angewandte Chemie International Edition*, vol. 48, pp. 8616–8639, 2009.
- [18] T. M. Tritt and M. A. Subramanian, “Thermoelectric Materials, Phenomena, and Applications: A Bird’s Eye View,” *MRS Bull.*, vol. 31, pp. 188–198, 2006.
- [19] X. F. Zheng, C. X. Liu, Y. Y. Yan, and Q. Wang, “A review of thermoelectrics research – Recent developments and potentials for sustainable and renewable energy applications,” *Renew. Sustain. Energy Rev.*, vol. 32, pp. 486–503, 2014.
- [20] H. Zou, D. M. Rowe, and G. Min, “Growth of p-and n-type bismuth telluride thin films by co-evaporation,” *J. Cryst. Growth*, vol. 222, pp. 82–87, 2001.
- [21] L. M. Goncalves, C. Couto, P. Alpuim, D. M. Rowe, and J. H. Correia, “Thermoelectric Properties of Bi₂Te₃ / Sb₂Te₃ Thin Films,” *Mater. Sci. Forum*, vol. 514–516, no. May, pp. 156–160, 2006.

- [22] M. Kang, J. Jung, S. Lee, J. Ryu, and S. Won, "Conductivity, carrier density, mobility, Seebeck coefficient, and power factor in V_2O_5 ," *Thermochim. Acta*, vol. 576, pp. 71–74, 2014.
- [23] B. Fang, Z. Zeng, and X. Yan, "Effects of annealing on thermoelectric properties of Sb_2Te_3 thin films prepared by radio frequency magnetron sputtering," *J. Mater. Sci. Mater. Electron.*, vol. 24, pp. 1105–1111, 2013.
- [24] S. V. Ovsyannikov and V. V Shchennikov, "High-Pressure Routes in the Thermoelectricity or How One Can Improve a Performance of Thermoelectrics ," *Chem. Mater. Rev.*, vol. 22, pp. 635–647, 2010.
- [25] V. D. Das and K. S. Bhat, "Electrical conductivity of air-exposed and unexposed lead selenide thin films: Temperature and size effects," *Phys. Rev. B*, vol. 40, no. 11, pp. 7696-7703, 1989.
- [26] P. K. Kalita, "Structural and Optical Properties of Chemically Synthesised PbSe Nanorods," *Res. J. Mater. Sci.*, vol. 1, no. 1, pp. 26–30, 2013.
- [27] K. S. Urmila, Namitha Asokan T., Rachel Reena Philip and B. Pradeep, "Optical and low-temperature thermoelectric properties of phase-pure p-type InSe thin films," *Appl. Phys. A*, vol. 120, no. 2, pp. 675–681, 2015.
- [28] S. Tolansky, *Multiple Beam Interferometry of Surfaces and films*. Oxford University Press, London, 1948.
- [29] A. Soni and G. S. Okram, "Resistivity and thermopower measurement setups in the temperature range of 5 – 325 K," *Rev. Sci. Instrum.*, vol. 79, pp. 125103 1–4, 2008.
- [30] *Powder Diffraction file, International Centre for Diffraction Data (ICDD) Card No: 78-1903.*

- [31] B. D. Cullity, *Elements of x-ray diffraction*. Addison-Wesley publishing company Inc, USA, 1956.
- [32] Namitha Asokan T., K. S. Urmila, R. Jacob, R. R. Philip, G. S. Okram, V. Ganesan and B. Pradeep, “Optical and electrical properties and phonon drag effect in low temperature TEP measurements of AgSbSe₂ thin films,” *J. Semiconductors*, vol. 32, pp. 052001 1-6, 2014.
- [33] J. Tauc, “Optical properties and electronic structure of amorphous Ge and Si,” *Mater. Res. Bull.* vol. 3, pp. 37–46, 1968.
- [34] S. Prabhakar, N. Suryanarayanan, R. Rajaseka and S. Sreekanth, “Lead selenide thin films from vacuum evaporation method- Structural and optical properties,” *Chalcogenide Lett.*, vol. 6, pp. 203–211, 2009.
- [35] I. Smu and M. N. Nnabuchi, “The optical and solid state properties of lead selenide (PbSe) thin films grown by chemical bath deposition (CBD) technique,” *J. Ovonic Res.*, vol. 6, no. 2, pp. 81 – 86, 2010.
- [36] M. A. Majeed Khan, S. Kumar, M. Alhoshan, and A. S. Al Dwayyan, “Spray pyrolysed Cu₂ZnSnS₄ absorbing layer: A potential candidate for photovoltaic applications,” *Opt. Laser Technol.*, vol. 49, pp. 196–201, 2013.
- [37] N. Chaudhary, A. A. Bahishti, and M. Zulfequar, “Photoconductivity of Se_{85-x}Te₁₅Hg_x thin films,” *Physica B*, vol. 407, no. 12, pp. 2267–2271, 2012.
- [38] B. G. Streetman, “Carrier recombination and trapping effects in transient photoconductive decay measurements,” *J. Appl. Phys.*, vol. 37, no. 8, pp. 3137–3144, 1966.
- [39] John Y. W. Seto, “The electrical properties of polycrystalline silicon films,” *J. Appl. Phys.*, vol. 46, no. 1975, pp. 5247–5254, 1975.

- [40] H. Wang, Y. Pei, A. D. LaLonde and G. J. Snyder, "Heavily Doped p-Type PbSe with High Thermoelectric Performance: An Alternative for PbTe," *Advanced Mater.*, vol. 23, pp. 1366–1370, 2011.
- [41] C. Herring, "Theory of the Thermoelectric Power of Semiconductors," *Phys. Rev.*, vol. 96, pp. 1163–1187, 1954.
- [42] C. Gayner, R. Sharma, M. K. Das, and K. K. Kar, "Boost in room temperature thermoelectric performance of PbSe:Al_x through band modification and low densification," *J. Appl. Phys.*, vol. 120, pp. 155106 1-11, 2016.
- [43] X. Zhang and Li-Dong Zhao, "Thermoelectric materials: Energy conversion between heat and electricity," *J. Materiomics*, vol. 1, pp. 92–105, 2015.
- [44] J. Lin, Y. Chen, and C. Lin, "Annealing Effect on the Thermoelectric Properties of Bi₂Te₃ Thin Films Prepared by Thermal Evaporation Method," *J. Nanomater.*, vol. 2013, pp. 201017 1–6, 2013.

Chapter 5

Reactively evaporated p-type lead antimony selenide thin films and its characterization

5.1 Introduction

5.2 Experimental details

5.3 Results and discussions

5.4 Conclusion

5.1 Introduction

Enhancing the utilization of full spectrum solar energy, in order to mitigate the global energy crisis, through the optimal hybridization of photovoltaic (PV) and thermoelectric (TE) devices is in demand because solar energy is readily available and most stable, in contrast to wind, water and pressure [1]. Recently, a large number of studies have focused on the development of thermoelectric modules which convert heat into electricity. These devices are silent, reliable and scalable rather than their efficiency, making them ideal for small, distributed power generation and refrigeration applications. The efficiency of thermoelectric material is given by the dimensionless figure of merit $ZT = \frac{S^2\sigma T}{\mathcal{K}}$ or power factor $P = S^2\sigma$ where ‘S’ is the Seebeck coefficient, σ is the electrical conductivity and \mathcal{K} is the thermal conductivity. The figure of merit can be increased by maximizing the power

factor through and/or minimizing the thermal conductivity. The maximization of the power factor can be achieved through the development of new materials, optimization of existing materials by doping, and the exploration of nanoscale materials. The thermal conductivity can be minimized by alloying and/or nanostructuring [2]. Initially the materials used for commercial applications include bulk Bi_2Te_3 , PbTe , SiGe system [3]. Some of the recently developed materials under investigation include skutterudites [4]–[6], clathrates [7]–[10], half-Heusler alloys [11][12][13], complex chalcogenides [14]–[17], complex oxide materials [18], thin film superlattice structures [19] and nano structured materials [20]–[23]. The current tendency to miniaturisation has provoked interest in thin film thermoelectric devices to enhance thermoelectric performance because (i) films have lower thermal conductivity than those of bulk materials due to strong phonons scattering at surfaces and film-surface interface and (ii) density of states near the Fermi energy is enhanced, giving rise to increased Seebeck coefficient [24][25].

Although solar cell devices have been used for various applications, the low efficiency and high price of solar cell materials have limited their widespread application. Chalcogenide compounds have had a prominent position in the field of photovoltaic since most of the compounds are environmentally stable, high melting points and have energy gaps appropriate for photovoltaic applications over a wide range of temperatures. Polycrystalline thin films of copper indium sulphide (CuInS_2), copper gallium sulphide (CuGaS_2), copper indium gallium diselenide (Cu(In,Ga)Se_2), copper gallium indium sulfide (CuGaInS_2), cadmium telluride (CdTe), cadmium

sulphide (CdS), indium diselenide (InSe₂) and copper indium aluminum diselenide (CIAS) are the chalcogenide materials that have been extensively studied and these materials display good electrical and optical properties suitable for photovoltaic devices [26]. Thus, the key issue of micro-electronic devices is the fabrication of new and novel semiconducting thin films with high opto-electronic and thermoelectric properties for small-scale solar energy conversion applications.

In this study nano-structured p-type Pb_{3.58}Sb_{4.42}Se₁₀ are reactively evaporated and their structural, optical and transient photoconductivity properties are evaluated. Interest in extending the temperature range of operation above that of the commercially used TE materials, the Seebeck coefficient of Pb_{3.58}Sb_{4.42}Se₁₀ thin films are studied over 11–300 K.

5.2 Experimental details

The p-type lead antimony selenide thin films were prepared by reactive evaporation technique on to ultrasonically cleaned glass substrates kept at 448±5K. The need to synthesize the compound from the elements prior to deposition which is a tedious and sometimes expensive metallurgical process is eliminated in this technique. Moreover, the decomposition of the compound upon heating in vacuum due to large differences in the vapor pressure of lead, antimony and selenium and consequent lack of stoichiometry in the films are avoided. In this work, the high purity (99.999%) lead, antimony and selenium were used as evaporates. Antimony and selenium were evaporated from two separate glass crucibles kept in molybdenum baskets and lead from a molybdenum boat. The source materials were heated with current at vacuum

$\sim 10^{-5}$ torr and deposited on glass substrates. The optimized parameters used for the preparation of the samples in present work are given below.

Table 5.1 Deposition parameters:

Impingement rate of lead	$\approx 1.13 \times 10^{15} \text{ atoms cm}^{-2} \text{ s}^{-1}$
Impingement rate of antimony	$\approx 2 \times 10^{15} \text{ atoms cm}^{-2} \text{ s}^{-1}$
Impingement rate of selenium	$\approx 6 \times 10^{14} \text{ atoms cm}^{-2} \text{ s}^{-1}$
Substrate temperature	$= 448 \pm 5 \text{ K}$

The films of thickness of about 600 nm were prepared and it was measured using stylus profiler (Dektak 6M stylus profiler). The XRD measurements were done using Rigaku D MaxC X-Ray Diffractometer with Cu-K α radiation. SEM (JEOL Model JSM-6390 LV) and AFM (AFM nanoscope E, Digital Instruments) were used to determine the morphology and microstructure of the film. XPS measurements were performed with XPS - VSW Scientific Instruments photoelectron spectrometer using monochromatic Al-K α radiation (1486.6 eV). The optical transmittance spectra of the films were recorded on a JASCO V-570 UV-Vis-NIR spectrophotometer. The dark conductivity and photoconductivity of the films was recorded using a Keithley 2611A source meter, a bias voltage of 10 V was applied and current was recorded in the dark for 150 s and under illumination (FSH lamp of 82 V, 300 W) for another 300 s. The Seebeck coefficient of the film was measured in the temperature range of 11–300 K. The Hall measurement is carried out by using ECOPIA HMS-3000 system.

5.3 Results and discussions

5.3.1 Structural analysis

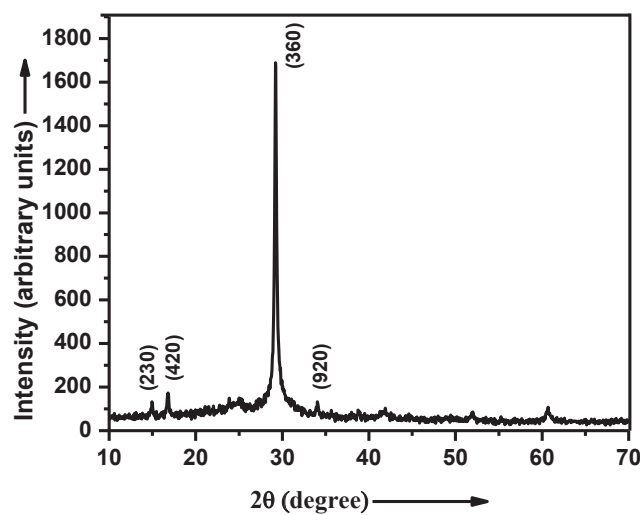


Fig. 5.1 X-ray diffraction pattern of a typical $\text{Pb}_{3.58}\text{Sb}_{4.42}\text{Se}_{10}$ sample

The X-ray diffraction pattern in figure 5.1 reveals the polycrystalline nature of $\text{Pb}_{3.58}\text{Sb}_{4.42}\text{Se}_{10}$ thin film. All peaks are indexed as per ICDD file no: 80-0654 (table 5.2). But the 100% peak in the standard pattern is absent in the as prepared film. This may be due to the orientation of the (521) plane perpendicular to the film surface. The peak corresponds to an orthorhombic structure with lattice parameters $a = 24.77\text{\AA}$, $b = 20.25\text{\AA}$, $c = 4.12\text{\AA}$ and molecular weight = 2069.51 which are consistent with the ICDD file no: 80-0654 [27]. The values of particle size, dislocation density, number of crystallites per unit area and strain calculated are tabulated (table 5.3) [28].

Table 5.2 The observed XRD data along with standard ICDD data

Standard pattern(ICDD Card No: 80-0654)			As prepared film	
(hkl)	d(Å)	I/I ₀	d(Å)	I/I ₀
230	5.8053	2	5.9272	8
420	5.2195	1	5.2787	10
360	3.0555	24	3.05901	100
521	3.0260	100	-	-
920	2.6334	1	2.63357	8

Table 5.3 Microstructural parameters:

Average particle size D (nm)	~ 25
Dislocation density ρ (lines m^{-2})	$\sim 1.6 \times 10^{15}$
Number of crystallite per unit area N (m^{-2})	$\sim 3.84 \times 10^{14}$
Strain T	$\sim 2.267 \times 10^{-3}$

5.3.2 Morphological and compositional analysis

Figure 5.2 shows the SEM image of a typical $Pb_{3.58}Sb_{4.42}Se_{10}$ thin film with 5,000 magnifications. It is observed that the film is composed of minute grains without cracks or pinholes and it well covers the glass substrate. The EDS spectra of the thin films as depicted in figure 5.3 show that the sample consists of lead, antimony and selenium.

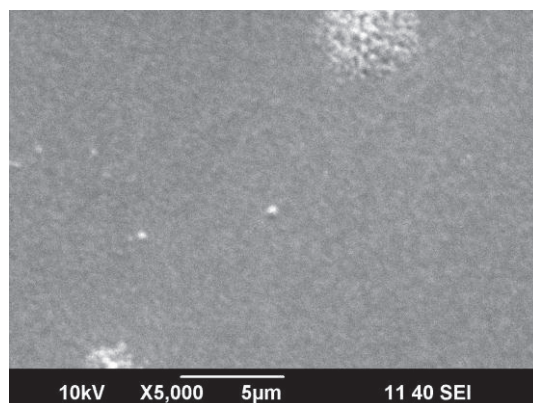


Fig. 5.2 Surface Morphology of lead antimony selenide thin film

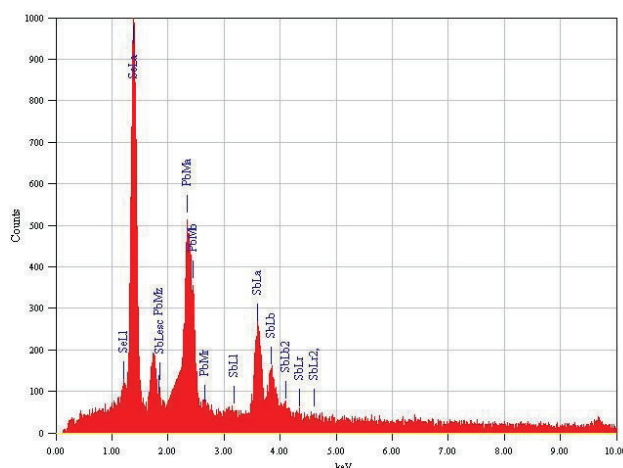


Fig. 5.3 EDAX spectra of a typical lead antimony selenide thin film

Figure 5.4(a), 5.4(b), and 5.4(c) show the X-ray photoelectron spectra of Pb 4f, Sb 3d and Se 3d for a typical $\text{Pb}_{3.58}\text{Sb}_{4.42}\text{Se}_{10}$ thin film. As can be observed, the Pb 4f_{7/2} and 4f_{5/2} peaks shown in Figure 4(a) are centered at about 137.03eV and 142.07 eV. The presence of peaks is attributed to the possible presence of lead in $\text{Pb}_{3.58}\text{Sb}_{4.42}\text{Se}_{10}$ film. The binding energies of Sb 3d_{3/2} and Sb 3d_{5/2} peaks (Figure 4(b)) are observed at about 540.1 eV and

530.82 eV respectively. The Se 3d_{5/2} peak is shown in Figure 4(c) with binding energies of about 53.29 eV. Compositional analysis gives result as 20% of Pb, 35% of Sb and 45% of Se which confirms the films are nearly stoichiometric. The above results confirm the formation of Pb_{3.58}Sb_{4.42}Se₁₀ film.

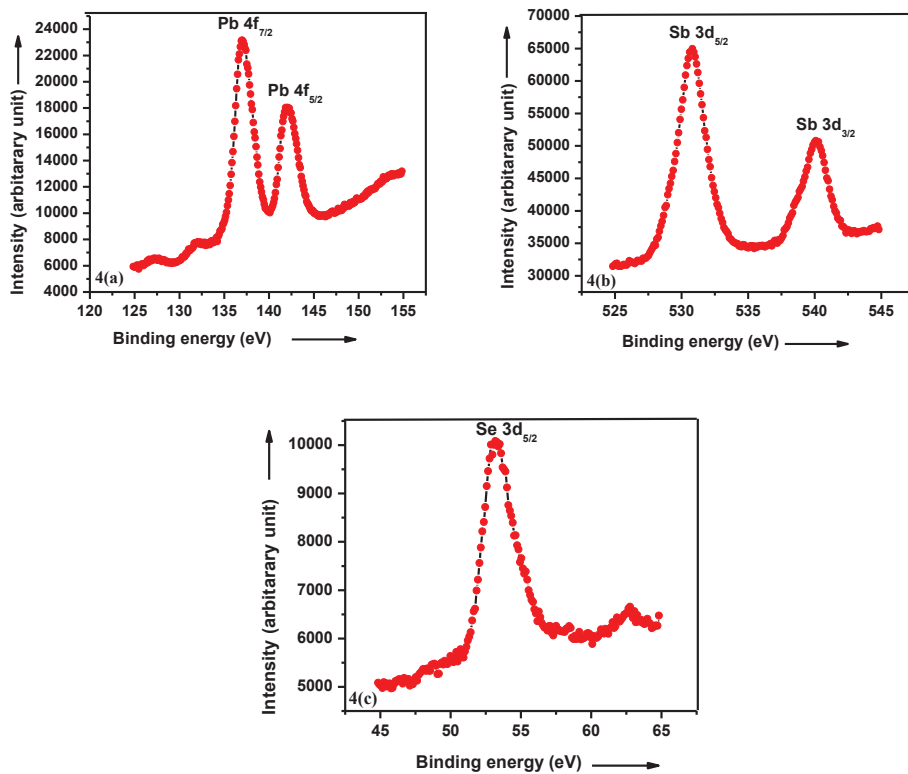


Fig. 5.4 XPS spectra for Pb_{3.58}Sb_{4.42}Se₁₀ film on glass substrate

Figures 5.5(a) and 5.5(b) represent the two-dimensional (2D) and three-dimensional (3D) typical AFM images of the thin film. It can be seen from Fig. 5(a) that the film exhibited closely packed well defined grains of sizes 60 to 90 nm in diameter, confirming the nanocrystalline structures for the films. The

surface of the as-prepared thin film is almost smooth with root mean square (RMS) value of surface roughness determined from 3D image is 5 nm.

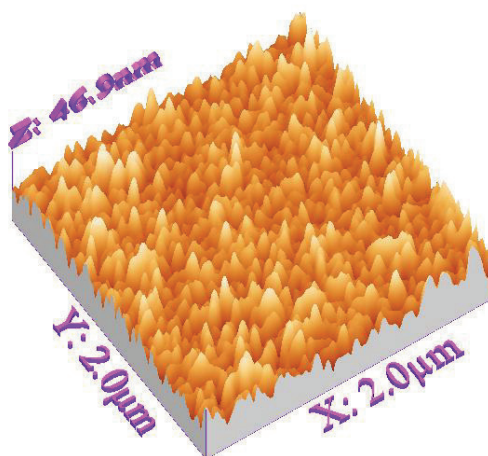
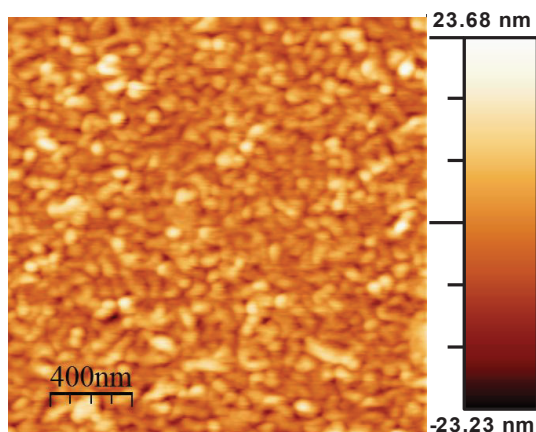


Fig. 5.5(a) The two dimensional AFM topography image of $\text{Pb}_{3.58}\text{Sb}_{4.42}\text{Se}_{10}$ thin film (area $2 \times 2 \mu\text{m}$) and (b) the three dimensional AFM topography image of $\text{Pb}_{3.58}\text{Sb}_{4.42}\text{Se}_{10}$ thin film (area $2 \times 2 \mu\text{m}$)

5.3.3 Optical analysis

The envelope method suggested by Swanepoel is used for extracting the optical parameters of the film. The refractive index is calculated in weak and medium absorption region and is extrapolated in strong absorption region by the Cauchy's equation [29][30][31]. From the interference fringe pattern of the transmittance spectra as depicted in figure 5.7(b), the extracted values of refractive index $n(\lambda)$ and the accompanying Cauchy's fit with photon energy are shown in figure 5.6(a). With increasing of energy, the refractive index of a typical film is increased from 5.07 to 6.43.

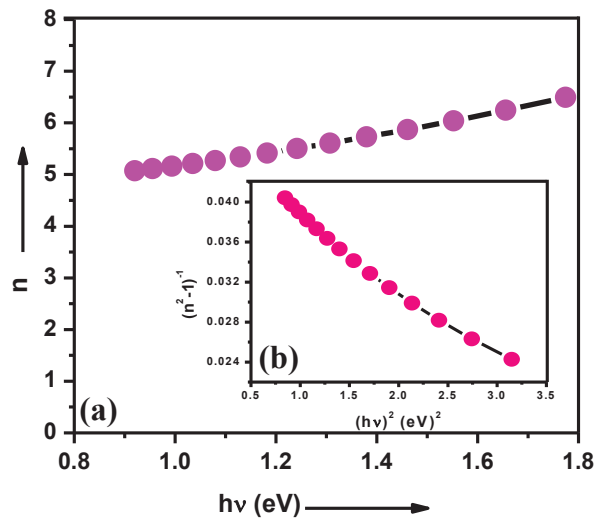


Fig. 5.6 Plots of (a) refractive index dispersion spectra of a typical sample with photon energy and (b) refractive index factor versus $(h\nu)^2$.

If n_1 and n_2 are the refractive indices calculated from two consecutive maxima or minima corresponds to two wavelengths of λ_1 and λ_2 , then the thickness of the film t can be obtained as [32]

$$t = \frac{\lambda_1 \lambda_2}{2(\lambda_1 n_2 - \lambda_2 n_1)} \quad (5.1)$$

The thickness obtained is about 600 nm and is well agreement with that obtained from the Stylus profiler. The absorption coefficient (α) obtained in the strong absorption region is found to be larger than 10^4 cm^{-1} , which is very promising for photovoltaic application.

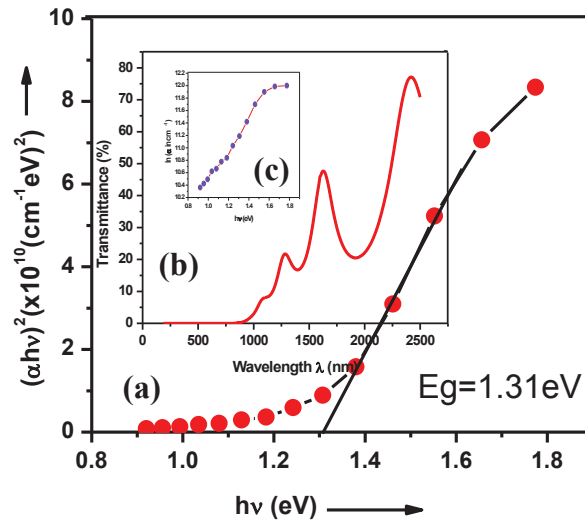


Fig. 5.7 Plot of (a) the dependence of $(\alpha h\nu)^2$ on photon energy for a typical $\text{Pb}_{3.58}\text{Sb}_{4.42}\text{Se}_{10}$ sample, (b) Typical transmission spectra and (c) Absorption in a sample

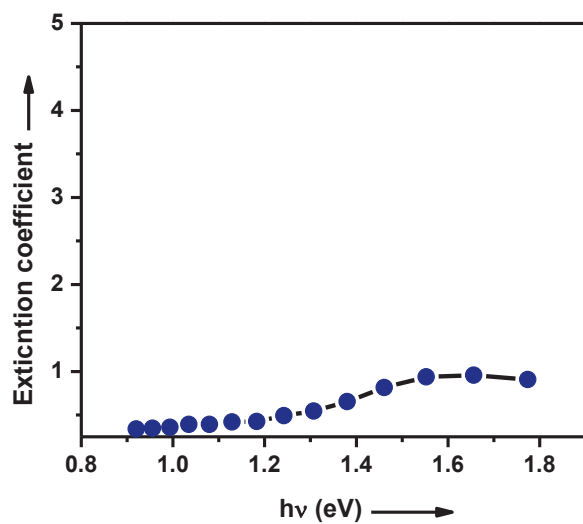
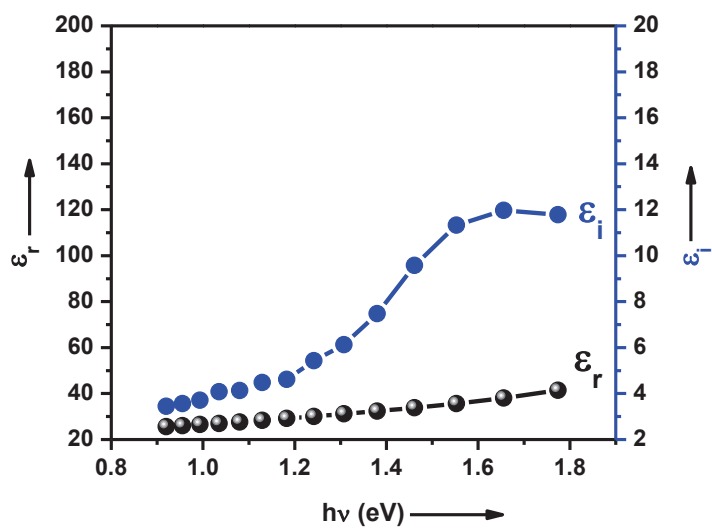
From absorption coefficient of the thin film in high absorption ($\alpha \geq 10^4 \text{ cm}^{-1}$) region, $(\alpha h\nu)^2$ versus photon energy is plotted according to Tauc's

relation and is shown in figure 5.7(a). A linear region over a wide range of photon energy is found in the plot of $(\alpha h\nu)^2$ versus $h\nu$, indicating that the dominant transition type is direct allowed. The value optical band gap is 1.31 eV. From the plot of the natural logarithm of the absorption coefficient against the photon energy as depicted in figure 5.7(c), it is found that this tailing follows Urbach rule. The width of the tail is estimated and found to be 0.5 eV, indicates the presence of structural disorder in the polycrystalline sample.

The refractive index (n) dispersion of the film can be analyzed in terms of the single oscillator model proposed by the Wemple and DiDomenico (WDD)[33][34] as

$$n^2 - 1 = \frac{E_0 E_d}{E_0^2 - (h\nu)^2} \quad (5.2)$$

where E_0 is the single-oscillator energy and E_d is the dispersion energy. By plotting refractive index factor $(n^2 - 1)^{-1}$ versus $(h\nu)^2$ near the absorption edge and fitting the data to a straight line (Fig. 5.6(b)), the obtained values of WDD parameters E_0 and E_d for a typical sample are 2.65 eV and 61.35 eV. As was proposed by Tanaka [35], the approximate value of the optical band gap E_g , is also derived from WDD model, according to the expression $E_g \approx \frac{E_0}{2}$. The value obtained is almost in agreement with that from the Tauc's extrapolation model. The extinction coefficient (k) value as depicted in figure 5.8 increases with increase in the photon energy and it varies from 0.34 to 0.91. The real part (ϵ_r) and imaginary part (ϵ_i) of the complex dielectric constant of the prepared film are also calculated [36] and their dependence on photon energy is presented in Fig. 5.9.

Fig. 5.8 Variation in k with photon energyFig. 5.9 Variation in ϵ_r and ϵ_i with photon energy

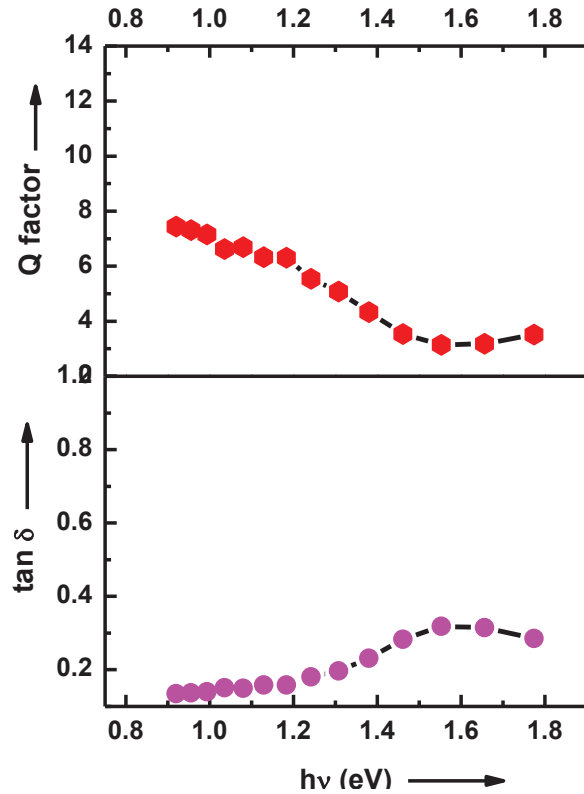


Fig. 5.10 Variation in $\tan \delta$ and Q factor with photon energy

Figure 5.10 shows dissipation factor ($\tan \delta$) and Q factor of the films as a function of photon energy. The $\tan \delta$ is the energy dissipation in the dielectric system, which is proportional to the imaginary part of the dielectric constant. At lower photon energy $\tan \delta$ is low and it increases with increasing energy.

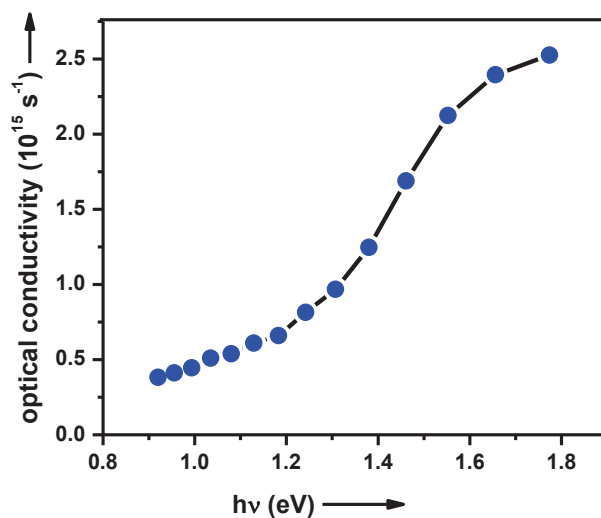


Fig. 5.11 The optical conductivity against photon energy for the $\text{Pb}_{3.58}\text{Sb}_{4.42}\text{Se}_{10}$ thin film sample

The optical conductivity (σ_{opt}) of the film is obtained [32] by

$$\sigma_{opt} = \frac{\alpha n c}{4\pi} \quad (5.3)$$

where α is the absorption coefficient, n is the refractive index and c is the velocity of light. The variation of optical conductivity for a $\text{Pb}_{3.58}\text{Sb}_{4.42}\text{Se}_{10}$ thin film is shown in figure 5.11 as a function of photon energy. It is found that σ increases with increase in photon energy. The high magnitude of optical conductivity ($>10^{14} \text{ s}^{-1}$) and the low extinction coefficient (<1) confirms the presence of very high photo response nature of the material. Experimental results of time dependent transient photoconductivity measurements of a typical sample are reported in figure 5.12. It is clear from this figure that there is an increase in the conductivity of the sample under illumination. After

turning off the light, the photocurrent first decreases rapidly and then decreases much more slowly. Even after decaying for 350 s, the photocurrent does not go to zero. The present photoconductivity rise and decay with time indicate that the photoconductivity behavior may be best understood in terms of deep traps within localized states

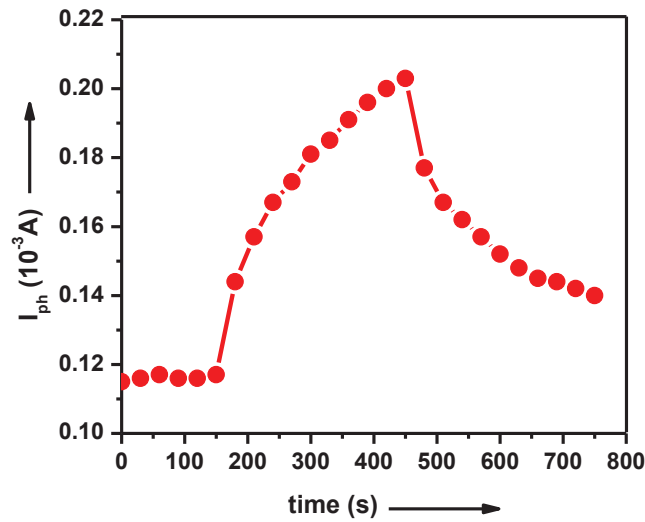


Fig. 5.12 The rise and decay of photocurrent in $Pb_{3.58}Sb_{4.42}Se_{10}$ film at room temperature.

For the analysis of decay rates in non-exponential decay the differential lifetime is calculated using the Fuhs and Stuke relation [37]. The increase in differential life time with time shown in figure 5.13 illustrates that the decay is non-exponential in nature. Therefore the slow decay may be ascribed due to deep traps that exist at all the energies in the band gap.

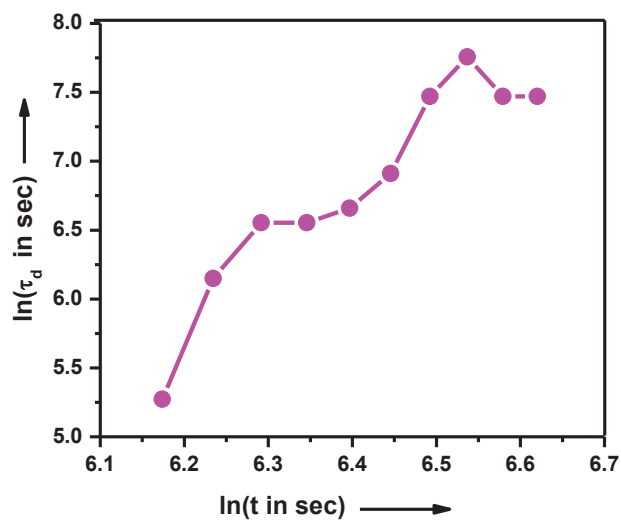
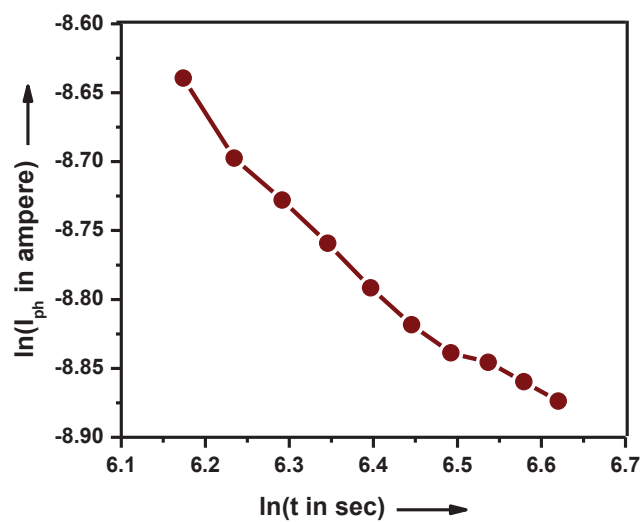


Fig. 5.13 The variation of differential life time

Fig. 5.14 The plot of $\ln(I_{ph})$ versus $\ln(t)$

The dispersion parameter (β) is calculated from the slope of $\ln(I_{ph})$ versus $\ln(t)$ (figure 5.14) and using the value of β , the localized state distribution parameter E_l is also calculated. The value of E_l obtained is 0.0508 eV which gives the position of trap states in the band gap of the material. Unfortunately, we could not find any article that calculates the above reported parameters for $Pb_{3.58}Sb_{4.42}Se_{10}$ thin film. Hence, the values reported here could not be compared with others. The results show that the reactively evaporated $Pb_{3.58}Sb_{4.42}Se_{10}$ thin films which display good electrical and optical properties, making it highly suitable for optoelectronic applications.

5.3.4 Low temperature TEP properties and Hall measurement

The van der Pauw technique in a magnetic field of 0.55 T was used to obtain hall measurement (table 5.3). The hot probe method was used to check the type of conductivity of the samples, the films showed p-type conductivity.

Table 5.4 Room temperature Hall measurement results

Carrier concentration n (cm^{-3})	Mobility μ ($cm^2V^{-1}s^{-1}$)	Hall coefficient R_H ($cm^3C^{-1}V^{-1}$)	Magnetoresistance Ω (Ω)	Conductivity σ ($\Omega^{-1}cm^{-1}$)
$\sim 1.263 \times 10^{13}$	~ 38.48	$\sim 4.942 \times 10^5$	$\sim 5.544 \times 10^6$	$\sim 7.78 \times 10^{-5}$

Thermoelectric energy conversion at lower temperatures (around and below 300 K) can benefit a wide range of applications including refrigeration, air conditioning, and cryogenic cooling (17) but is also challenging mainly because the diffusive Seebeck coefficient drops in magnitude whereas the thermal conductivity increases as the temperature decreases. It is therefore tempting to make use of the phonon drag effect to boost the Seebeck

coefficient for better thermoelectrics at lower temperatures [38]. Figure 5.15 shows the variation of Seebeck coefficient S of $\text{Pb}_{3.58}\text{Sb}_{4.42}\text{Se}_{10}$ film in the temperature range of 11–300 K.

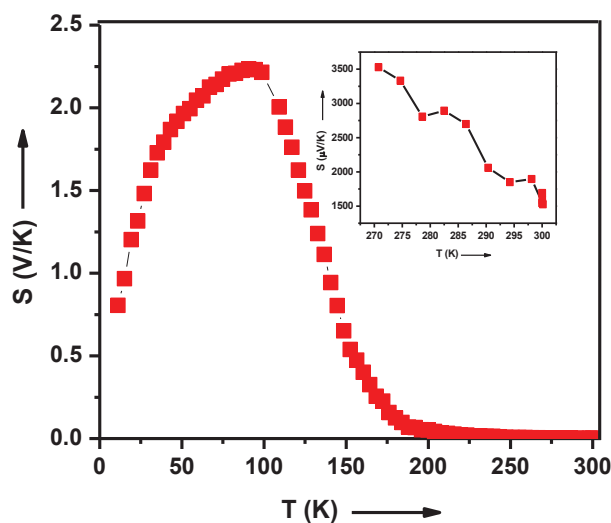


Fig. 5.15 The variation of the Seebeck coefficient with temperature.

The Seebeck coefficient of the deposited films was found to be positive indicating the predominant p-type behavior of $\text{Pb}_{3.58}\text{Sb}_{4.42}\text{Se}_{10}$ film. It is observed that S is slightly varying in the range $1691 \mu\text{VK}^{-1}$ to $3332 \mu\text{VK}^{-1}$ from 300 K to 273 K which is a typical behaviour of a non-degenerate semiconductor (inset of fig. 5.15). As temperature decreases S starts to increase abruptly and the film shows a giant Seebeck coefficient of 2.23VK^{-1} at about 90 K. The further decrease in temperature diminishes the thermoelectric power rapidly. The peak at 90 K indicates the presence of substantial phonon drag

effects in this sample contributing to a giant Seebeck coefficient at low temperature. For non-degenerate semiconductors [39],

$$S = \pm \frac{k_B}{e} \left[A + \frac{E_F}{k_B T} \right] \quad (1.8)$$

where E_F is the separation of the Fermi level from the top of the valence band, e is the charge of the electron and k_B is the Boltzmann's constant. $A = \left(\frac{5}{2} - s \right)$ is transport term, a constant varies from 0 to 4 depends on the scattering process. The scattering parameter A is found to be 2, indicates the presence of acoustic phonon scattering.

Table 5.4 The semiconductor properties of $\text{Pb}_{3.58}\text{Sb}_{4.42}\text{Se}_{10}$ film at Fermi level

Fermi level E_F (eV)	Effective mass m^*	Density of states N (cm^{-3})	Relaxation time τ (s)	Fermi velocity v_F (m s^{-1})	Mean free path l (nm)
~ 0.454	$\sim 0.00044 m_0$	$\sim 2.29 \times 10^{14}$	$\sim 0.096 \times 10^{-16}$	1.9×10^7	~ 18.24

The Fermi level lies deep in the band gap of the material. The film shows an electrical conductivity of $7.786 \times 10^{-5} \Omega^{-1}\text{cm}^{-1}$ and the Seebeck coefficient of $1691 \mu\text{VK}^{-1}$ at room temperature, resulting in a moderate power factor of $2.23 \times 10^{-8} \text{Wcm}^{-1}\text{K}^{-2}$. Even though effective mass ($0.00044 m_0$) is low, the low electrical conductivity is due to the low carrier concentration. Although its power factor at room temperature is lower than those of state-of-the-art thermoelectric materials, the giant S value at low temperature can be prospectively beneficial for low temperature applications with high performance [40].

5.4 Conclusion

The optimizations of the reactively evaporated p-type nano-structured lead antimony selenide ($\text{Pb}_{3.58}\text{Sb}_{4.42}\text{Se}_{10}$) thin films, the optical and transport properties are reported. The structural parameters such as dislocation density, number of crystallites per unit area and lattice strain in a typical film are estimated as 1.6×10^{15} lines m^{-2} , 3.84×10^{14} m^{-2} and 2.267×10^{-3} . The average particle size is obtained as 25 nm. The films are found to be p-type and their conductivities are of the order of $7.78 \times 10^{-5} \Omega^{-1}\text{cm}^{-1}$. Differential life time of carriers is also calculated and is increasing with decay time. An optical band gap of 1.31 eV, high absorbance ($>10^4 \text{cm}^{-1}$) and optical conductivity reported here for $\text{Pb}_{3.58}\text{Sb}_{4.42}\text{Se}_{10}$ thin films suggests the possible application of these films as absorber layer in solar cell. The maximum TE power of 2.3VK^{-1} occurs at 90 K and a relatively higher S of about $1691 \mu\text{VK}^{-1}$ is exhibited at room temperature. These results are promising in the realization of room temperature and even lower temperature thermoelectric application with high performance. The combination of both optical and TE properties of $\text{Pb}_{3.58}\text{Sb}_{4.42}\text{Se}_{10}$ thin films make them more prominent for PV-TE hybrid system and also for a variety of other PV-TE applications.

References

- [1] K. Park, S. Shin, A. S. Tazebay, H. Um, J. Jung, S. Jee, M. Oh, S. Park, B. Yoo, C. Yu and J. Lee, "Lossless hybridization between photovoltaic and thermoelectric devices," *Sci. Reports*, vol. 3, pp. 1–6, 2013.
- [2] Sima Aminorroaya-Yamini, Chao Zhang, Xiaolin Wang and Ivan Nevirkovets, "Crystal structure, electronic structure and thermoelectric properties of n-type BiSbSTe_2 ," *J. Phys. D Appl. Phys.*, vol. 45, p.

- 125301 1–6, 2012.
- [3] C. Wood, “Materials for thermoelectric energy conversion,” *Rep. Prog. Phys.*, vol. 51, pp. 459–539, 1988.
- [4] G. S. Nolas, M. Kaeser, R. T. Littleton IV, and T. M. Tritt, “High figure of merit in partially filled ytterbium skutterudite materials,” *Appl. Physics Letters*, vol. 77, pp. 1855–1857, 2000.
- [5] X. Shi, J. Yang, J. R. Salvador, M. Chi, J. Y. Cho, H. Wang, S. Bai, J. Yang, W. Zhang and L. Chen, “Multiple-filled skutterudites: High thermoelectric figure of merit through separately optimizing electrical and thermal transports,” *J. Am. Chem. Soc. Chem. Soc.*, vol. 133, pp. 7837–7846, 2011.
- [6] G. S. Nolas, D. T. Morelli and T. M. Tritt, “SKUTTERUDITES: A Phonon-Glass-Electron Crystal Approach to Advanced Thermoelectric Energy Conversion Applications,” *Annu. Rev. Mater. Sci.*, vol. 29, pp. 89–116, 1999.
- [7] P. Norouzzadeh¹, C. W. Myles and D. Vashaee, “Prediction of Giant Thermoelectric Power Factor in Type-VIII Clathrate Si₄₆,” *Sci. Reports*, vol. 4, pp.7028 1–5, 2014.
- [8] T. Takabatake and K. Suekuni, “Phonon-glass electron-crystal thermoelectric clathrates: Experiments and theory,” *Rev. Mod. Phys.*, vol. 86, pp. 669–716, 2014.
- [9] G. S. Nolas, J. L. Cohn, G. A. Slack, and S. B. Schujman, “Semiconducting Ge clathrates: Promising candidates for thermoelectric applications,” *Appl. Physics Letters*, vol. 73, pp. 178–180, 1998.
- [10] G. S. Nolas, G. A. Slack, G. S. Nolas, and G. A. Slack, “Thermoelectric

- Clathrates - Cage like crystals may soon help to pump heat with electricity and to create electricity with heat,” *Sigma Xi, Sci. Res. Soc.*, vol. 89, pp. 136–141, 2001.
- [11] J. W. Simonson, D. Wu, W. J. Xie, T. M. Tritt, and S. J. Poon, “Introduction of resonant states and enhancement of thermoelectric properties in half-Heusler alloys,” *Phys. Rev. B*, vol. 83, pp. 235211 1-9, 2011.
- [12] T. M. Tritt, “Holey and Unholey Semiconductors,” *Science*, vol. 283, no. 1999, pp. 804–805, 1999.
- [13] G. S. Nolas, J. Poon, and M. Kanatzidis, “Recent Developments in Bulk Thermoelectric Materials,” *MRS Bull.*, vol. 31, pp. 199–205, 2006.
- [14] D. Chung, T. Hogan, P. Brazis, M. Rocci-lane, C. Kannewurf, M. Bastea, C. Uher, and M. G. Kanatzidis, “CsBi₄Te₆: A High-Performance Thermoelectric Material for Low-Temperature Applications,” *Science*, vol. 287, pp. 1024–1027, 2000.
- [15] Y. Pei, X. Shi, A. Lalonde, H. Wang, L. Chen, and G. J. Snyder, “Convergence of electronic bands for high performance bulk thermoelectrics,” *Nature*, vol. 473, pp. 66–69, 2011.
- [16] N. Chen, F. Gascoin and G. J. Snyder, “Macroscopic thermoelectric inhomogeneities in (AgSbTe₂)_x(PbTe)_{1-x},” *Appl. Physics Letters*, vol. 87, p. 171903 1-3, 2005.
- [17] S. D. Mahanti, P. Larson, Duck-Young Chung, S. Sportouch and M. G. Kanatzidis, “Electronic structures of complex chalcogenides and other narrow band gap thermoelectric materials,” *Mat. Res. Soc. Symp. Proc.*, vol. 545, p. 23, 1999.
- [18] K. Koumoto, i. Terasaki and R. Funahashi, “Complex Oxide Materials

- for Potential Thermoelectric Applications,” *MRS Bull.*, vol. 31, pp. 206–210, 2006.
- [19] H. Böttner, G. Chen and R. Venkatasubramanian, “Aspects of Thin-Film Superlattice Thermoelectric Materials, Devices, and Applications,” *MRS Bull.*, vol. 31, pp. 211–217, 2006.
- [20] M. G. Kanatzidis, “Nanostructured Thermoelectrics: The New Paradigm,” *Chem. Mater. Rev.*, vol. 22, pp. 648–659, 2010.
- [21] D. Hitchcock, Yen-Liang Liu, Y. Liu, T. M. Tritt, J. He, And Chia-Jyi Liu, “Low temperature thermoelectric properties and aging phenomena of nanostructured p-type $\text{Bi}_{2-x}\text{Sb}_x\text{Te}_3$ ($x=1.46, 1.48, 1.52$ and 1.55),” *Funct. Mater. Lett.*, vol. 06, pp. 1340008 1-4, 2013.
- [22] W. Xie, S. Wang, S. Zhu, J. He, X. Tang, Q. Zhang, and T. M. Tritt, “High performance Bi_2Te_3 nanocomposites prepared by single-element-melt-spinning spark-plasma sintering,” *J. Mater. Sci.*, vol. 48, no. 7, pp. 2745–2760, 2013.
- [23] Lin-Hui Ye, K. Hoang, A. J. Freeman, S. D. Mahanti, J. He, T. M. Tritt, and M. G. Kanatzidis, “First-principles study of the electronic, optical, and lattice vibrational properties of AgSbTe_2 ,” *Phys. Rev. B*, vol. 77, p. 245203 1-6, 2008.
- [24] N. S. Patil, A. M. Sargar, S. R. Mane, and P. N. Bhosale, “Effect of Sb doping on thermoelectric properties of chemically deposited bismuth selenide films,” *Mater. Chem. Phys.*, vol. 115, pp. 47–51, 2009.
- [25] J. Kim, J. Choi, J. Bae, M. Kim, and T. Oh, “Thermoelectric Characteristics of n-Type Bi_2Te_3 and p-Type Sb_2Te_3 Thin Films Prepared by Co-Evaporation and Annealing for Thermopile Sensor Applications,” *Mater. Trans.*, vol. 54, no. 4, pp. 618–625, 2013.

- [26] B. Parida, S. Iniyan, and R. Goic, “A review of solar photovoltaic technologies,” *Renew. Sustain. Energy Rev.*, vol. 15, pp. 1625–1636, 2011.
- [27] Powder Diffraction file, International Centre for Diffraction Data (ICDD) Card No: 80-0654.
- [28] Namitha Asokan T., K. S. Urmila and B. Pradeep, “Structural, optical, transient photoconductivity studies and low temperature thermoelectric power measurements on reactively evaporated lead selenide thin films” *J. Mater. Sci: Mater. Electron.*, vol. 27, pp. 5646–5653, 2016
- [29] A. F. Qasrawi, “Temperature dependence of the band gap, refractive index and single-oscillator parameters of amorphous indium selenide thin films,” *Opt. Mater.* 29, vol. 29, pp. 1751–1755, 2007.
- [30] A. K. S. Aqili, Z. Ali, and A. Maqsood, “Optical and structural properties of two-sourced evaporated ZnTe thin films,” *Appl. Surf. Sci.* 167, vol. 167, pp. 1–11, 2000.
- [31] E. Marquez, J. Ramirez-Malot, P. Villarest, R. Jimbnez-Garayt, P. J. S. Ewen and A. E. Owen, “Calculation of the thickness and optical constants of amorphous arsenic sulphide films from their transmission spectra,” *J. Phys. D Appl. Phys.*, vol. 25, pp. 535–541, 1992.
- [32] E. R. Shaabana, I. S. Yahiab and E. G. El-Metwally, “Validity of Swanepoel’s Method for Calculating the Optical Constants of Thick Films,” *Acta Phys. Pol. A*, vol. 121, no. 3, pp. 628–635, 2012.
- [33] S. H. Wemple and M. DiDomenico, “Behavior of the Electronic Dielectric Constant in Covalent and Ionic Materials,” *Phys. Rev. B*, vol. 3, pp. 1338–1351, 1997.

- [34] S. H. Wemple and M. DiDomenico, "Optical Dispersion and the Structure of Solids," *Phys. Rev. Lett.*, vol. 23, pp. 1156–1160, 1969.
- [35] K. Tanaka, "Optical Properties and Photoinduced Changes in Amorphous As-S Films," *Thin Solid Films*, vol. 66, pp. 271–279, 1980.
- [36] S. M. El-Sayed, "Optical investigations of the indium selenide glasses," *Vacuum*, vol. 72, pp. 169–175, 2004.
- [37] A. Kumar, S. Goel and S. K. Tripathi, "Steady-state and transient photoconductivity in amorphous thin films of $\text{Ge}_x\text{Se}_{100-x}$," *Phys. Rev. B*, vol. 38, no. 18, pp. 432–435, 1988.
- [38] J. Zhou, B. Liao, Bo Qiu, S. Huberman, K. Esfarjani, M. S. Dresselhaus, and G. Chen, "Ab initio optimization of phonon drag effect for lower-temperature thermoelectric energy conversion," *PNAS*, vol. 112, no. 48, pp. 14777–14782, 2015.
- [39] K. P. Mohanchandra and J. Uchil, "Thermoelectric power CdS and CdSe films deposited on vibrating substrates," *Thin Solid Films*, vol. 305, pp. 124–129, 1997.
- [40] Xiao Zhang and Li-Dong Zhao, "Thermoelectric materials: Energy conversion between heat and electricity," *Journal of Materiomics*, vol. 1, pp. 92–105, 2015.

Chapter 6

Reactively evaporated n-type silver selenide thin films and its characterization

6.1 Introduction

6.2 Experimental details

6.3 Results and discussions

6.4 Conclusion

6.1 Introduction

Silver selenide is a semiconducting material of the I-VI binary semiconducting group, with a narrow band gap and is found in nature as a component of minerals, the so called Naumannite. It undergoes a structural phase transition from the low temperature phase (Orthorhombic, Tetragonal and Triclinic structures) to high temperature phase (Cubic structure) at the transition temperature [1]–[8]. The low temperature phase has a metallic behaviour and the high temperature phase exhibits the characteristics of a semiconductor [9]. The appearance of large magnetoresistance (MR) in a non-magnetic material like silver selenide has greatly enhanced the interest in silver selenide, even though both Ag and Se are non-magnetic and in addition, stoichiometric silver selenide does not exhibit significant MR [10]–[12]. Studies on thin films of Ag₂Se are attracting wide attention for various non-

linear optical devices [13], rechargeable secondary devices, multipurpose ion-selective electrodes, infra-red sensors [14], photolithographic layers [15], electrochemical potential memory devices [16], semiconducting optical devices for visible region [17], [18], Schottky barrier, resistive random-access memory (ReRAM) device [19] and super ionic conductor [20]. There are a few works available in the literature on silver selenide thin films. Safran et. al. [21] have reported the TEM studies of thin film samples of Ag_2Se prepared by high-temperature successive deposition of polycrystalline silver thin films and selenium. Gnanadurai et. al. [22] have investigated the effect of heating rate on hysteresis in the phase transition temperature of silver selenide thin films in the temperature range 300–430 K, for different heating rates from 0.25 to 2 K/min. Mogwitz et. al. [23] described the preparation of thin Ag_{2+x}Se films by pulsed laser deposition in argon as background gas. The authors report the large and linear magnetoresistance effect of the as prepared silver-rich silver selenide. Hong–Kim et al [24] synthesized first silver metal film using chemical vapor deposition and the Ag_2Se film by selenium vapor deposition. The phase transition phenomenon and cluster formation for two types of Ag_2Se ie α -phase and β -phase were discussed by Kumashiro et. al.[4]. Santhosh Kumar and Pradeep [25]–[27] used the method reactive evaporation for the deposition of Ag_2Se thin films on glass substrates at a temperature of about 398 ± 5 K. After deposition the substrate temperature was maintained for 45 minute to 1 hour at the coating temperature to stabilize the reaction. Recently Pandiaraman and Soundararajan [20] have reported the optical studies of thermally evaporated silver selenide thin films using micro-Raman spectrometer. Present

work reports the results of the structural, morphological, compositional, optical and some electrical studies of Ag₂Se thin films which have been deposited successfully without in-situ annealing using reactive evaporation technique. The microstructural properties are examined. Morphological and chemical compositional analyses are done. Band gap and the Urbach energy are calculated using absorption spectrum. The electrical, photoconductivity and thermoelectric properties are also reported.

6.2 Experimental details

Preparation of Ag₂Se thin films onto ultrasonically cleaned glass substrates were carried out using reactive evaporation method without in-situ annealing. For this, 99.999% pure silver was kept in a molybdenum boat and 99.999% pure selenium in glass crucible. The substrates were heated to a temperature of about 398 ± 5 K and a vacuum of the order of 10^{-5} torr. Immediately after deposition, the substrate temperature was reduced stepwise. The present approach essentially eliminates the use of in-situ annealing by optimizing the experimental conditions. Good quality films of thickness 400 nm were obtained with the following deposition parameters.

Table 6.1 Deposition parameters:

Impingement rate of Silver	$\approx 3 \times 10^{15}$ atoms $\text{cm}^{-2} \text{s}^{-1}$
Impingement rate of Selenium	$\approx 1 \times 10^{14}$ atoms $\text{cm}^{-2} \text{s}^{-1}$
Substrate temperature	$= 398 \pm 5$ K

The film was characterized by X-ray diffraction (XRD) using Rigaku D MaxC X-Ray Diffractometer with Cu-K α radiation ($\lambda = 1.5406$ Å, operated at 30kV, 20mA). The data were collected in the 30°–60° range and a step size

of 0.02° was selected for resolution. The composition and surface morphology of thin films were determined using JEOL JSM 6390 LV scanning electron microscope. The surface morphology was measured by AFM nanoscope E Digital Instrument. Optical characterization was done using JASCO V-570 UV Vis–NIR spectrophotometer and thickness measurement is done using Veeco Dektak 6M Stylus Profiler. The electrical conductivity measurements of the films were carried out by the two probe method in the temperature range 300–450 K. The area of the film was $3.4 \times 1.2 \text{ cm}^2$ and silver paste was applied to ensure good ohmic contacts to the film. Similarly, the photoconductivity measurements were carried out using the two probe method by applying voltage and measuring the current using Keithley source meter model 2611A.

6.3 Results and discussions

6.3.1 Structural analysis

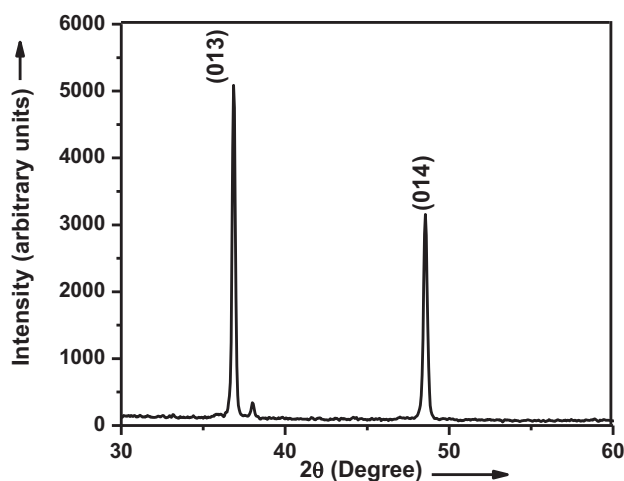


Fig. 6.1 X-ray diffraction pattern of a typical Ag_2Se sample

Figure 1 shows the X-ray diffraction pattern of the as prepared silver selenide thin film. Indexing of the XRD pattern is done in accordance with the ICDD file no. 71-2410 which corresponds to the reflections of orthorhombic phase of Ag_2Se with lattice parameters, $b = 7.36 \text{ \AA}$ and $c = 7.76 \text{ \AA}$ [28]. The peaks at $2\theta = 36.847$, and 48.551 match the standard pattern of Ag_2Se in intensities and the corresponding planes are (013) and (014) (table 6.2). This implies that the film is polycrystalline in nature. The 100% peak in the standard pattern is absent. This may be due to the orientation of the (110) plane perpendicular to the film surface. The peak at $2\theta = 37.998$, $d = 2.3685$ of the XRD spectrum corresponds to elementary silver. The micro-structural parameters in the film are examined and the calculated results are tabulated in table 6.3 [29].

Table 6.2 The observed XRD data along with standard ICDD data

Standard pattern (ICDD Card No: 71-2410)			As prepared film	
(hkl)	d(Å)	I/I ₀	d(Å)	I/I ₀
110	3.6932	100	-	-
013	2.4299	22	2.4398	100
014	1.8715	10	1.8755	61

Table 6.3 Microstructural parameters:

Average particle size D (nm)	≈ 38
Dislocation density ρ (lines m^{-2})	$\approx 6.9252 \times 10^{14}$
Number of crystallite per unit area N (m^{-2})	$\approx 7.290 \times 10^{15}$
Strain T	$\approx 1.43 \times 10^{-3}$

6.3.2 Morphological and compositional analysis

The morphology of as-prepared film (SEM) is shown in figure 6.2 (with magnification of 15,000X). It is also observed that the as-deposited films are homogeneous, without cracks or holes and well covered to the substrates. The average size of the grain is about 25 – 40 nm, which corresponds well with the crystallite size calculated from XRD.

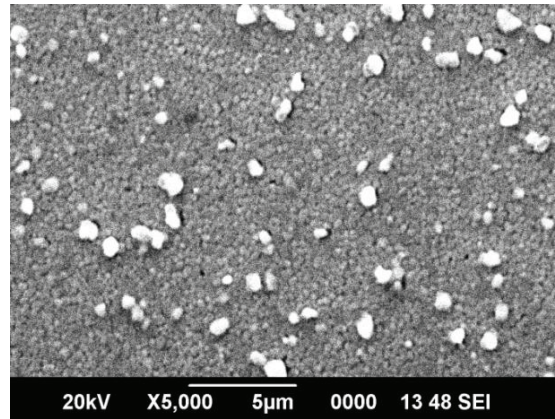


Fig. 6.2 Surface Morphology of Ag₂Se thin film

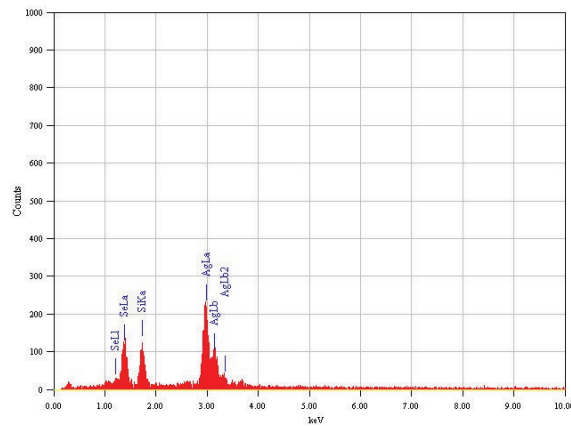


Fig. 6.3 EDAX spectra of a typical Ag₂Se thin film

The EDAX spectrum of as deposited silver selenide thin film is shown in figure 6.3. Figures 6.4(a) and 6.4(b) illustrate the X-ray photoelectron spectra of Ag 3d, and Se 3d for a typical Ag_2Se thin film. The XPS of the as-deposited silver selenide film reveals Ag $3d_{5/2}$ and $3d_{3/2}$ peaks at about 367.65 eV and 373.68 eV and Se $3d_{5/2}$ peak at 52.86 eV consistent with the pure silver selenide. Compositional analysis gives result as 61% of silver and 39% of selenium which confirms the films are nearly stoichiometric within experimental accuracy.

From AFM images (Fig. 6.5(a) and 6.5(b)), it is observed that the film has uniform distribution of agglomerated particles with well- defined boundaries. Grains of about 300 nm are observed in AFM (Fig. 6.5(a)) and the root mean square value of the surface roughness estimated is 13 nm (Fig. 6.5(b)).

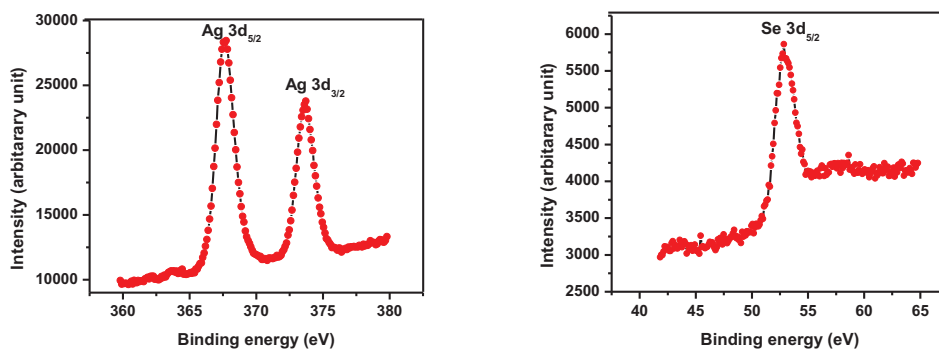


Fig. 6.4 Plots of (a) Silver 3d spectra and (b) Selenium 3d spectra of a typical Ag_2Se thin film

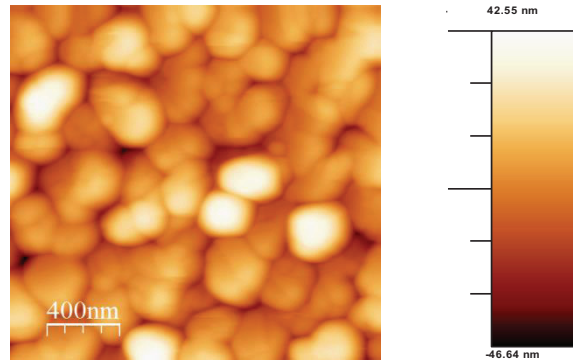


Fig. 6.5(a) The two dimensional AFM topography image of Ag₂Se thin film (area 2 X 2 μ m)

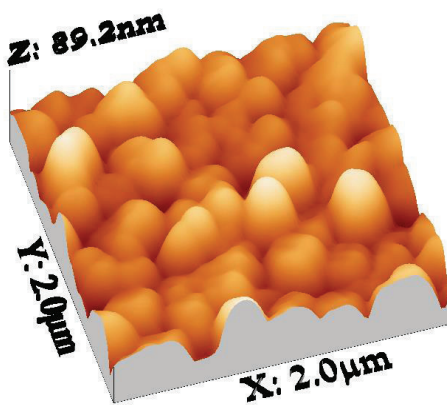


Fig. 6.5(b) The three dimensional AFM topography image of Ag₂Se thin film (area 2 X 2 μ m)

6.3.3 Electrical analysis

Figure 6.6 shows the variation of $\ln(I)$ versus temperature in the range 300–423K of the prepared thin film sample for three continuous cycles. The electrical conductivity is increasing linearly with increasing ambient

temperature in the range 300-398 K in the first cycle. At 398 K, it undergoes an endothermic phase transition from semiconductor to metallic by absorbing heat energy during heating. But during cooling, at 368 K it undergoes exothermic transition from metallic to semiconductor. From the slope of this curve, the activation energy is calculated and is 0.12eV.

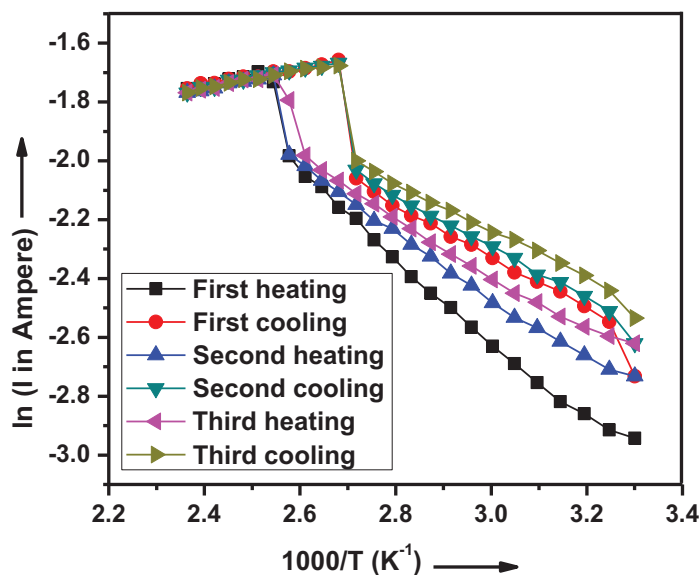


Fig. 6.6 Variation of $\ln(I)$ with inverse of temperature for a typical Ag_2Se sample

The phase transition temperature is 398 K in the first heating cycle and it is 393 K for the second and third cycles. The reverse transition takes place at 368 K for the three cycles. This result coincides with a similar dependence found by the authors [4], [22]. Then, to determine the type of conductivity, the hot

probe method was employed and it is observed that the as deposited sample showed n-type conductivity.

6.3.4 Optical analysis

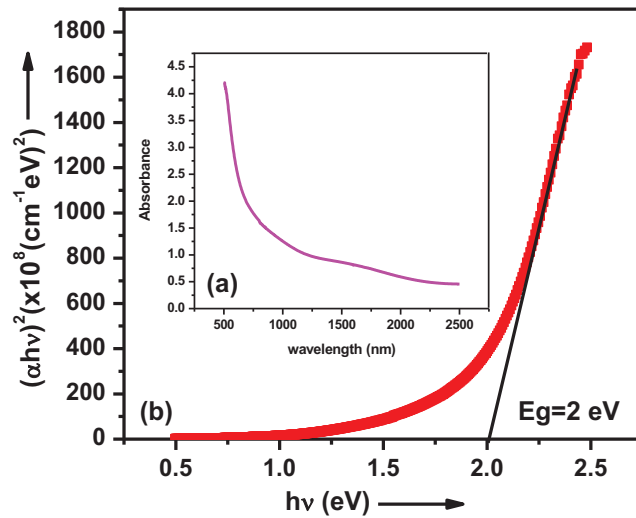


Fig. 6.7(a) Variation of absorbance with wavelength (b) The dependence $(\alpha h\nu)^2$ on photon energy.

The optical absorption spectra have been studied at room temperature in the wavelength range of 500-2500 nm (figure 6.7(a)). Ag_2Se being a direct band gap semiconductor [30], the optical gap can be determined using the well-known Tauc's relation. The plot of $(\alpha h\nu)^2$ versus photon energy ($h\nu$) of the Ag_2Se thin film is depicted in the figure 6.7(b). The earlier studies on optical properties of silver selenide show that optical band gap of silver selenide exists between 0.04 eV and 0.13 eV [31]. But recent reports show that it exists between 1.2 eV and 1.8 eV [32]. The optical band gap of the as

prepared film is found to be 2.0 eV, which is quite close to the optimum values for a buffer layer in photovoltaic cell. Absorption coefficient is found to be of the order of 10^4 - 10^5 cm^{-1} and it also suggests the possibility of the thin film in photovoltaic cell. In order to study the wavelength dependence of the extinction coefficient of the as-prepared thin film, the variation of the extinction coefficient (k) with photon energy is plotted and shown in figure 6.8. It is found to vary from 0.226 to 0.417 with increase in photon energy. A plot of $\ln(\alpha)$ against the photonenergy is shown in Fig. 6.9. The linearity of the graph confirms that the carrier transitions take place between the localized states in the band tail. A linear fit is established in the linear portions of the curve and the width of Urbach tail obtained from the fit is 895 meV [33], [34].

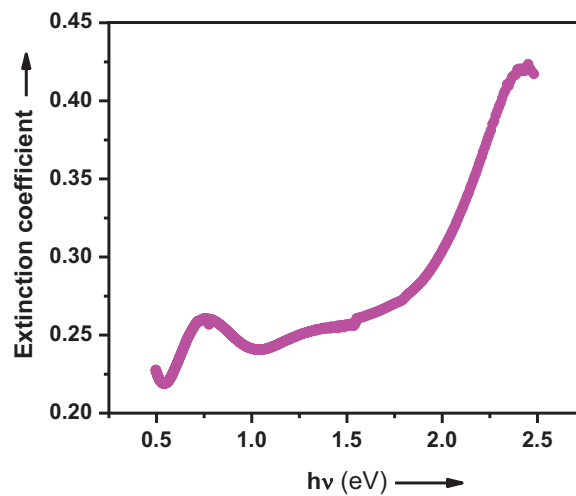


Fig. 6.8 Variation of extinction coefficient with photon energy

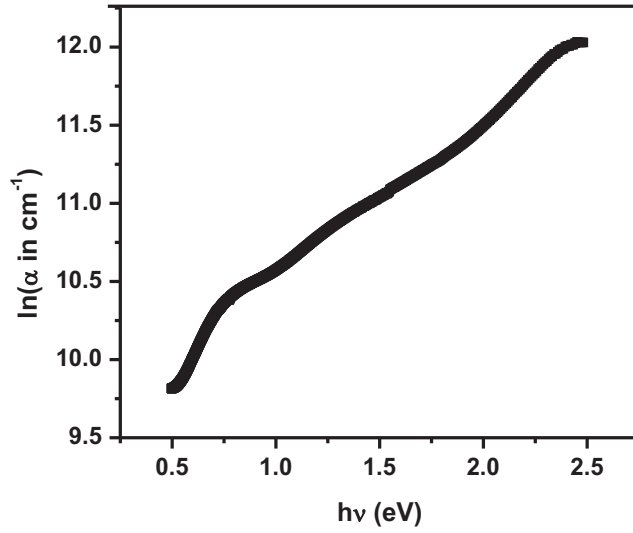


Fig. 6.9 Plot of $\ln(\alpha)$ against the photon energy for Ag_2Se film

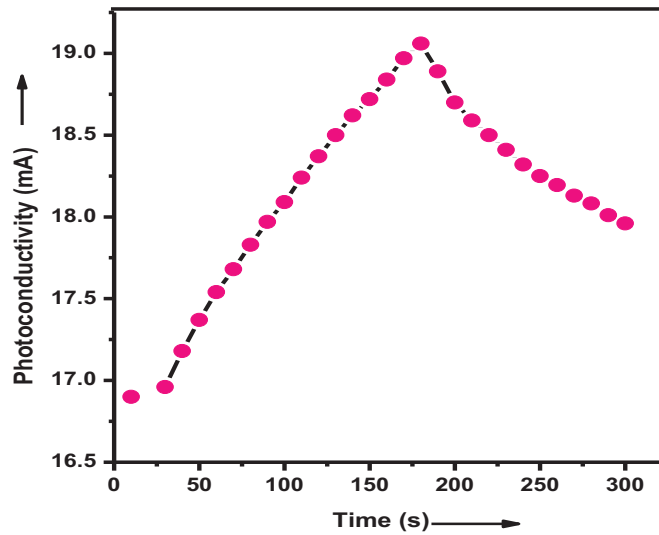


Fig. 6.10 The rise and decay of photocurrent in Ag_2Se film

The rise and decay of photocurrent of Ag_2Se sample at room temperature is depicted in Fig. 6.10. It is clear from this figure that the rise and decay of the photocurrent is very slow in this material. The sample shows a little photoresponse, usually conductive samples show a small value of photoconductivity.

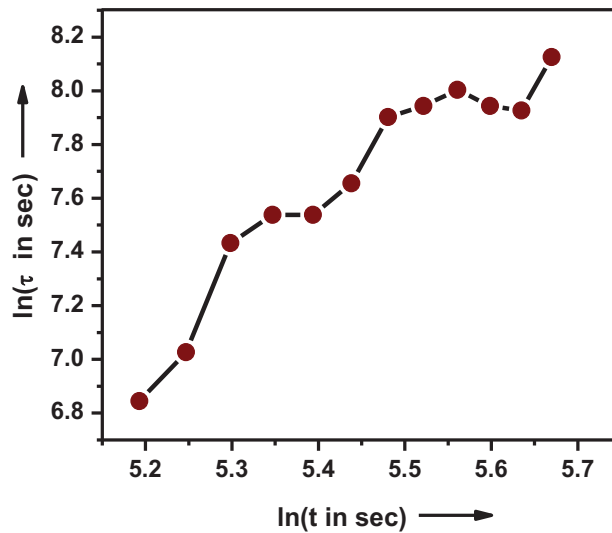


Fig. 6.11 The variation of differential life time with decay time

The increase in differential life time with time shown in figure 6.11 illustrates that the decay is non-exponential in nature. Therefore the slow decay may be ascribed due to deep traps or recombination centres that exist at all the energies in the band gap. The dispersion parameter (β) is calculated from the slope of $\ln(I_{ph})$ versus $\ln(t)$ (figure 6.12) and using the value of β , the localized state distribution parameter E_l is also calculated. The present photoconductivity behavior may be best understood in terms of recombination

centres within sample [35]. The recombination centres are originated from the localized energy states ($E_0=0.2695$ eV) present in the band gap of the material.

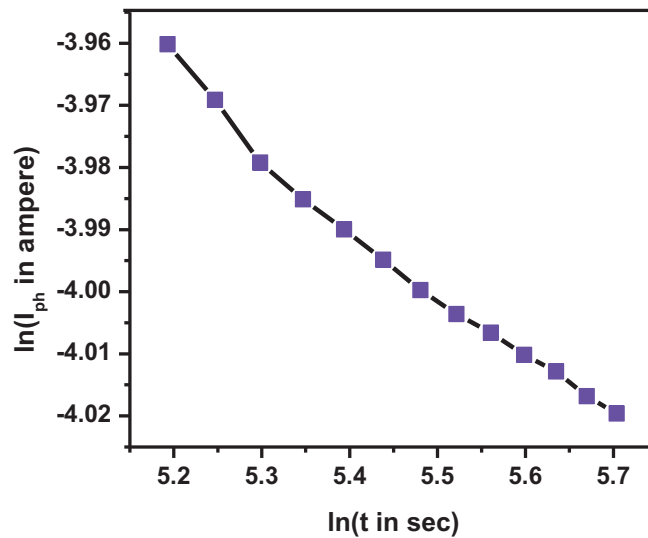


Fig. 6.12 The plot of $\ln(I_{ph})$ versus $\ln(t)$

6.3.5 Low temperature TEP properties and Hall measurement

The room temperature electrical properties of n-type Ag_2Se thin films obtained by the van der Pauw method are tabulated in table 6.4. The low temperature thermoelectric power (TEP) measurements in a typical Ag_2Se sample in the range 5–300 K is shown in figure 6.13. Several factors such as impurity, electron-phonon, phonon-phonon, electron-magnon etc affect individually or collectively to the T dependence of S [36].

Table 6.4 Hall effect measurement results

Carrier concentration n (cm^{-3})	Mobility μ ($\text{cm}^2 \text{V}^{-1} \text{s}^{-1}$)	Hall coefficient R_H ($\text{cm}^3 \text{C}^{-1} \text{V}^{-1}$)	Magnetoresistance (Ω)	Conductivity σ ($\Omega^{-1} \text{cm}^{-1}$)
3.21×10^{19}	2.517×10^2	0.194	0.2668	1.297×10^3

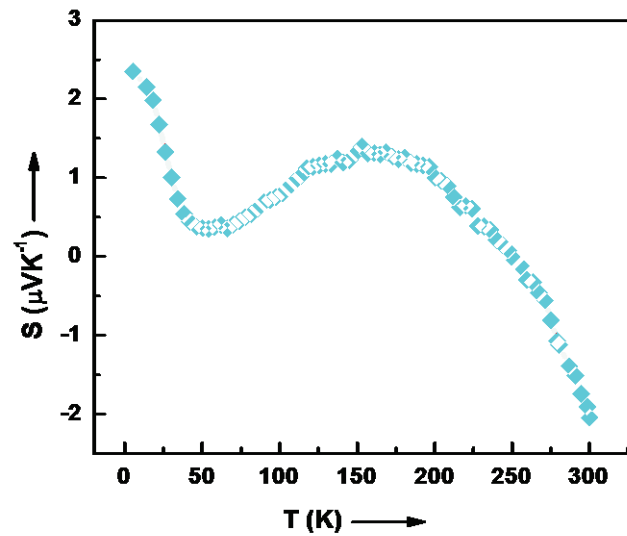


Fig. 6.13 The variation of Seebeck coefficient with temperature.

At room temperature, the negative value of TEP indicates the n-type conductivity of the sample and its value found to be around $2 \mu\text{VK}^{-1}$. Film shows a typical degenerate behavior of a degenerate semiconductor near room temperature. Using the optimum carrier concentration and S data, the Fermi level (E_F) is estimated as 3.6 eV (table 6.5). The deep Fermi level position in conduction band leads to low Seebeck coefficient at 300 K. The large value of

Hall mobility ($2.517 \times 10^2 \text{ cm}^2 \text{ V}^{-1} \text{ s}^{-1}$) due to reduced electron effective mass ($0.01 m_0$) is the cause of increased conductivity ($1297 \text{ } \Omega^{-1} \text{ cm}^{-1}$) in these films which is comparable to that reported in $\beta - \text{Ag}_2\text{Se}$ powders [37].

As seen in figure 6.13, Seebeck coefficient (S) is small and almost linear in T near room temperature indicates that the mere drift-diffusion mechanism dominates at higher temperature. As temperature is lowered below room temperature, it increases rapidly and below about 247 K, S converts to positive sign since the dominant carrier type changes from electrons to holes at 247 K due to the mixed conduction mechanism associated with the intrinsic conduction. At about 169 K, a TEP peak is observed, its value is $1.3 \text{ } \mu\text{VK}^{-1}$ and then it decreases with decreasing temperature. Again a dip in TEP is observed at around 54 K and it can also be seen that there is sharp increase in S at very low temperature which is opposite to the drift – diffusion mechanism. At very lower temperatures the number of intrinsic carriers is negligible compared to the number of carriers released by impurities, impurity scattering strongly affect the faster increase in TEP.

Table 6.5 The semiconductor properties of Ag_2Se film at Fermi level

Fermi level E_F (eV)	Effective mass m^*	Density of states N (cm^{-3})	Relaxation time τ (s)	Fermi velocity v_F (m s^{-1})	Mean free path l (nm)
~ 3.6	$\sim 0.01 m_0$	$\sim 2.49 \times 10^{16}$	$\sim 1.4 \times 10^{-15}$	$\sim 0.11 \times 10^8$	~ 15

The n-type film shows power factor of $0.52 \times 10^{-4} \text{ Wcm}^{-1} \text{ K}^{-2}$ at room temperature. The predicted power factor and the optimum carrier concentration is much greater in these thin films as compared to that reported in n-type

skutterudites at 300 K and n-type polycrystalline $\text{Bi}_x\text{Sb}_{2-x}\text{Te}_3$ alloys [38] [39]. Although optimum levels have not yet been reached, we believe additional improvements are possible by increasing the Seebeck coefficient through band modification in the density of states near the Fermi level.

6.4 Conclusion

Polycrystalline thin films of silver selenide are prepared by reactive evaporation technique to investigate the optoelectronic and thermoelectric properties. The micro-structural properties such as grain size, number of crystallites per unit area, dislocation density, and strain are examined. Morphological studies reveal that the Ag_2Se particles cluster into uniformly distributed grains. Photoconductivity is studied at room temperature. The rise and decay is found to be very slow in this material. Temperature dependence of electrical conductivity shows the semiconducting nature of the film upto the phase transition temperature 398 K and after it showed the metallic property. The anomalous behavior of TEP at low temperature, the maxima or minima due to impurity scattering are also reported. The films are n-type with high electrical conductivity of $1.3 \times 10^3 \Omega^{-1} \text{cm}^{-1}$. From the perspective of module fabrication the nearly stoichiometric and low resistive thin film of Ag_2Se with the room temperature power factor of $0.52 \times 10^{-4} \text{Wcm}^{-1}\text{K}^{-2}$ is always desirable to have compatible materials for the n-legs of a thermoelectric couple.

References

- [1] A. G. Abdullayev, R. B. Shafizade, E. S. Krupnikov, and K. V Kiriluk, "Phase Formation and Kinetics of the phase transition n Ag_2Se thin films," *Thin Solid Films*, vol. 106, pp. 175–184, 1983.

- [2] T. Okabe and K. Ura, "High-resolution electron-microscopic studies of the polymorphs in $\text{Ag}_{2+\delta}\text{Se}$ films," *J. Appl. Cryst.*, vol. 27, pp. 140–145, 1994.
- [3] L. V. Constantinescu, "Orientation in polymorphic films obtained by vacuum evaporation of Ag-Se," *Thin Solid Films*, vol. 32, pp. 333–337, 1976.
- [4] T. O. Kumashiro, T. Ohachi and I. Taniguchi, "Phase transition and cluster formation in silver selenide," *Solid State Ionics*, vol. 86–88, pp. 761–766, 1996.
- [5] G. Safran, L. Malicsko, O. Geszti and G. Radnoczi, "The formation of (0 0 1) oriented Ag_2Se films on amorphous and polycrystalline substrates via polymorphic-phase transition," *J. Cryst. Growth*, vol. 205, pp. 153–162, 1999.
- [6] G. Safran, P. Keusch, J. R. Giinter and P. B. Barna, "Development and properties of single-crystal silver selenide layers," *Thin Solid Films*, vol. 215, pp. 147–151, 1992.
- [7] K. Yin, Y. Xia, Z. Liu, J. Yin, and L. Sun, "Electron-beam induced phase transformation in $\beta\text{-Ag}_2\text{Se}$ thin films," *Phys. Status Solid A*, vol. 209, no. 1, pp. 135–138, 2012.
- [8] Y. Saito, M. Sato, and M. Shiojiri, "Orientation in Ag_2Se polymorphic films produced by the reaction of silver films with selenium," *Thin Solid Films*, vol. 79, pp. 257–266, 1981.
- [9] C. M. Fang, R. A. de Groot, and G. A. Wieggers, "Ab initio band structure calculations of the low-temperature phases of Ag_2Se , Ag_2Te and Ag_3AuSe_2 ," *J. Phys. Chem. Solids*, vol. 63, pp. 457–464, 2002.
- [10] B. C. Mohanty and S. Kasiviswanathan, "Thermal stability of silver selenide thin films on silicon formed from the solid state reaction of Ag and Se films," *Thin Solid Films*, vol. 515, pp. 2059–2065, 2006.

- [11] G. Beck and J. Janek, "Negative and linear positive magnetoresistance effect in silver-rich silver selenide," *Solid State Sci.*, vol. 10, pp. 776–789, 2008.
- [12] J. Xu, D. Zhang, F. Yang, Z. Li, Z. Deng, and Y. Pan, "A metal – semiconductor composite model for the linear magnetoresistance in high magnetic field," *Phys. B*, vol. 403, pp. 4000–4005, 2008.
- [13] B. H. An , H. M. Ji, J. Wu , M. K. Cho, K. Yang, H. Lee, Y. K. Kim, "Phase changeable silver selenide thin films fabricated by pulse electrodeposition," *Curr. Appl. Phys.*, vol. 9, pp. 1338–1340, 2009.
- [14] B. Pejova, M. Najdoski, I. Grozdanov, and S. K. Dey, "Chemical bath deposition of nanocrystalline (111) textured Ag₂Se thin films," *Mater. Lett.*, vol. 43, pp. 269–273, 2000.
- [15] P. K. Khanna and B. K. Das, "Novel synthesis of silver selenide nano-powder from silver nitrate and organo-selenium compound," *Mater. Lett.*, vol. 58, no. 6, pp. 1030–1034, 2004.
- [16] S. J. Pawar, P. P. Chikode, V. J. Fulari, and M. B. Dongare, "Studies on electrodeposited silver selenide thin film by double exposure holographic interferometry," *Mater. Sci. Eng. B*, vol. 137, pp. 232–236, 2007.
- [17] K. Li, X. Liu, H. Wang, and H. Yan, "Rapid synthesis of Ag₂Se nanocrystals by sonochemical reaction," *Mater. Lett.*, vol. 60, pp. 3038–3040, 2006.
- [18] H. Kim, H. Jeong, K. S. Kim, S. H. Yoon, S. S. Lee, K. W. Seo, and I. Shim, "Syntheses of Liquid Phase [(efac)Ag(P(OR)₃)] Precursors and Their Application to the Preparation of Silver and Silver Selenide Thin Films," *Bull. Korean Chem. Soc. 2004*, vol. 25, no. 7, pp. 1068–1070, 2004.
- [19] N. J. Lee, M. R. Park, T. S. Yoon, Y. J. Choi, and C. J. Kang, "Resistive

- switching characteristics of Ag₂Se thin film,” *Proc. IEEE Conf. Nanotechnol.*, 2012.
- [20] M. Pandiaraman and N. Soundararajan, “Micro-Raman studies on thermally evaporated Ag₂Se thin films,” *J. Theor. Appl. Phys.*, vol.6, pp. 1–5, 2012.
- [21] G. Safran, O. Geszti, G. Radnoczi and P. B. Barna “TEM study of Ag₂Se developed by the reaction of polycrystalline silver films and selenium,” *Thin Solid Films*, vol. 317, pp. 72–76, 1998.
- [22] P. Gnanadurai, N. Soundararajan, and C. E. Sooriamoorthi, “Influence of heating rate on the hysteresis in the phase transition in silver selenide thin films,” *Vacuum*, vol. 78, pp. 33–36, 2005.
- [23] B. Mogwitz, C. Korte, J. Janek, M. V. Kreutzbruck, and L. Kienle, “Preparation and magnetoresistance of Ag_{2+x}Se thin films deposited via pulsed laser deposition,” *J. Appl. Phys.*, vol. 101, no. 4, p. 043510, 2007.
- [24] H. Kim, H. Jeong, K. S. Kim, S. H. Yoon, S. S. Lee, K. W. Seo, I. Shim, “Preparation of silver thin films using liquid-phase precursors by metal organic chemical vapor deposition and their conversion to silver selenide films by selenium vapor deposition,” *Thin Solid Films*, vol. 478, pp. 72–76, 2005.
- [25] M. C. Santhosh Kumar and B. Pradeep, “Structural, electrical and optical properties of silver selenide thin films,” *Semicond. Sci. Technol.*, vol. 17, pp. 261–265, 2002.
- [26] M. C. Santhosh Kumar and B. Pradeep, “Transport properties of silver selenide thin films from 100 K to 300 K,” *Mater. Lett.*, vol. 56, pp. 491–495, 2002.
- [27] M. C. Santhosh Kumar and B. Pradeep, “Preparation and electrical properties of silver selenide thin films by reactive evaporation,” *Bull.*

- Mater. Sci.*, vol. 25, pp. 407–411, 2002.
- [28] *Powder Diffraction file, International Centre for Diffraction Data (ICDD) Card No: 71-2410.*
- [29] T. Namitha Asokan, K. S. Urmila, and B. Pradeep, “Structural, optical, transient photoconductivity studies and low temperature thermoelectric power measurements on reactively evaporated lead selenide thin films,” *J. Mater. Sci. Mater. Electron.*, vol. 27, pp. 5646–5653, 2016.
- [30] A. B. Kulkarni, M. D. Uplane and C. D. Lokhande, “Preparation of silver selenide from chemically deposited silver films,” *Thin Solid Films*, vol. 260, pp. 14–18, 1995.
- [31] M. Pandiaraman, N. Soundararajan, C. Vijayan, C. Kumar and R. Ganesan, “Spectroscopic Studies on Silver Selenide Thin Films,” *J. Ovonic Res.*, vol. 6, no. 6, pp. 285–295, 2010.
- [32] M. B. Dongare and S. J. Pawar, “Low temperature route for synthesis of silver selenide thin films and their properties: annealing effect,” *Material Science An indian Journal*, vol.2, no. 6, pp. 122-125, 2006.
- [33] F. Urbach, “The long-wavelength edge of photographic sensitivity and of the electronic Absorption of Solids,” *Phys. Rev.*, vol. 92, p. 1324, 1953.
- [34] L. B. Chandrasekar, R. Vijayalakshmi, B. Rajeswari, R. Chandramohan, G. Arivazhagan, and S. A. Packiaseeli, “Preparation and Characterization of Silver Selenide Thin Film,” *Brazilian J. Phys.*, vol. 44, pp. 653–657, 2014.
- [35] W. Fuhs and J. Stuke, “Hopping recombination in trigonal Selenium Single Crystals,” *Phys. Status Solid b*, vol. 27, pp. 171–184, 1968.
- [36] C. Herring, “Theory of the Thermoelectric Power of Semiconductors,” *Phys. Rev.*, vol. 96, no. 5, pp. 1163–1187, 1954.

- [37] H. Wang, Chu, D. Wang, Mao, Pan, Guo, Xiong, and Jin, “Low-Temperature Thermoelectric Properties of β -Ag₂Se Synthesized by Hydrothermal Reaction,” *J. Electront. Mater.*, vol. 40, pp62-628, 2011.
- [38] N. Gerovac, G. I. Snyder, and T. Caillat, “Thermoelectric properties of n-type polycrystalline Bi_xSb_{2-x}Te₃ alloys,” *21th International Conference on Thermoelectronics*, pp. 31-34, 2002.
- [39] C. Uher, “In search of efficient n-type skutterudite thermoelectrics,” *21th International Conference on Thermoelectronics*, pp. 35-41, 2002.

Chapter 7

Reactively evaporated n-type silver antimony selenide thin films and its characterization

- 7.1 Introduction**
- 7.2 Experimental details**
- 7.3 Results and discussions**
- 7.4 Conclusion**

7.1 Introduction

The binary silver selenide and its related ternary semiconducting materials are of great attention because of the importance of investigation on new materials for various optoelectronic applications that should be more efficient, highly reproducible and less toxic. The studies on I-V-VI₂ chalcopyrites have been done extensively because of their strong absorbing properties that make these materials good for photovoltaic applications [1][2][3]. The silver antimony selenide thin film exists in two phases—cubic AgSbSe₂ and orthorhombic Ag₅SbSe₄. Cubic AgSbSe₂ being a narrow band gap p-type semiconductor, is one of the semiconducting materials which have NaCl structure. AgSbSe₂ is particularly disordered with selenium atoms occupying the chlorine sites, while silver and antimony atoms are arranged randomly on the sodium sites [4][5]. The high thermoelectric performance of AgSbSe₂, a lower cost and most abundant analog of AgSbTe₂, has been a

relatively recent discovery. It has been prepared by various processing techniques, including vacuum evaporation [6][7][8][9], chemical deposition [10] and direct fusing the constituent elements in a vacuum sealed quartz tube [1]. A. Abdelghany et al [11] carried out measurements on the electrical conductivity and thermoelectric power of the AgSbSe_2 in the solid and liquid states from 350 to 975⁰C. Bindu et al [12][13] have been reported the possibilities of this material as an absorber layer for the $\text{SnO}_2\text{-CdS-(i)Sb}_2\text{Se}_3\text{-(p)AgSbSe}_2$ photovoltaic structure. They have also reported the thermoelectric measurements on AgSbSe_2 thin film in the temperature range of 250-320 K. Wojciechowski et al [14] points out the semiconducting with a narrow band or semi-metallic properties of this materials by studying the electrical conductivity and the Seebeck coefficient ($320 \mu\text{VK}^{-1}$ at room temperature) is measured as a function of temperature in the range from 300-600 K. Maksymilian Schmidt et al [15] estimated the value of E_g of this material and is 0.09 eV indicating the semi-metallic feature and alloying of AgSbSe_2 compounds exhibit apparent semiconducting behavior. AgSbSe_2 compounds show promising thermoelectric properties by virtue of its very low thermal conductivity and relatively high power factor. It is reported that the thermal conductivities of the AgSbSe_2 semiconductors are impressively low due to the strong anharmonicity of their chemical bonds in the crystal structure [16]. Moreover, the disordered character of this compound, crystallizes in a cubic NaCl-type structure in which Ag and Sb randomly occupy the same crystallographic position, is a factor of extremely low thermal conductivity [16]. The AgSbSe_2 have been studied previously, however, the literature survey

showed that the low temperature thermoelectric studies on the indirect band gap semiconductor AgSbSe₂ were not reported. The analysis of thermoelectric power (TEP) as a function of temperature is particularly significant to assess the relative strength of the electron-phonon interactions and all other phonon interactions. In this work, we report the deposition of AgSbSe₂ thin films without in-situ annealing using reactive evaporation technique. To evaluate the potentiality of this material for optoelectronic and thermoelectric applications, structural, electrical, optical and low temperature thermoelectric properties to enlighten the electron transport behavior, are also studied and presented.

7.2 Experimental details

The AgSbSe₂ thin films were deposited on glass substrates in a vacuum of 10⁻⁵ torr. Glass substrates of 34×12×1 mm size were first cleaned using an industrial detergent and then ultrasonically agitated. These substrates were dried with hot air blower and then loaded on the substrate holder placed at a distance of 13cm from the evaporation sources. For the preparation of ternary AgSbSe₂, two separate glass crucibles kept in molybdenum baskets were used as sources for the evaporation of 99.999% pure elemental Sb and Se. A molybdenum boat was used for the evaporation of 99.999% pure Ag. System was evacuated to a vacuum better than 10⁻⁵ torr and the substrates were heated to the required temperature of 398 K. Substrates were maintained at that temperature for 15 minutes for stabilization. The temperature was monitored by DPM connected with a Chromel-Alumel thermocouple mounted on the substrate. First selenium atmosphere was made in the vacuum chamber and then silver and antimony were evaporated from separate sources by controlling

the current through the source. After deposition the substrate temperature was slowly reduced to room temperature. The crystallinity and stoichiometry of the compound depend on the incident fluxes and the substrate temperature and are optimized using the reactive evaporation technique. The optimized preparative parameters for obtaining the stoichiometric silver antimony selenide thin film using this technique are determined (table 7.1).

Table 7.1 Deposition parameters

Impingement rate of silver	$\approx 3 \times 10^{15} \text{ atoms cm}^{-2} \text{ s}^{-1}$
Impingement rate of antimony	$\approx 2 \times 10^{15} \text{ atoms cm}^{-2} \text{ s}^{-1}$
Impingement rate of selenium	$\approx 1 \times 10^{14} \text{ atoms cm}^{-2} \text{ s}^{-1}$
Substrate temperature	$\approx 398 \pm 5 \text{ K}$

The XRD measurements were done using Rigaku D – MaxC diffractometer with Cu-K α ($\lambda = 1.5404 \text{ \AA}$) radiation, operated at 30 kV, 20 mA. Optical absorbance spectra were recorded using JASCO V570 UV-Vis-NIR spectrophotometer with automatic computer data acquisition. SEM analysis to study the morphology of the film was done using JEOL JSM 6390 scanning electron microscope. Two probe method was used to study the temperature dependent electrical conductivity measurements in the temperature range of 300-450 K inside a conductivity cell at a pressure of 10^{-3} mbar and pairs of silver paint electrodes were applied on the film surface as ohmic contact. Thickness of the film was measured using the Veeco Dektak 6M Stylus Profiler. The thermoelectric power measurements were done using automated precision measurement setups for electrical resistivity and simultaneously thermoelectric power of different samples in the temperature range 5-325 K.

7.3 Results and discussions

7.3.1 Structural analysis

The X-ray diffraction pattern of a typical AgSbSe_2 thin film sample is shown in figure 7.1. The indexing of the pattern is done and the XRD data is compared with standard ICDD card no: 89-3670 of AgSbSe_2 compound exhibiting face centered cubic (fcc) with the space group $f m\bar{3}m$ [17] (table 7.2). The prominent peak in the pattern corresponds to the reflection from (200) plane. The relative intensities of the other peaks decrease since the penetration depth of the X-ray decreases as angle increases.

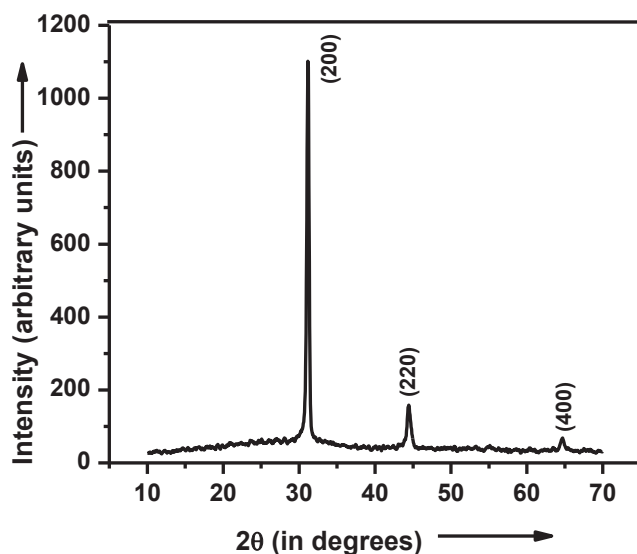


Fig. 7.1 X-ray diffraction spectra of a typical AgSbSe_2 thin film.

The well-defined sharp peaks in the pattern suggest that the grains in the sample are randomly oriented along different crystallographic planes which indicate the polycrystalline nature of the prepared sample. The lattice

parameter of the AgSbSe₂ thin film is 0.5742 nm. The structural analysis showed the films are single phase with NaCl structure which is in agreement with that reported by Soliman et al [18]. The values of microstructural parameters such as particle size, dislocation density, number of crystallites per unit area and strain calculated are tabulated in table 7.3.

Table 7.2. The observed XRD data along with standard ICDD data

Standard pattern(ICDD Card No: 89-3670)			As prepared film	
(hkl)	d(Å)	I/I ₀	d(Å)	I/I ₀
200	2.8930	100	2.871	100
220	2.0456	90	2.039	15
400	1.4465	16	1.446	6

Table 7.3 Microstructural parameters

Average particle size D (nm)	22
Dislocation density ρ (lines m ⁻²)	2.066×10^{15}
Number of crystallite per unit area N (m ⁻²)	5.635×10^{15}
Strain T	2.8×10^{-3}

7.3.2 Morphological and compositional analysis

Figure 7.2 shows the Scanning Electron Microscopy (SEM) images of AgSbSe₂ thin film at 10,000 magnifications. From the figure it is clear that there are agglomerated clusters with formation of islands and is well separated. The film shows well defined grains, indicative of the polycrystalline nature of

the film. The grain size obtained from SEM is 300 nm, is much greater than that from XRD, which is expected due to the clustering of the particles. The EDAX spectrum for a typical representative sample of AgSbSe₂ films is shown in figure 7.3.

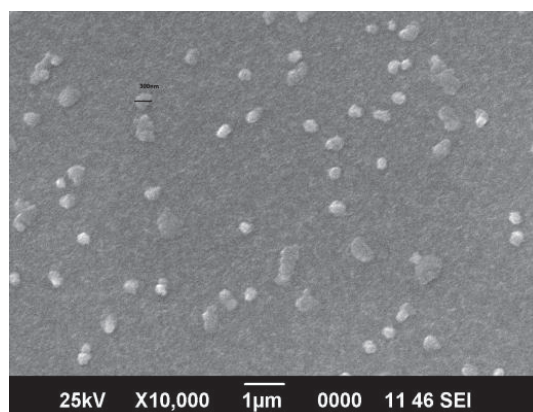


Fig. 7.2 SEM micrograph of silver antimony selenide thin film.

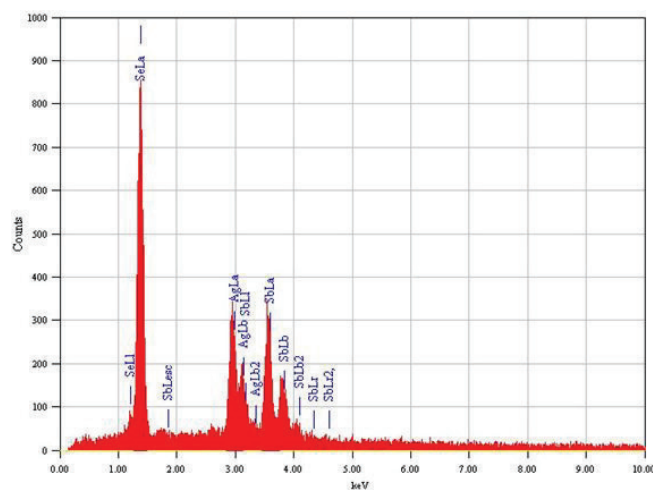


Fig. 7.3 EDAX spectra of a typical silver antimony selenide thin film

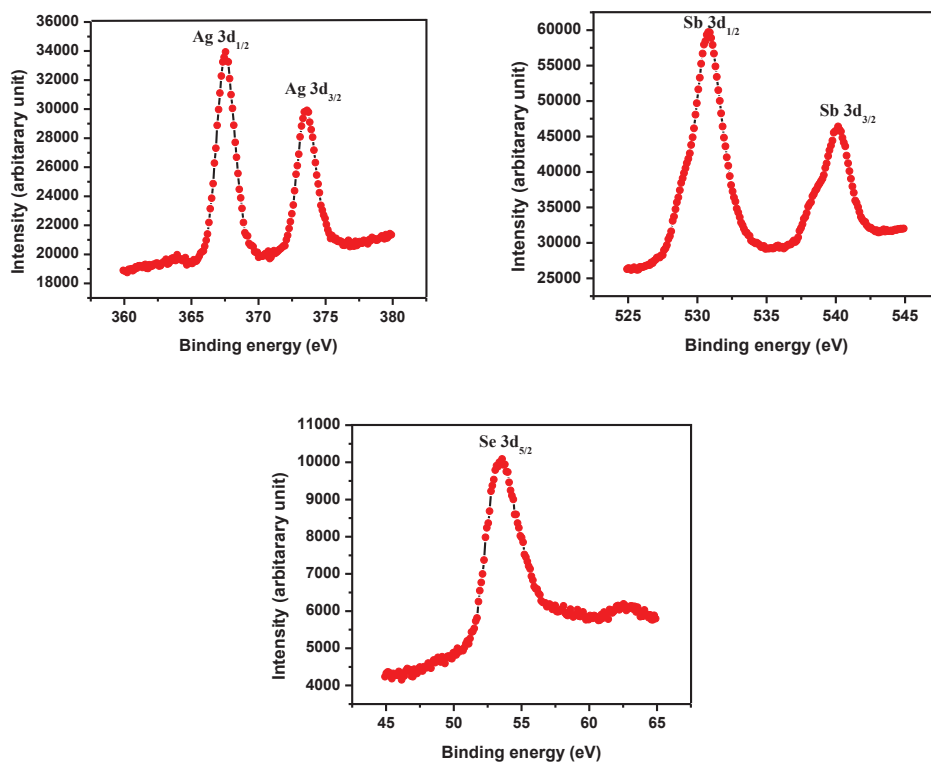


Fig. 7.4 Plots of (a) silver 3d spectra and 4(b) antimony 3d spectra and 4(c) selenium 3d spectra of AgSbSe_2 thin films.

The observed binding energy position of major peaks of silver corresponds to 367.53 eV for $\text{Ag } 3d_{1/2}$, 373.58 eV for $\text{Ag } 3d_{3/2}$ (figure 7.4(a)). The binding energies of $\text{Sb } 3d_{1/2}$ and $\text{Sb } 3d_{3/2}$ peaks (Figure 7.4(b)) are observed at about 530.86 eV and 540.17 eV respectively. The $\text{Se } 3d_{5/2}$ peak shown in Figure 7.4(c) is centered at about 53.59 eV. The observed shift in binding energy positions from the elemental peaks indicates chemical bonding in the compound. Compositional analysis gives result as 19% Ag, 35% Sb and

46% Se are present in the sample, revealing a nearly stoichiometric composition.

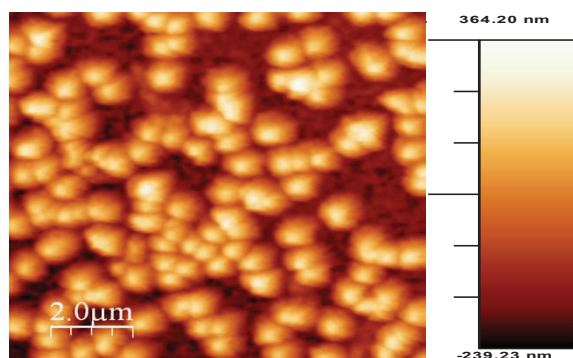


Fig. 7.5(a). The two dimensional AFM images of AgSbSe₂ thin film of the surface (10 X 10 μm).

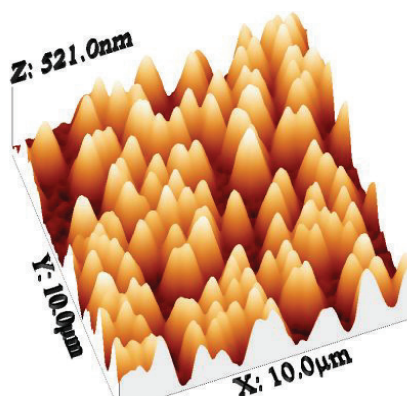


Fig. 7.5(b). The three dimensional AFM images (10 X 10 μm).

Figure 7.5(a) and 7.5(b) show the two and three dimensional view of Atomic Force Microscopic images of AgSbSe₂ thin film, measured over an area of 10 X 10 μm. The grain boundaries are clear in the micrograph. The two micrographs show that the surface of the silver antimony selenide thin film consists of well-defined grains of different sizes and shapes. The appearance of

holes near the boundaries of large grains in the two dimensional view indicate the tendency of the film to agglomerate. During deposition holes had been generated in the film and they continue to grow through the grain boundaries leading to agglomeration. The average grain size obtained from AFM is about 350 nm which is substantiated with the value obtained from SEM. The surface roughness of the as-deposited film is also investigated and it is 121 nm.

7.3.3 Electrical analysis

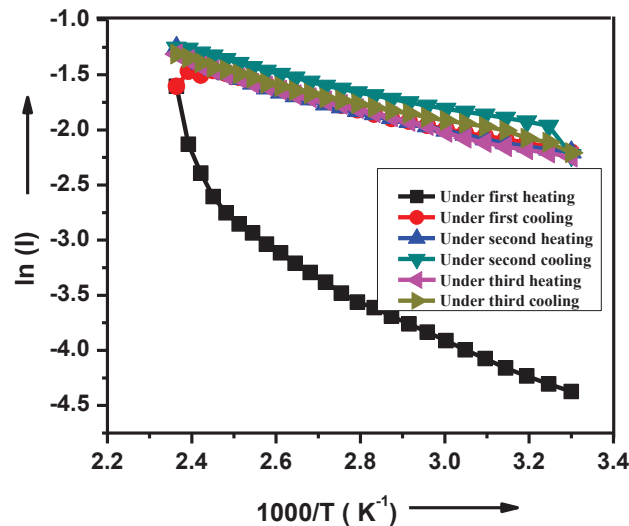


Fig. 7.6 Plot of $\ln(I)$ versus inverse of temperature

The Arrhenius plot of AgSbSe_2 thin film for the three continuous heating and cooling cycles are shown in figure 7.6. During heating a variation of $\ln(I)$ versus $1000/T$ is observed and the cooling curve lies above the heating curve. The samples show a semiconducting nature with rise in temperature. From the figure it is clear that after the first heating cycle, the conductivity

variation with temperature retraces the same path of the first cooling curve indicating that the prepared film is stabilized by releasing the strains in the sample and the electrical properties remain the same. The activation energy calculated is 0.08 eV which is closely matching with the measurements done by Patel et al [19] for the AgSbSe₂ thin films prepared by single source thermal evaporation method in vacuum.

7.3.4 Optical analysis

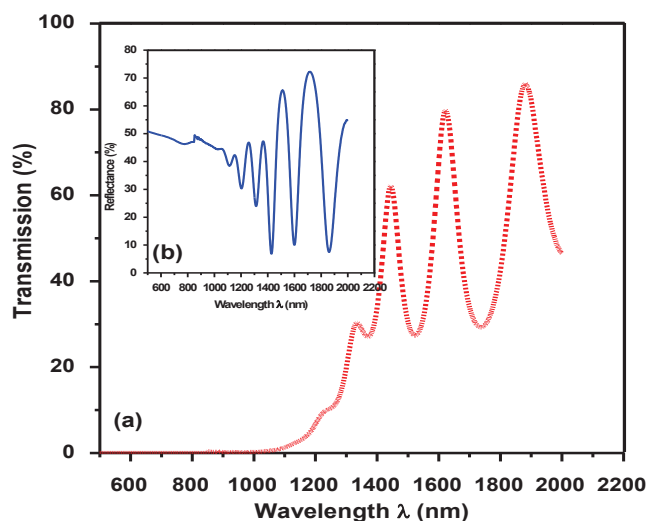


Figure 7.7(a) Typical transmission spectra and (b) reflection spectra

The obtained spectral distribution curves for transmission in the wavelength range of 500-2200 nm are illustrated in Fig. 7.7(a) and 7.7(b). The spectrum shows interference pattern with a sharp fall of transmittance at the band edge. Due to these interference patterns, Swanepoel method [20] is used

to obtain the spectral distribution of the refractive index n and the absorption coefficient α .

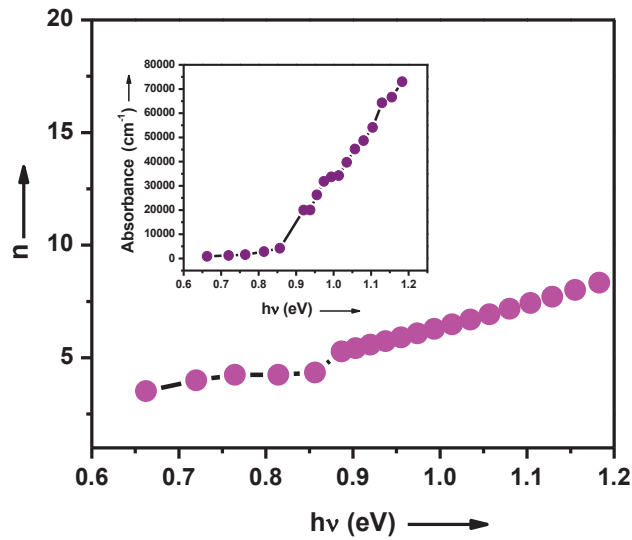


Fig. 7.8 Plots of (a) refractive index and (b) absorbance as a function of $h\nu$ in a typical sample

The refractive index is calculated in weak and medium absorption region and is extrapolated to the strong absorption region by the Cauchy equation. The obtained values of n are used for calculating α . The spectral distributions of n and α versus photon energy $h\nu$ for the AgSbSe_2 thin film are shown in figures 7.8(a) and 7.8(b), respectively. The extinction coefficient (k) is a measure of the fraction of light lost due to scattering and absorption per unit distance of the penetration medium. It can be estimated from the values of α and λ and figure 7.9 illustrates the dependence of extinction coefficient on the photon energy for a typical AgSbSe_2 sample.

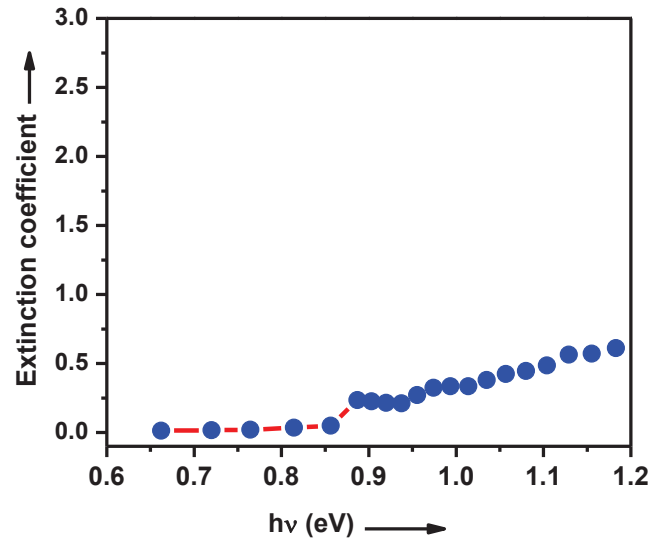


Fig. 7.9 Variation in k with photon energy

For indirect transition, the optical absorption edge can be analyzed by the following relation [21]:

$$(\alpha h\nu) = A(h\nu - E_g \pm E_p)^m \quad (7.1)$$

where A is a constant depends on the transition probability and m is an index that characterizes the optical absorption process. The value of m is 2 and 3 for indirect allowed and indirect forbidden transitions respectively. E_p corresponds to phonon energy. The plot of $(\alpha h\nu)^{1/2}$ versus photon energy $h\nu$ is shown in figure 7. 10. Figure shows that $(\alpha h\nu)^{1/2}$ versus $h\nu$ is a linear function; this linearity indicates the existence of the allowed indirect transitions. The estimated value of E_g for indirect optical transition of AgSbSe₂ films is 0.84 eV. The result is in good agreement with band gap of 0.93 eV reported for

AgSbSe₂ sample annealed at 398 K [9], and 0.90 eV reported by Bindu et. al. [12]. The high value of absorption coefficient ($>10^4 \text{ cm}^{-1}$) and the optical band gap of 0.84 eV make this material suitable for photosensitive devices.

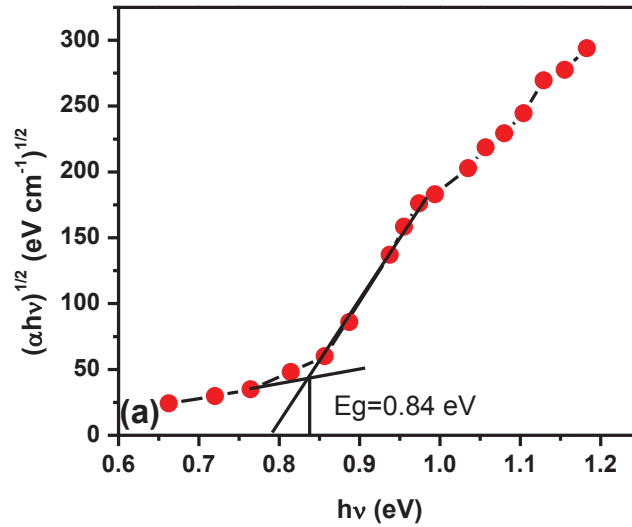


Fig. 7.10 Plot of dependence of $(\alpha h\nu)^{1/2}$ on photon energy for a typical AgSbSe₂ sample

The data of the dispersive refractive index, $n(\lambda)$, can be fitted to the Wemple and DiDomenico (WDD) dispersion relationship, that is single-oscillator model. The single oscillator constants: E_0 , the so called oscillator energy is an average of the optical band gap, E_d is the dispersive energy, which measures the average strength of interband optical transition. By plotting refractive index factor $(n^2 - 1)^{-1}$ versus $(h\nu)^2$ and fitting the data to a straight line yields the oscillator parameters. Figure 7.11 shows the plot of $(n^2 - 1)^{-1}$ versus $(h\nu)^2$.

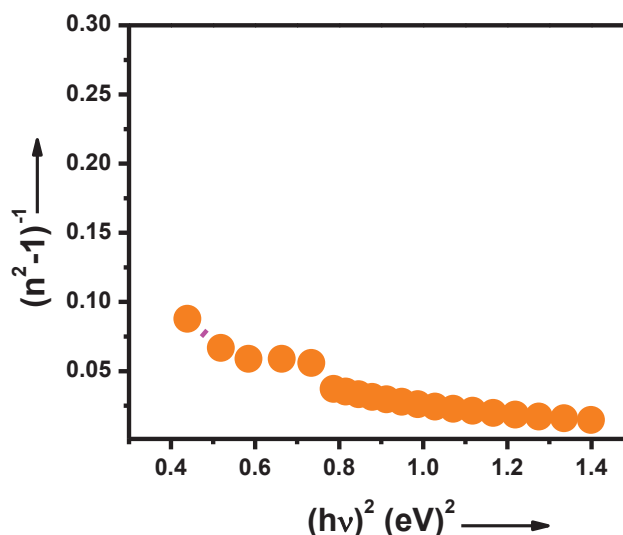


Fig. 7.11 Refractive index factor versus $(h\nu)^2$.

The values of E_0 and E_d can be then calculated from the intercept E_0/E_d , and the slope $1/E_0E_d$. The values of WDD dispersion parameters, E_0 and E_d for the thin film sample are 1.364 eV and 21.52 eV respectively. The optical band gap E_g calculated from Wemple–Didomenico dispersion parameter E_0 , using relation $E_g \approx \frac{E_0}{2}$ is 0.682 eV is almost in agreement with those obtained by the Tauc's extrapolation. The real part of the dielectric constant (ϵ_r) shows how much it will slow down the speed of light in the material, whereas the imaginary part (ϵ_i) shows how a dielectric material absorbs energy from an electric field due to dipole motion. It can be seen clearly from the figure 7.12 that both the real and imaginary parts of the dielectric constant increase with increase in photon energy.

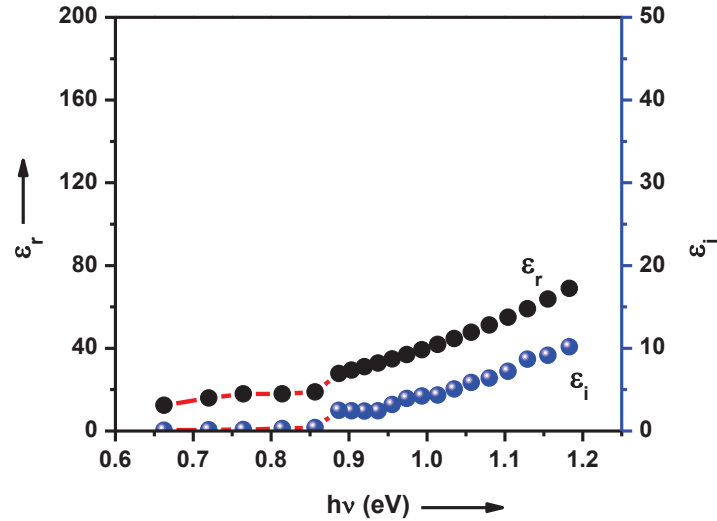


Fig. 7.12 Variation in ϵ_r and ϵ_i with photon energy

The knowledge of the real and the imaginary parts of the dielectric constant provides information about the loss factor ($\tan \delta$):

$$\tan \delta = \frac{\epsilon_i}{\epsilon_r} \quad (7.2)$$

where ϵ_r is the real part and ϵ_i is the imaginary part of the dielectric constant.

Figure 7.13 shows loss factor and Q factor of the films as a function of photon energy. These results indicate that in AgSbSe₂ thin film the loss factor increases with increase in photon energy.

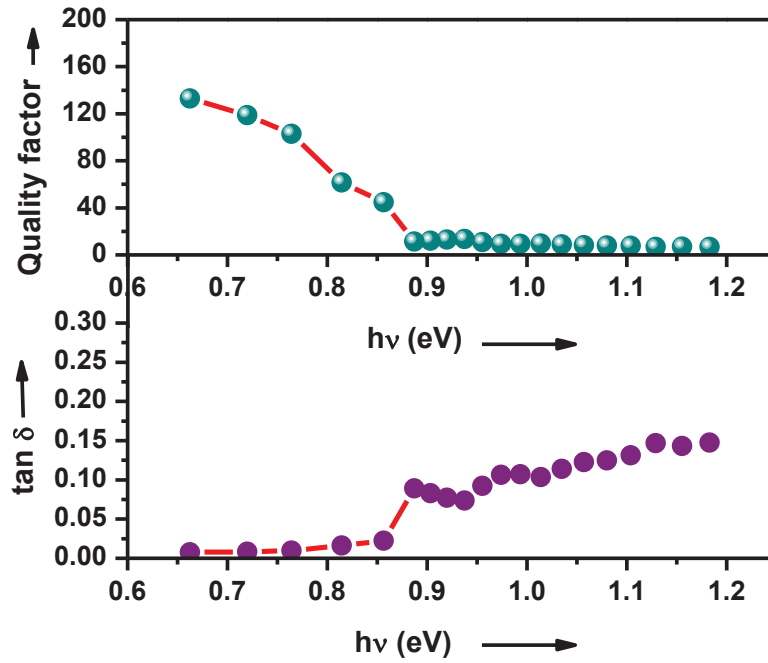


Fig. 7.13 Variation in $\tan \delta$ and Q factor with photon energy

The optical response of a material is mainly studied in terms of the optical conductivity (σ_{opt}) which is shown in figure 7.14. It can be seen clearly from the figure that the optical conductivity increases with increase in photon energy. The sudden increase in optical conductivity can be attributed to the increase in absorption coefficient.

In the low photon energy range it is assumed that the spectral dependence of the absorption edge follows the Urbach rule. A plot of $\ln(\alpha)$ against the photon energy is shown in figure 7.15 and a linear fit is established in the linear portions of the curve. The width of Urbach tail obtained from the fit is 0.123 eV, indicates the smaller density of localized states in the band gap.

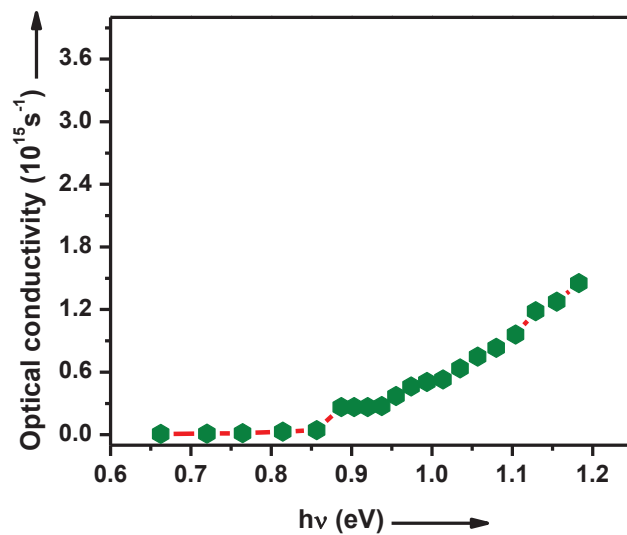
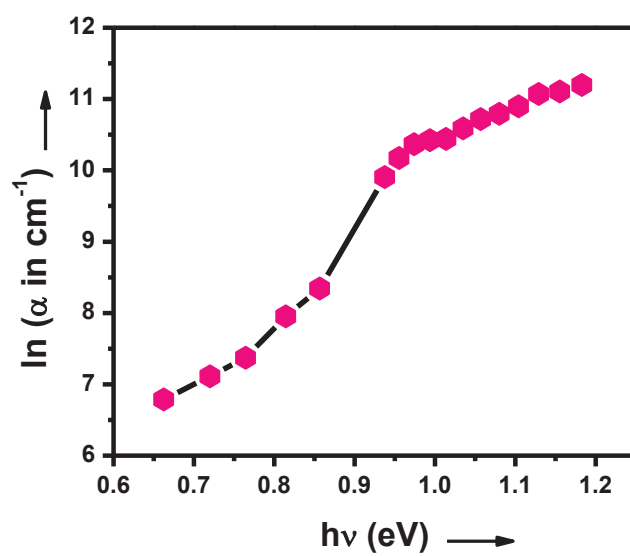


Fig. 7.14 The optical conductivity against photon energy

Fig. 7.15 Plot of ln(α) against the photon energy for AgSbSe₂ sample

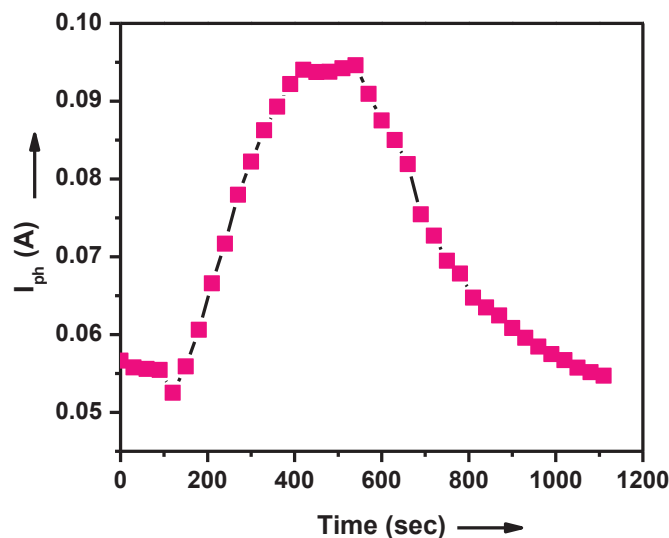


Fig. 7.16 The rise and decay of photocurrent in AgSbSe_2 film at room temperature

Figure 7.16 illustrates the photo current and the dark current in a typical AgSbSe_2 sample. It is clear from this figure that the rise and decay of the photocurrent is very slow in this material. After turning the light off, the photocurrent starts decreasing and a residual photoconductivity exists. The slope of $\ln(I_{ph})$ versus $\ln(t)$ curve (figure 7.17) can be used to calculate the trap depth in the sample and it is found to be 0.039 eV. The differential life time versus time is plotted and is shown in Figure 7.18. It is found that the decay time is increasing with increasing time. These results show the presence of the continuous distribution of localized states in this material.

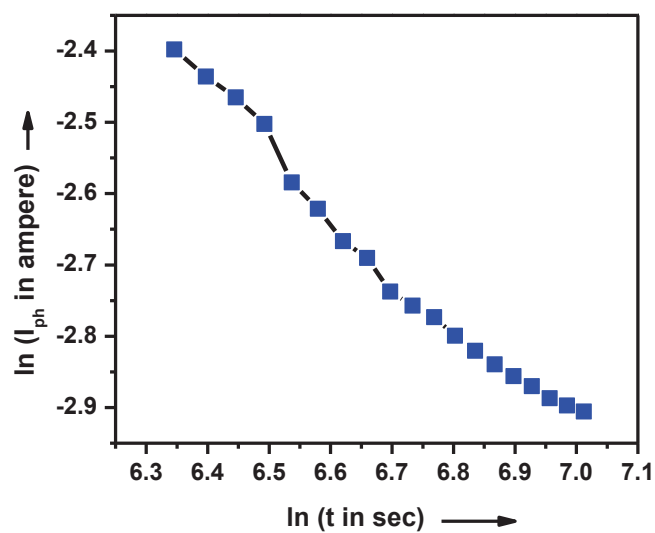
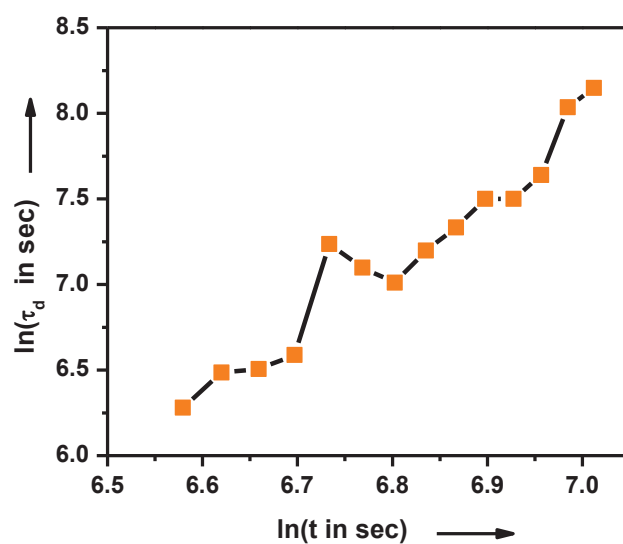
Fig. 7.17 The plot of $\ln(I_{ph})$ versus $\ln(t)$ 

Fig. 7.18 The variation of differential life time with decay time

7.3.5 Low temperature TEP properties and Hall measurement

Among the different new TE materials, tellurium free I-V-VI₂ chalcogenides are one of the promising class of materials due to their intrinsic low lattice thermal conductivity. The strong anharmonicity of chemical bonds of I-V-VI₂ semiconductors may originate from the presence of lone-pair electrons in the sp-hybridized bonding orbitals [22][16]. The valence electron configuration of Sb is 5s²5p³. And the 5s electrons are significantly lower in energy than the 5p orbitals. Therefore the Sb atoms becomes trivalent and forms polar covalent bonds with Se by sharing its p electrons while the s² electron pair forms an isolated bond. The non-bonded electron pair of Sb gives rise to electron clouds surrounding the Sb atoms that is being easily deformed by lattice vibrations, resulting in strong unharmonicity. Recently theoretical studies show that the Gruneisen parameters (γ) are indeed higher in the case of AgSbSe₂ ($\gamma = 3.4$) compared to those of AgSbTe₂ ($\gamma = 2.3$) and AgBiSe₂ ($\gamma = 2.5$) which leads to intrinsically low thermal conductivity in this compound [16][23]. The thermoelectric power S is generally the sum of the electronic term S_e , resulting from the spontaneous tendency of the charge carriers to diffuse from hot to cold, and the phonon term S_g , resulting from the drag on the charge carriers exerted by the phonons streaming from hot to cold by thermal conduction. The phonon drag contribution to thermoelectric power is an effect in which the strong phonon-electron interaction by which the phonons may impart some of their momentum to the diffusing carriers along the temperature gradient, causes an increase in the buildup of charge above that from the diffusion of the electrons alone [24].

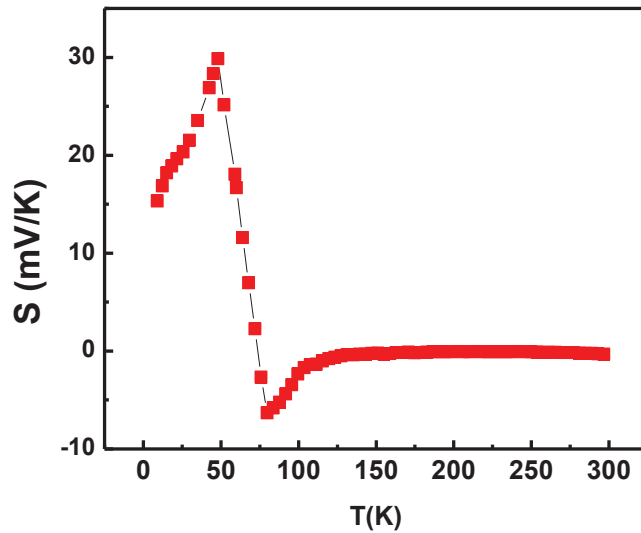


Fig. 7.19. The temperature variation of Seebeck coefficient for the AgSbSe_2 sample.

The phonon drag effect is widely observed in thermoelectric power of metals and semiconductors as peaks and faster enhancement or decrement in TEP than that for pure diffusion alone. The temperature dependence of TEP of the AgSbSe_2 samples is shown in figure 7.19. From around 9 K to 48 K TEP rapidly increases with temperature from 15 mVK^{-1} , to a large positive value of about 30 mVK^{-1} , the conduction should occur predominantly due to holes. This is the largest value of thermoelectric power ever reported for this material at 48 K. At low temperature, even though the electron relaxation time is controlled by impurities, from the linear variation of TEP with increase in temperature suggests the dominance of phonon drag effect that illustrate the strong

interaction between electron-hole system. The S_g tends to zero at both low and high temperatures and gives a maximum value at an intermediate temperature of 48 K where the electron-phonon interaction becomes dominant with respect to the other phonon interactions.

The high positive value of the Seebeck coefficient of about 30 mVK^{-1} at temperature of 48 K shows the hole conductivity of the sample. As temperature increases above 48 K thermoelectric power sharply drops and then an inversion of sign is observed indicating the change of the predominant carriers from holes to electrons. The TEP changes its sign since electrons and holes plus strong electron-phonon interaction contributes to the superlattice formation during the structural phase transition of NaCl type structures [25]. The figure shows that the phonon drag peaks of both holes and electrons occurs due to strong phonon electron interaction, is the typical feature of this sample. In AgSbSe₂ thin films the rock salt structure was reported and one can expect an inversion on carrier type during phase transformation, the zero crossing of TEP is clear in the figure. Sergey et al [25] reported the phase transitions in ZnTe under pressure as other chalcogenides by thermoelectric power method, which is sensitive to changes of sign of dominant charge carriers usually occurring under phase transformations. Amir A. Lakhani and Jandl [26] reported under superlattice formation, the low temperature TEP converts its sign, indicating that dominant carrier type passes from p to n. From the above figure, the TEP dip observed at a temperature of about 80 K confirms the large role of phonon drag effect than the drift-diffusion contribution. A pronounced negative minimum observed in the transforming samples exhibits the super lattice state

and the TEP dip is due to the strong phonon drag effect which leads to the softening of the associated zone-boundary phonon. The change of sign of Seebeck coefficient of AgSbSe₂ sample in the solid to liquid transition at high temperature was reported by A. Abdelghany et al [11]. The TEP dip temperature T_m allows us to calculate the non-normalised energy of the phonon using the relation [27]:

$$k_B T_m = h \omega_m \quad (7.3)$$

where k_B is the Boltzman's constant, h is the Plank's constant and evaluated phonon frequency is to be 56 cm⁻¹ at the TEP dip temperature of 80 K.

Table 7.4 Hall effect measurement results

Carrier concentration n (cm ⁻³)	Mobility μ (cm ² V ⁻¹ s ⁻¹)	Hall coefficient R_H (cm ³ C ⁻¹ V ⁻¹)	Magnetoresistance Ω (Ω)	Conductivity σ (Ω^{-1} cm ⁻¹)
$\sim 2.15 \times 10^{18}$	$\sim 4.174 \times 10^2$	~ 2.95	~ 27.19	$\sim 1.44 \times 10^2$

Table 7.5 Carrier properties at room temperature

Fermi level E_F (eV)	Effective mass m^*	Density of states N (cm ⁻³)	Relaxation time τ (s)	Fermi velocity v_F (m s ⁻¹)	Mean free path l (nm)
~ 0.024	$\sim 0.26 m_0$	$\sim 9.26 \times 10^{16}$	$\sim 6.17 \times 10^{-15}$	0.027×10^6	1.7

The magnitude of the Seebeck coefficient is found to be 311 μ VK⁻¹ at room temperature. Also, a nearly linear temperature dependence of Seebeck coefficient indicates typical degenerate behavior. The room temperature power

factor of the film have been found to be $6.97 \times 10^{-6} \text{ Wcm}^{-1}\text{K}^{-2}$ with a carrier concentration of $2.15 \times 10^{18} \text{ cm}^{-3}$ which is slightly above those previously reported for AgSbSe_2 semiconductors [16][28]. The Seebeck coefficient near room temperature is found to be almost comparable to that measured in p-type AgSbSe_2 ($300 \mu\text{VK}^{-1}$). The increased power factor in AgSbSe_2 thin film when compared to p-type pristine AgSbSe_2 and Sb deficient $\text{AgSb}_{0.9925}\text{Se}_2$ ($2.5 \times 10^{-6} \text{ Wcm}^{-1}\text{K}^{-2}$ at $\sim 608 \text{ K}$ and $4.7 \times 10^{-6} \text{ Wcm}^{-1}\text{K}^{-2}$ at room temperature respectively) could be justified by considering the increased conductivity in the thin film sample ($\sigma = 144 \Omega^{-1}\text{cm}^{-1}$) with that of the latter ($\sigma = 86 \Omega^{-1}\text{cm}^{-1}$). The Seebeck coefficient and Hall carrier-concentration data were used to estimate the Fermi level and effective mass of carriers (table 7.4 and 7.5). Under degenerate approximation, the Fermi level determined as 0.024 eV, the narrow Fermi level position below the conduction band edge leads to high Seebeck coefficient at room temperature. The value of density of states effective mass estimated as $0.26 m_0$ is lesser than that reported for AgSbSe_2 compound [23]. A m^* value of $1.2 m_0$ in the case AgSbSe_2 with a carrier density of $15 \times 10^{18} \text{ cm}^{-3}$ and mobility of $7 \text{ cm}^2\text{V}^{-1}\text{s}^{-1}$ has also been reported by Guin et al. The comparatively high electron mobility ($417.4 \text{ cm}^2\text{V}^{-1}\text{s}^{-1}$) due to the reduction in effective mass, resulting in increased conductivity in this film. The combination of high electrical conductivity and reasonable Seebeck coefficient leads to near optimum power factor value in the room temperature. This material exhibits an interesting temperature dependence of TEP, which makes the material particularly attractive for device applications at low

temperatures because the same base materials can be used for the p and n legs of the thermoelectric converter.

7.4 Conclusion

Silver antimony selenide thin films are deposited on glass substrates using reactive evaporation technique. The present work reports its structural, optical and low temperature thermoelectric properties. The structural parameters such as particle size, lattice constant, number of crystallites per unit area and strain are estimated. The films obtained are semiconducting in nature and has activation energy of 0.08 eV. The absorbance of the film is found to be high ($> 10^4 \text{ cm}^{-1}$) and the optical band gap is 0.84 eV which is indirect allowed. The analysis of temperature variations of TEP in terms of phonon-drag effect gives that in the case of AgSbSe_2 thin film there exists a strong electron-phonon interaction which is a basic feature of the structurally transforming samples. The TEP dip at 80 K as due to phonon drag effect in the transforming samples gives the non-normalised phonon frequency as 56 cm^{-1} . The density of state effective mass, Fermi level position and mobility of charge carriers have been estimated. Notably the near optimum power factor with an optimized carrier concentration has been achieved in room temperature and the considerable increases in Seebeck coefficient at lower temperatures suggesting that AgSbSe_2 thin films are promising for TE applications.

References

- [1] R. S. Kumar, A. Sekar, N. V. Jaya, and S. Natarajan, "Synthesis and high pressure studies of the semiconductor AgSbSe_2 ," *J. Alloys Compd.*, vol. 285, pp. 48–50, 1999.

- [2] K. Wang, C. Steimer, R. Detemple, D. Wamwangi, and M. Wuttig, "Assessment of Se based phase change alloy as a candidate for non-volatile electronic memory applications," vol. 81, pp. 1601–1605, 2005.
- [3] J. G. Garza, S. Shaji, A. C. Rodriguez, T. K. Das Roy, and B. Krishnan, "AgSbSe₂ and AgSb(S,Se)₂ thin films for photovoltaic applications," *Appl. Surf. Sci.*, vol. 257, pp. 10834–10838, 2011.
- [4] F. Liu, J. Li, J. Yang, Z. Han, L. Jiang, Y. Lai, J. Li, Y. He and Y. Liub, "Preparation and characterization of AgSbSe₂ thin films by electrodeposition," *J. The Electrochemical Society*, vol. 160, no. 11, pp. 578-582, 2013.
- [5] B. A. Hasan and I. M. Ibrahim, "Structural, Morphological and Electrical Properties of AgSbSe₂ Thin Films," *J. Eng. & Tech.*, vol. 33, no. 7, pp.1283–1289, 2015.
- [6] A. R. Patel and D. Lakshminarayana, "Effect of substrate temperature on the crystallinity of AgSbSe₂ films," *Thin Solid Films*, vol. 98, pp. 59–63, 1982.
- [7] H.El-Zahed, "Electrical and structural studies of AgSbSe₂ thin films," *Thin Solid Films*, vol. 238, pp. 104–109, 1994.
- [8] M. Hamam, Y. El-Gendy, M. S. Selim, A. M. Salem, and N. H. Teleb, "Optical Properties of Thermally Evaporated AgSbSe₂ Thin Films," *J. Appl. Sci. Res.*, vol. 5, no. 12, pp. 2323–2331, 2009.
- [9] M. Hamam, M. S. Selim, N. H. Teleb, and A. M. Salem, "Structure and optical properties in the amorphous to crystalline transition in AgSbSe₂ thin films," *Phys. Status Solidi C*, vol. 7, no. 3, pp. 861–864, 2010.
- [10] J. G. Garza, S. Shaji, A. M. Arato, E. Perez-Tijerina, A. C. Rodriguez, T. K. Das Roy and B. Krishnan, "Chemically Deposited Silver Antimony Selenide Thin Films for Photovoltaic Applications," *Mater. Res. Soc. Symp. Proc*, vol. 1165, pp. 1–6, 2009.

- [11] A. Abdelghany, S. N. Elsayed, D. M. Abdelwahab, A. H. Abou El Ela and N.H. Mousa, "Electrical conductivity and thermoelectric power of AgSbSe_2 in the solid and liquid states," *Mater. Chem. Phys.*, vol. 44, pp. 277–280, 1996.
- [12] K Bindu, Jose Campos, M. T. S. Nair, A Sanchez and P K Nair, "Semiconducting AgSbSe_2 thin film and its application in a photovoltaic structure," *Semicond. Sci. Technol*, vol. 20, pp. 495–504, 2005.
- [13] K. Bindu, M. T. S. Nair, T. K. Das Roy and P. K. Nair, "Chemically deposited photovoltaic structure using antimony sulfide and silver antimony selenide absorber films service sulfide and silver antimony selenide absorber films," vol. 9, no. 6, pp. G195–196, 2006.
- [14] K. Wojciechowski, J. Tobola, M. Schmidt, and R. Zybala, "Crystal structure, electronic and transport properties of AgSbSe_2 and AgSbTe_2 ," *J. Phys. Chem. Solids*, vol. 69, pp. 2748–2755, 2008.
- [15] M. Schmidt, R. Zybala, K. T. Wojciechowski, "Structural and Thermoelectric Properties of AgSbSe_2 - AgSbTe_2 system," *Mater. Ceram. /Ceramic Mater.*, vol. 62, no. 4, pp. 465–470, 2010.
- [16] X. Zhang and Li-Dong Zhao, "Thermoelectric materials: Energy conversion between heat and electricity," *J. Materiomics*, vol. 1, pp. 92–105, 2015.
- [17] *Powder Diffraction file, International Centre for Diffraction Data (ICDD) Card No: 89-3670.*
- [18] H. S. Soliman, D. Abdel-Hady and E. Ibrahim, "Optical properties of thermally evaporated AgSbSe_2 thin films," *J. Phys.; Condensed Matter*, vol. 10, p. 847, 1998.
- [19] A. R. Patel, D. Lakshminarayana, and K. V. Rao, "Growth and crystallization of AgSbSe_2 films," *Thin Solid Films*, vol. 94, pp. 51–57, 1982.

- [20] M. M. Abdel-Aziz, I. S. Yahia, L. A. Wahab, M. Fadel and M. A. Afifi, "Determination and analysis of dispersive optical constant of TiO_2 and Ti_2O_3 thin films," *Appl. Surf. Science*, vol. 252, pp. 8163-8170, 2006.
- [21] C. Kittel, *Introduction to solid state physics*, 7th ed. John Wiley & sons publishing, 2005.
- [22] M. D. Nielsen, V. Ozolins and J. P. Heremans, "Lone pair electrons minimise lattice thermal conductivity," *Energy Environ. Sci.*, vol. 6, pp. 570–578, 2013.
- [23] S. N. Guin, D. S. Negi, R. Detta and K. Biswas "Nanostructuring, carrier engineering and bond anharmonicity synergistically boost the thermoelectric performance of p-type $\text{AgSbSe}_2\text{-ZnSe}$," *J. Mater. Chem. A*, vol. 2, pp. 4324–4331, 2014.
- [24] A. R. Patel, D. Lakshminarayana, and K. V. Rao, "Theory of the thermoelectric power of semiconductors," *Phys. Rev.*, vol. 96, pp. 1163–1187, 1954.
- [25] V. O. Sergey, V. V. Shchennikov, "Phase transitions investigation in ZnTe by thermoelectric power measurements at high pressure", *Solid State Commun.*, vol. 132: pp. 333-336, 2004.
- [26] A. A. Lakhani, S. Jandl, "Thermoelectric power of $\text{TiSe}_{2-x}\text{S}_x$ mixed crystals at low temperatures". *Phys Rev B*, vol.28, p. 1978, 1983.
- [27] K. P. Mohanachandra, J. Uchil, "Thermoelectric power of CdS and CdSe films deposited on vibrating substrates", *Thin Solid Films*, vol. 305, p. 124, 1996.
- [28] S. N. Guin and K. Biswas, "Thermoelectric performance of p-type AgSbSe_2 ," *J. Mater. Chem. C*, vol. 3, pp. 10415–10421, 2015.

Chapter 8

Summary and future outlook

8.1 Summary and general conclusions

8.2 Future outlook

8.1 Summary and general conclusions

The field of development of both PV and TE materials is now growing steadily due to their ability to convert solar energy or waste heat to electricity, thus providing a solution for energy crisis and however, the TE/PV energy conversion efficiency is mainly limited by the performance of the materials. Among the various emerging materials, chalcogenide compounds have been identified as potential materials for PV applications. The development of high performance TE materials based on selenium, aside from conventional tellurium based materials like PbTe and Bi₂Te₃, will become increasingly attractive for research due to the toxicity and low abundance of tellurium.

In this thesis, attempt has been made to prepare thin films of four selenium based intrinsically low thermal conductivity materials including PbSe, Pb_{3.58}Sb_{4.42}Se₁₀, Ag₂Se, and AgSbSe₂ using reactive evaporation technique. The good quality films are obtained by trial and error. The deposition parameters like impingement rates and substrate temperature are optimized for the preparation of nearly stoichiometric thin films. The films are preliminarily characterized using various techniques such as X-ray Diffraction

(XRD), X-ray photoelectron spectroscopy (XPS), Scanning Electron Microscope (SEM), Atomic Force Microscopy (AFM), optical absorption/transmission, electrical conductivity, Hall measurement, photoconductivity and low temperature thermoelectric power measurements. Several optical parameters of the thin film such as photoconductivity, extinction coefficient and band gap etc are studied. In order to check the potential of thin films in TE applications the room temperature Hall measurements and low temperature TEP measurements are done. From Seebeck coefficient and carrier concentration, the density of state Fermi level, effective mass, mean free path, relaxation time and Fermi velocity are determined.

Among the various IV–VI narrow band gap semiconductor, PbTe has been the most studied for TE applications. In this thesis, polycrystalline thin films of p-type PbSe are prepared using the reactive evaporation technique and the TE measurements indicate that the narrow of Fermi level (0.054 eV) position to the valence band edge leads to optimum Seebeck coefficient. Moreover, the optimum carrier concentration and electrical conductivity gives near optimum power factor of $12 \times 10^{-4} \text{ Wcm}^{-1}\text{K}^{-2}$ suggests the possible application of PbSe thin film in room temperature small scale TE applications.

For the first time, thin films of $\text{Pb}_{3.58}\text{Sb}_{4.42}\text{Se}_{10}$ with p-type conductivity, prepared using reactive evaporation technique under optimized deposition conditions are reported. The film showed direct allowed optical band gap of 1.31 eV, high absorption coefficient ($>10^4 \text{ cm}^{-1}$) and optical

conductivity, suggesting the possible application of $\text{Pb}_{3.58}\text{Sb}_{4.42}\text{Se}_{10}$ thin films as absorber layer in solar cell.

Polycrystalline thin films of n-type Ag_2Se are prepared by reactive evaporation technique to investigate the optoelectronic and thermoelectric properties. The polymorphic phase transition temperature is observed at 398 K in these films and the reverse transition is taken place at 368 K. The n-type film shows high electrical conductivity of $1.3 \times 10^3 \Omega^{-1} \text{cm}^{-1}$ and power factor of $0.52 \times 10^{-4} \text{Wcm}^{-1}\text{K}^{-2}$ at room temperature, is always desirable to have compatible materials for the n-legs of a thermoelectric couple .

Thin film of AgSbSe_2 has been prepared on ultrasonically cleaned glass substrate at a substrate temperature of $398 \pm 5\text{K}$ by reactive evaporation at a pressure of 10^{-5} mbar. The near optimum power factor with an optimized carrier concentration at room temperature and the large Seebeck coefficient at low temperature due to phonon drag effect, suggesting that AgSbSe_2 thin films are promising for TE applications.

8.2 Future outlook

The electrical and transport properties of chalcogenide compounds reported here suggests the possibility of investigating various unexplored properties and the potential in using them for various application like photovoltaic cell and thermoelectric module. The intrinsically low thermal conductivity together with rapid increase of S in p- type PbSe samples leads to promising thermoelectric performance in these thin films, suggests it as an inexpensive alternative to PbTe material.

Lead antimony selenide showed good electrical and optical properties and this can be prepared either as n-type and p-type depending on Pb/Sb ratio. The possibility of fabricating homojunction/heterojunction solar cell using $\text{Pb}_{3.58}\text{Sb}_{4.42}\text{Se}_{10}$ can be investigated. The low σ ($7.786 \times 10^{-5} \Omega^{-1}\text{cm}^{-1}$) and high S ($1691 \mu\text{VK}^{-1}$) at room temperature give a moderate power factor of $2.23 \times 10^{-8} \text{Wcm}^{-1}\text{K}^{-2}$. The low conductivity must be due to low carrier concentration, further improvement is possible through carrier concentration optimisation.

Apart from possessing intrinsically low thermal conductivity, AgSbSe_2 has a favourable band structure. Therefore doping will significantly modify the density of state near the Fermi level of AgSbSe_2 results further improvement in power factor. The thermal conductivity and figure of merit of the as prepared films can be evaluated.